Evgeni Zhelyazkov

# An investigation into the fatigue behavior of micro-cracks in resin rich regions of composite laminates produced by liquid infusion


# An investigation into the fatigue behavior of micro-cracks in resin rich regions of composite laminates produced by liquid infusion

By

Evgeni Zhelyazkov

in partial fulfilment of the requirements for the degree of

**Master of Science**

in Aerospace Engineering

at the Delft University of Technology,

to be defended publicly on Friday November 4, 2016 at 01:00 PM.

Supervisors: Dr. Calvin Rans, TU Delft

Dr. Rik-Jan Lemmen, Airbus Operations GmbH

Thesis committee: Dr. Rene Alderliesten , TU Delft

Dr. Wim Verhagen, TU Delft

*This thesis is confidential and cannot be made public until November 4, 2016.*

## Contents

## Acknowledgements

The development of this Master thesis would not be possible without the contribution of many people. I express my sincerest gratitude to everybody who made it possible. I am thankful to my TU Delft supervisor Dr. Calvin Rans and my Airbus supervisor Dr. Rik-Jan Lemmen for the continuous and very helpful support during the course of the whole research project.

Many thanks to all technicians from Delft Aerospace Structures and Materials Laboratory (DASML), who helped me perform the manufacturing and the testing stages of the project – Berthil Grashof, Fred Bosch, Bart Wiegant, Gertjan Mulder, Johan Boender, Cees Paalvast, Frans Oostrum and Lijing Xue. Many thanks to all technicians from Dienst Elektronische en Mechanische Ontwikkeling (DEMO) workshop in the DASML headed by Ed Roessen for all the machining operations facilitating the manufacturing of the specimens for this project.

Thanks a lot to Simeon Dishkov, who spent many long evenings and weekends with me, helping with the specimen manufacturing. Last, but not least thanks to my parents and my girlfriend, who supported me in every possible way.

Evgeni Zhelyazkov

Delft, November 2016

## Executive summary

Damage is found in resin rich bead corner radii of RTM 6 epoxy-based composite ribs due to in-service thermal-mechanical loading after an aircraft inspection. The same types of damage are obtained through pure thermal cycling of a single bead. However, thermal cycling is a time-consuming process. Therefore, a faster way of damage investigation is required. A potential way to achieve this objective is by mechanically cycling a coupon specimen with simpler geometry than the bead.

To investigate potential solutions to the problem a literature review is performed. The scope of the literature review covers several topics as follows. Laminate fatigue damage modes and their impact on the laminate is researched. It is discovered that it is typical for RTM 6 epoxy-based laminates to build-up high matrix residual tensile stresses after manufacturing. Several differences between thermal and mechanical cycling are discovered. It is found that the most common way to test composites is by the use of ASTM standards. However, there is little available information about the fatigue behavior of laminates with resin rich areas.

Investigation of the fatigue behavior of laminates with resin rich areas is performed by the use of FEA and physical tests. Four specimen types labeled from A to D are manufactured. Type A is a dog-bone pure RTM 6 specimen. Types B to D are all composite specimens with the same in-plane geometry and different layups and manufacturing processes. All specimens are tested statically and in fatigue. In the fatigue testing session, fractography of the damage occurring at different test conditions for different specimen types is performed. In addition, two FE models are created. The first model is of the bead. The second model is a harmonized model applicable to all composite specimen types with required layup readjustments for each specimen type.

It is discovered by FEA that the maximum principal stress in the resin rich area is perpendicular to the matrix cracks in the bead and the composite specimens. It is also discovered that the maximum principal stress cycle of the matrix at the resin rich layer interface with the fabric is similar in the bead and the specimens. The similar fatigue parameters are the R-ratio and the stress amplitude. The parameter similarity suggests they could potentially drive the resin rich layer fatigue damage initiation. Moreover, a positive through-the-thickness stress gradient is discovered, which suggests the cracks are likely to initiate bellow the resin rich layer surface. This hypothesis is further supported by fractographic observations of cracks not reaching the laminate free surface.

Static and fatigue tests are performed. The static test provides the UTS of all specimen types, based on which cyclic load levels are selected. In the specimen fatigue tests several results are observed. In the first place, damage similar to the bead damage is found, namely cracks and delamination. In the second place, the damage is observed to penetrate through the laminate thickness and to be dependent upon the laminate compaction. However, this penetration depth dependency on the compaction might be influenced by the second curing cycle of specimen type C, in which the damage was observed. Finally, reduction in the specimen stiffness is observed due to fatigue damage accumulation in time.

Based on the results recommendations are formulated. For design purposes resin rich area formation should be avoided both inside and outside the laminate. If their formation is inevitable, at least the laminate should be kept well compacted and the resin rich area location should be kept only at the surface. For future research, two topics are identified as requiring such. First, is the laminate stiffness reduction. Second, is the influence of the second curing cycle of the well compacted specimen type C.

# Nomenclature

### List of abbreviations

| | |
|---|---|
| ASTM | American Society for Testing and Materials |
| CLPT | Classical Lamination Plate Theory |
| CTE | Coefficient of Thermal Expansion |
| DASML | Delft Aerospace Structures and Materials Laboratory |
| DEMO | Dienst Elektronische en Mechanische Ontwikkeling *(in Dutch)* |
| DMTA | Dynamic Mechanical Thermal Analysis |
| FE | Finite Element |
| FEA | Finite Element Analysis |
| MCID | Matrix Crack Induced Delamination |
| MCIM | Matrix Crack Induced Micro-cracking |
| RT | Room Temperature |
| RTM | Resin Transfer Molding |
| TMA | Thermal Mechanical Analysis |
| UD | Uni-Directional |
| UTS | Ultimate Tensile Strength |
| VI | Vacuum Infusion |
| VTP | Vertical Tail Plane |

## List of symbols

| | | |
|---|---|---|
| $T$ | Temperature | [°C] |
| $T_g$ | Glass transition temperature | [°C] |
| $T_{cure}$ / $T_c$ | Curing temperature | [°C] |
| $T_{infusion}$ | Infusion temperature | [°C] |
| $T_{zero\text{-}stress}$ | Zero-stress temperature | [°C] |
| $T_{min}$ | Minimum temperature of a thermal fatigue cycle | [°C] |
| $T_{max}$ | Maximum temperature of a thermal fatigue cycle | [°C] |
| $dT_{min}$ | Thermal load at minimum temperature of a thermal fatigue cycle | [°C] |
| $dT_{max}$ | Thermal load at maximum temperature of a thermal fatigue cycle | [°C] |
| RT / $T_0$ | Room temperature | [°C] |
| $p_{absolute}$ | Absolute pressure | [mbar] |
| $p_{cure}$ | Curing absolute pressure | [mbar] |
| $p_{infusion}$ | Infusion absolute pressure | [mbar] |
| UTS | Ultimate tensile strength | [MPa] / [N/mm] |
| $UTS^{26°C}$ | Ultimate tensile strength at 26°C | [MPa] / [N/mm] |
| $UTS^{(-20)°C}$ | Ultimate tensile strength at (-20)°C | [MPa] / [N/mm] |
| S11 | Longitudinal normal in-plane stress | [MPa] |
| $S11_{matrix}$ | Longitudinal normal in-plane stress of the matrix | [MPa] |
| $S11_{fiber}$ | Longitudinal normal in-plane stress of the fibers | [MPa] |
| $S11_a$ | Longitudinal normal in-plane stress amplitude | [MPa] |
| $S11_{min}$ | Minimum longitudinal normal in-plane stress of a fatigue cycle | [MPa] |
| $S11_{max}$ | Maximum longitudinal normal in-plane stress of a fatigue cycle | [MPa] |
| $S11_{min\ load}$ | Longitudinal normal in-plane stress at minimum applied load of a fatigue cycle | [MPa] |
| $S11_{max\ load}$ | Longitudinal normal in-plane stress at maximum applied load of a fatigue cycle | [MPa] |
| S22 | Lateral normal in-plane stress | [MPa] |
| S12 | Shear in-plane stress | [MPa] |
| SP | Maximum in-plane principal stress | [MPa] |
| SIL | Interlaminar stress | [MPa] |
| $SIL_a$ | Interlaminar stress amplitude | [MPa] |
| $SIL_{min}$ | Minimum interlaminar stress of a fatigue cycle | [MPa] |
| $SIL_{max}$ | Maximum interlaminar stress of a fatigue cycle | [MPa] |
| CTE | Coefficient of thermal expansion | [1/°C] |
| N | Laminate edge running load | [N/mm] |
| N11 | Longitudinal normal laminate edge running load | [N/mm] |
| $N11_{fiber}$ | Longitudinal fiber load | [N/mm] |
| $N11_{fiber}^{26°C}$ | Longitudinal fiber residual load at 26°C | [N/mm] |

| | | |
|---|---|---|
| $N11_{fiber}^{(-20)°C}$ | Longitudinal fiber residual load at (-20)°C | [N/mm] |
| $dN11_{fiber}$ | Difference in the longitudinal fiber residual load between 26°C and (-20)°C | [N/mm] |
| $N11_{min}$ | Minimum applied normal laminate edge running load of a fatigue cycle | [N/mm] |
| $N11_{max}$ | Maximum applied normal laminate edge running load of a fatigue cycle | [N/mm] |
| N22 | Lateral normal laminate edge running load | [N/mm] |
| N12 | Shear laminate edge running load | [N/mm] |
| F1 | Applied longitudinal mechanical force | [N] |
| $F1_{min}$ | Minimum applied longitudinal mechanical force of a fatigue cycle | [N] |
| $F1_{max}$ | Maximum applied longitudinal mechanical force of a fatigue cycle / static test | [N] |
| R | R-ratio of a fatigue cycle | [-] |
| $w_{specimen}$ | Minimum specimen width | [mm] |
| $t_{specimen}$ | Minimum specimen thickness | [mm] |
| $t_{fiber}$ | Fabric thickness | [mm] |

# List of tables

## List of figures

# 1. Introduction

This research project experimentally investigates in-service damage located at resin rich areas in the ribs of an aircraft Vertical Tail Plane (VTP). Ribs are key structural components in the construction of the main support structure of wings and empennages. In the aircraft VTP (Figure 1) this structure is known as the VTP box (Figure 2). The ribs have three functions in the VTP box: to support the skin in maintaining the required aerodynamic shape, to improve the buckling stability of the skin and to increase the torsional stiffness of the VTP box. The rib structures are loaded mechanically in shear and thermally by the ambient temperature. The relatively small thickness of the ribs makes them sensitive to buckling (e.g. Rib 9 in the VTP box of the A330 is 1.44 mm thick, [1]). Nevertheless, small thicknesses are required to accommodate the stringent weight efficiency demand of the aerospace industry.

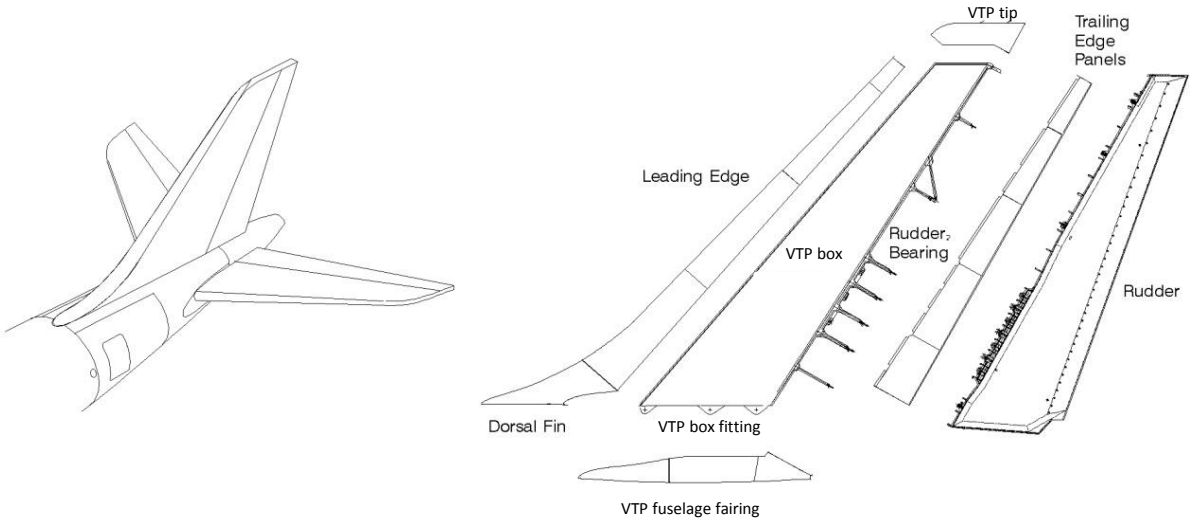


**Figure 1, Exploded view of the VTP, [2]**

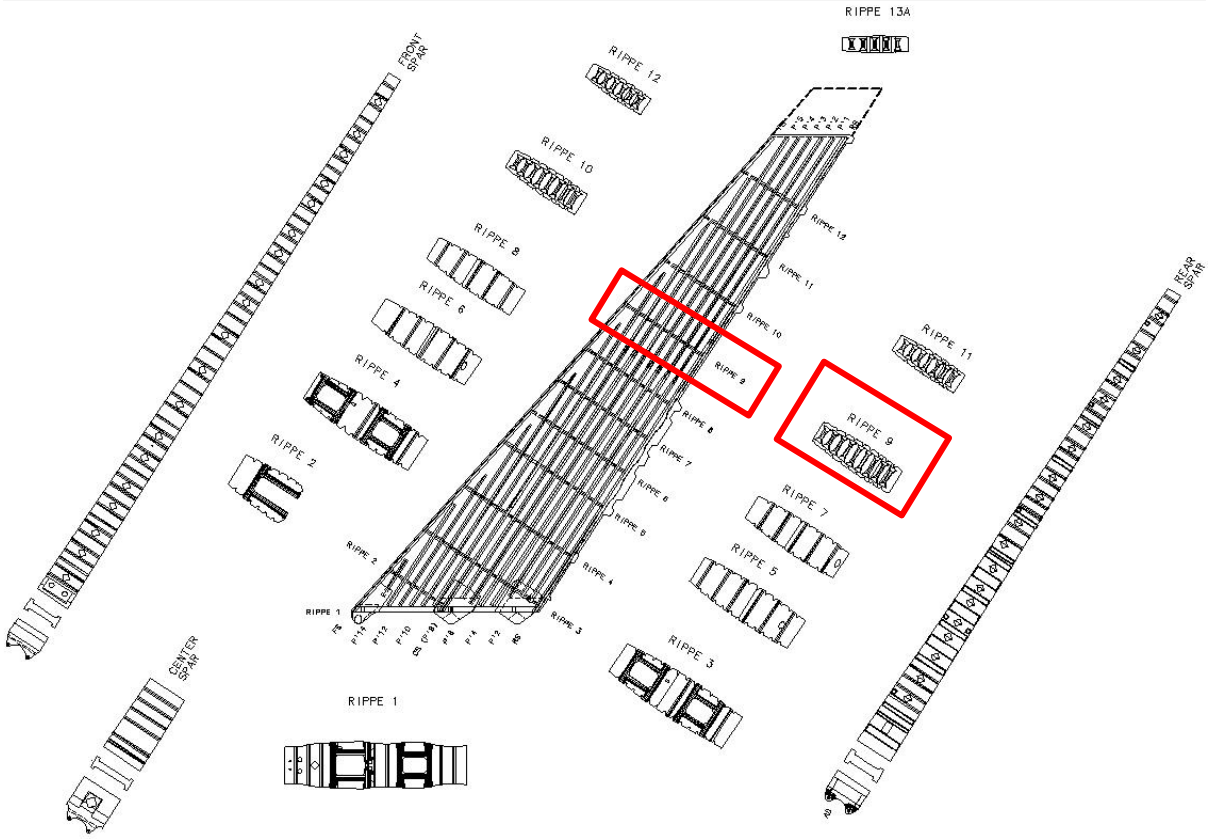


**Figure 2, Exploded view of the VTP Box, [2]**

The driving design requirement for the ribs is structural stability, i.e. buckling. In order to protect the ribs from buckling one solution is to reinforce them with stiffening elements. Conventional thin-walled aircraft components are reinforced against buckling by the use of stiffeners. An alternative approach is to incorporate the stiffener integrally as part of the rib. One possibility for such a stiffener is a bead. In the case of rib 9 of the VTP, beads are applied as stiffeners (Figure 3).

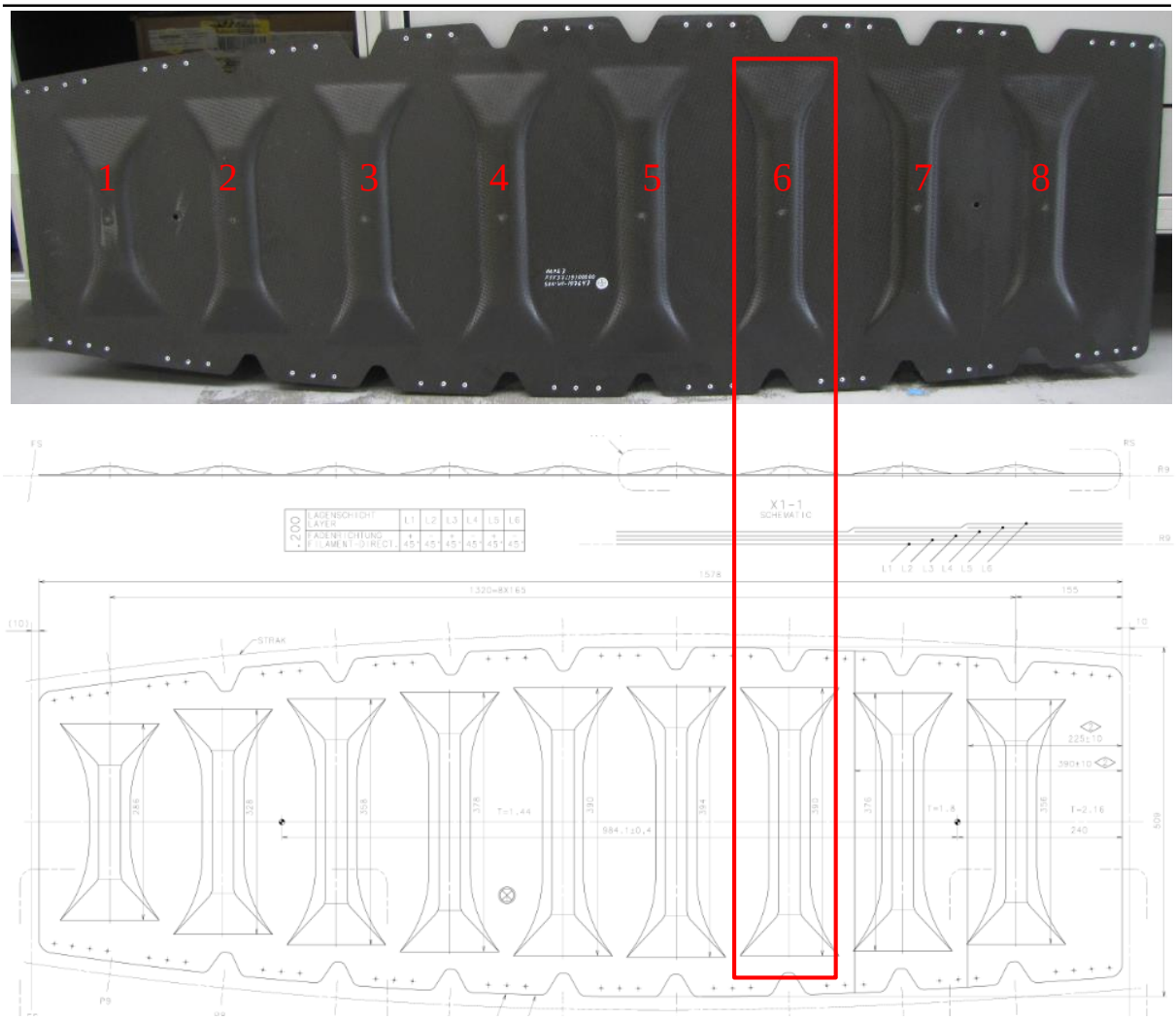


**Figure 3, Overview of the VTP box rib 9, [1]**

A schematic representation of the VTP box rib 9 bead is given in Figure 4. One characteristic feature of the bead-stiffener is the corner radius. The mechanical properties of the bead corner radius influence the rib buckling load. Therefore, if the bead corner radius mechanical properties are changed, the rib buckling load is potentially also changed.

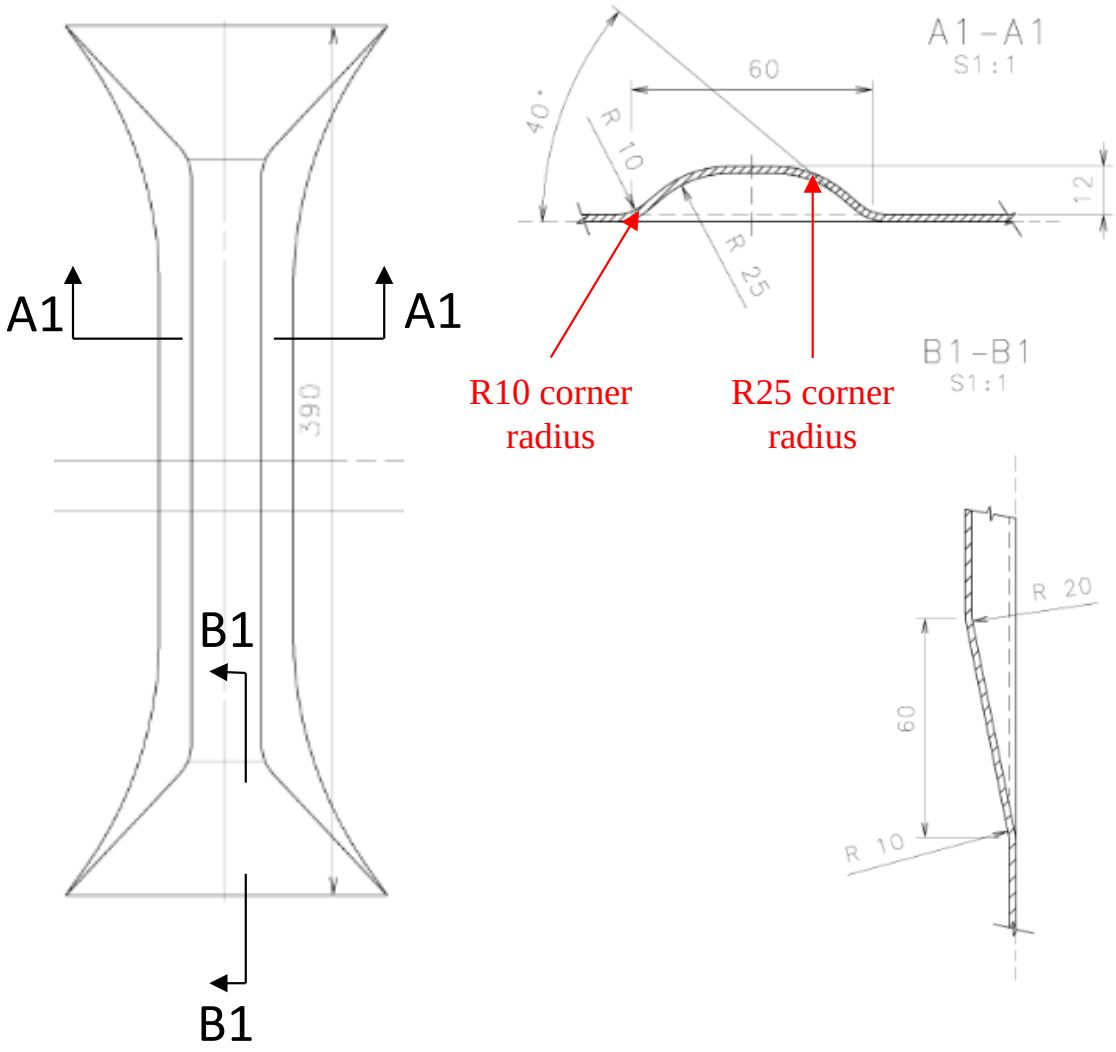


**Figure 4, Geometry of the VTP box rib 9 bead, [1]**

The use of integrated beads in composite structures is proved to generate up to 50% weight savings and 50% manufacturing time savings compared to a conventional structure (stringer-stiffened or sandwich ribs), [3, 4]. The main reason for these savings is the reduced number of parts and manufacturing operations.

For cost- and time-saving reasons the VTP ribs are manufactured by RTM 6 epoxy resin infusion of 5HS woven carbon fabric. The fabric layup consists of four plies all oriented at 45° with respect to the rib longitudinal axis (Figure 3). The cost- and time-savings are obtained, because the resin infusion can be automated to a higher degree compared to a hand lay-up or prepreg lay-up processes. Another advantage of the resin infusion process is the production of complex parts at intermediate volume rates and near-net shape, [5].

A challenge that exists for the lamination of complex geometries is to ensure proper draping of the composite layers through all radii. In case of the concave radii in the rib beads, it is possible that the fibers are not following the radii as preferred (Figure 5). Consequently, fiber bridging around the corner radii occurs leading to the formation of resin rich areas.

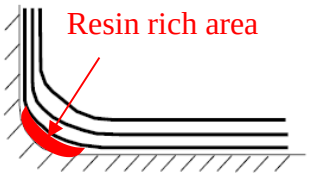


**Figure 5, Example of fiber bridging, [6]**

During visual inspection of rib 9, cracks are observed in the resin rich area of the rib bead (Figure 6 and Figure 7). It is discovered by test and analysis that the cyclic stress caused by the thermal load is the driver of this damage, [7]. Tests and analysis have shown that the damage has no impact on the structural load carrying capabilities. However, it is expensive and time consuming to perform component test to evaluate the impact of the damage on the structure. Especially, because thermal cycling is a slow test procedure. In order to investigate this type of damage, it would save a lot of time and money, if these tests could be performed on coupon level and by using a mechanical load cycle. Using a coupon test will save costs compared to a component test, and it is easier to test more parameters in a relatively easy way. Moreover, a coupon tests can be used to evaluate more directly the impact on the mechanical properties of the material. This impact can be used as input in the FEM model of the rib to evaluate the impact on component level. Using a mechanical load cycle will reduce the test duration, but also simplifies the test procedure.

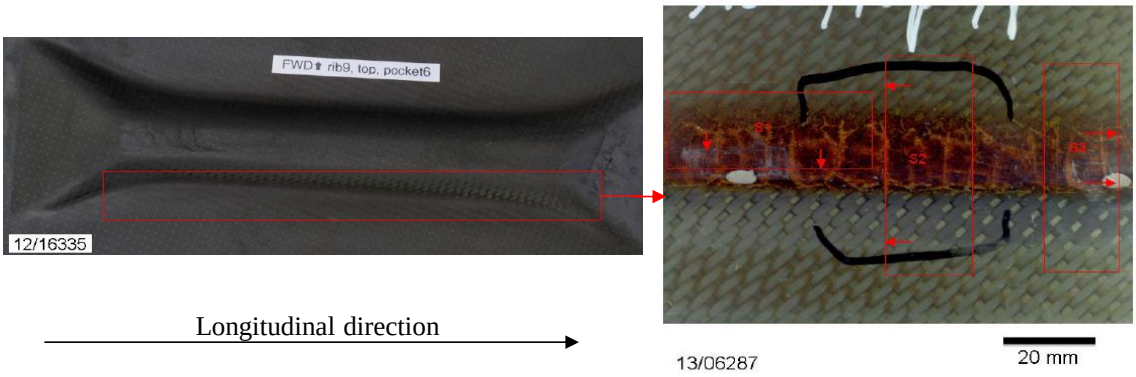


**Figure 6, Bead corner radius in-service damage and cross-sectional positions, [8]**

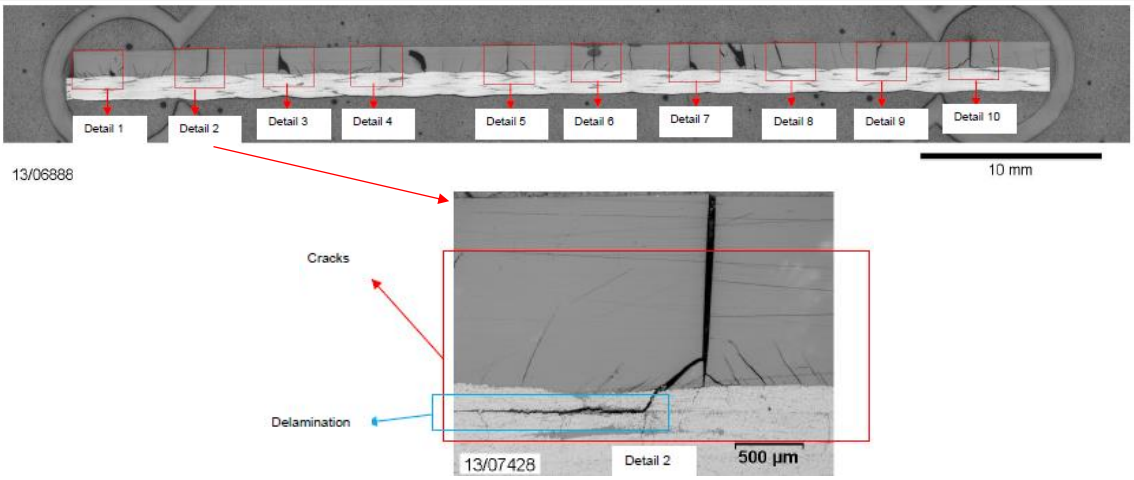


**Figure 7, Bead corner radius S1-S1 cross-section in-service damage, [8]**

During the course of this research it is calculated by FEA that the matrix thermal stress cycle at the resin rich layer interface with the first fabric ply in the bead varies between 32 MPa to 41 MPa, respectively for minimum and maximum thermal cyclic load (Chapter 3). This matrix stress cycle in the bead provides a stress amplitude of 5 MPa and an R-ratio of 0.78.

It is also discovered that a typical thermal cyclic test frequency is 0.00015 Hz, [7]. It takes 39 days to test a real structure or a specimen up to 500 thermal cycles. In contrast, a typical frequency of a mechanical cyclic test is 5 Hz, which only takes 1 minute and 40 seconds for 500 cycles, [9]. The mechanical fatigue test is about 33 333 times faster than the thermal fatigue test.

A few fundamental differences between the thermal and the mechanical load exist. In the first place, it is the way the load is applied. The thermal load loads the material biaxially. On the other hand, the mechanical load is most often uniaxial since biaxial mechanical loading requires complex test set-up . Another effect of the thermal load, which is not present in the mechanical load, is the low temperature material embrittlement.

The damage evolution in the resin rich bead corner radii is not yet completely investigated. Therefore, a main goal of this project is to investigate the damage development under in-service thermal fatigue loading conditions. However, the thermal cycling is a time-consuming process. Therefore, to investigate the damage accumulation, a process faster than the thermal cycling test is required. A mechanical cyclic test is needed as a faster alternative of the thermal cyclic test.

Many damage models (numerical, physics based analytical and phenomenological analytical) for laminated composites exist. Unfortunately, none of them can be applied to completely describe the damage evolution. All of them are valid only under strictly defined sets of conditions (e.g. layup, materials, and environmental conditions). This is one of the driving reasons that aircraft composite structures are designed following the “no damage growth” requirement. Therefore, a simple plane stress FE analysis is needed in this project to gain insight into the stresses driving the damage initiation. Following the problem introduction the research questions are formulated:

1. Is it possible to replicate the bead resin rich area thermal fatigue stress cycle in a simple coupon specimen loaded in mechanical tension-tension?
2. Which parameters drive the fatigue damage initiation?
3. Where does the fatigue damage initiate?
4. How does the fatigue damage accumulate in the laminate?
5. How does the fatigue damage affect the laminate mechanical properties?

In order to answer the research questions, a combined approach consisting of numerical analyses and physical tests is chosen. The numerical analysis is a basic FE stress analysis without complex damage growth modeling. A limitation of this choice is that it can only be used to investigate the damage initiation, but not its growth. However, from a practical standpoint it is easier for analytical validation. The investigated parameters are the stresses in the real structure and the specimens and their fatigue parameters (amplitude and R-ratio). The investigated stresses are the matrix longitudinal stress and the interlaminar stress at the resin rich layer interface with the first fabric ply.

The physical tests are only mechanical uniaxial tensile with applied constant temperature. A limitation of the mechanical test is that it is not able to completely replicate all effects of the thermal test. The tested coupon specimens have one-sided resin rich layers and flat geometry. This simplifies the geometry enough (no radius) to make the testing easier and simultaneously keeps the layup similar to the real structure. The aim of the physical tests is to investigate the damage evolution and to correlate the damage initiation with the numerical stress analysis. The damage is observed through optical microscopy of representative cross-sections.

It is discovered that the bead resin rich layer thermal stress cycle cannot be replicated mechanically, but the fatigue damage can. Moreover, the fatigue damage can be replicated faster. The fatigue damage is found to initiate below the resin rich layer surface. The matrix R-ratio and stress amplitude at the resin rich layer interface with the fabric are found to be potential fatigue driving parameters. In addition, the fatigue damage is found to develop in the form of cracks and delamination, penetrating through the laminate thickness. Moreover, similar damage is observed in the bead and the tested composite specimens. The accumulation of the fatigue damage is discovered to result in laminate stiffness reduction.

In order to build-up the path towards answering the research questions, the report layout follows the hereby described chapter sequence. Chapter 1 provides an introduction to the research problem. Chapter 2 reviews the scientific work related to the problem. Chapter 3 describes the finite element modeling performed for the project. Chapter 4 describes the specimen manufacturing, including geometry. In chapter 5 the test matrix, methodology and results are presented. The obtained results in the course of the research project are cross-correlated and discussed in chapter 6 and conclusions and recommendations are drawn in chapter 7.

# 2. Literature review

## 2.1. Chapter introduction

This chapter presents a review of the knowledge relevant to the development of this project. The literature reviewed here forms the fundamental knowledge and describes the current state-of-the-art necessary for the research.

Three major areas for this literature review are identified from the introduction. First, is the fatigue damage in composites. It is divided into four sub-areas, namely damage scales, damage modes, damage accumulation impact on the laminate and comparison of the thermal fatigue and the mechanical fatigue in composites. Second, is the necessity to review the available test methods applicable to composites. Finally, the RTM 6 epoxy related literature is reviewed, because RTM 6 is used as matrix material in the investigated rib. The RTM 6 temperature dependent properties are reviewed. Typical values of RTM 6 residual thermal stresses in composites from manufacturing are reviewed.

One topic that is not used in the research, but is useful for further research activities beyond this project is briefly reviewed. It is the non-linear RTM 6 material stress-strain models.

## 2.2. Fatigue damage in composites

### 2.2.1. Scales

Several length scales exist in laminated composite analysis as illustrated in Figure 8. Three of them are associated with the investigated composite damage in this research – micro-scale (fiber and matrix level, approximately 0.01 mm), meso-scale (ply or laminate level, approximately 0.1 mm) and macro-scale (component level, more than 1 mm). A major difficulty in composite design and analysis is to establish a link among all length scales.

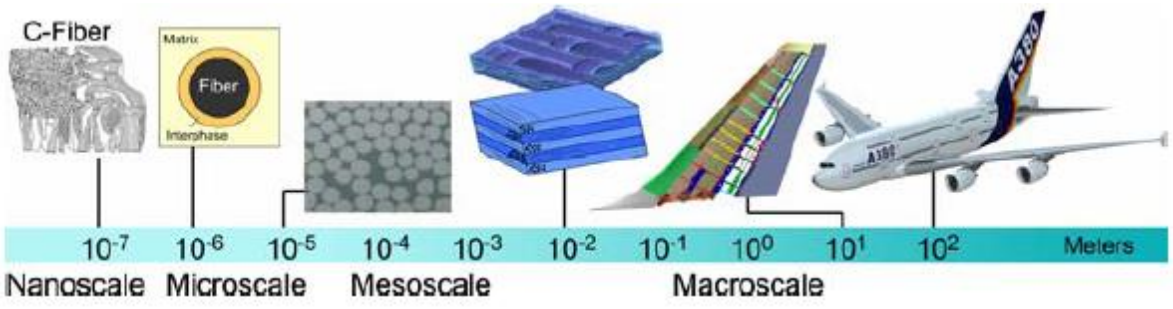


**Figure 8, Composite length scales, [10]**

### 2.2.2. Fatigue damage modes

Many scientific papers research both static and fatigue damage modes in Uni-Directional (UD) laminates. However, there is scarce of research investigating damage modes in woven fabric reinforced laminates. The number of articles investigating fatigue in woven fabric reinforced

laminates is even smaller. Therefore, all reviewed knowledge in this section is mainly related to UD laminates.

The composite damage modes are fiber-dominated and matrix-dominated. Fatigue loading creates predominantly matrix-dominated damage. A few matrix-dominated pure damage modes occur in a laminate – micro-cracking (at micro-scale), cracking (at meso-scale) and delamination (at meso-scale). Often they occur together, thus yielding interactive damage modes – Matrix Crack Induced Micro-cracking (MCIM) and Matrix Crack Induced Delamination (MCID), [11].

The pure damage mode development usually starts with matrix micro-cracking. It potentially leads to loss in laminate stiffness and sometimes to complete laminate failure. Micro-cracks can also initiate from a propagating crack, thus creating MCIM (Figure 9), [11].

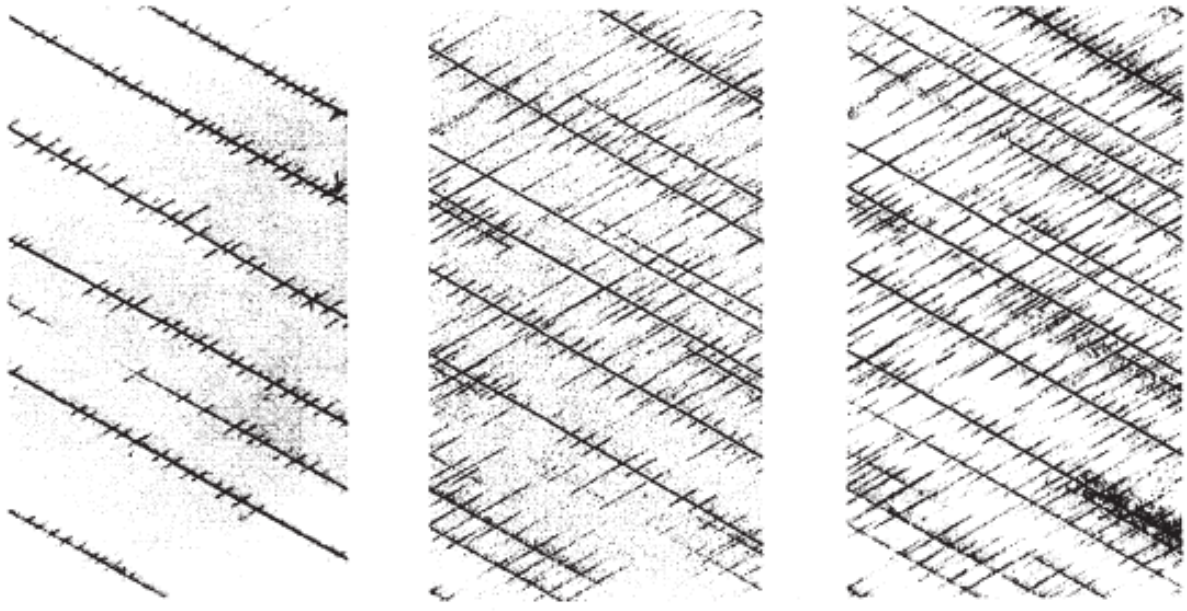

**Figure 9, MCIM observed by in-plane X-radiography at increasing load level (from left to right), [11]**

The other interactive damage development scenario is MCID (Figure 10). Two MCID development scenarios are possible, [11, 12]. The first scenario is an intraply through-the-thickness crack to deflect into interlaminar delamination. The second scenario is two through-the-thickness cracks located in adjacent plies to coalesce at the ply interface, thus creating a delamination connecting the cracks. Cracking frequently precedes delamination when the inner part of the laminate is considered.

Two phenomena govern the MCID initiation, [11, 13]. First, the stresses at a crack tip have similar nature to the laminate free-edge stresses. High out-of-plane tensile peel stress is generated due to the discontinuity. Second, the cracked ply carries much less load, thus loading the adjacent plies more heavily. This further amplifies the peel stress, which facilitates the MCID initiation.

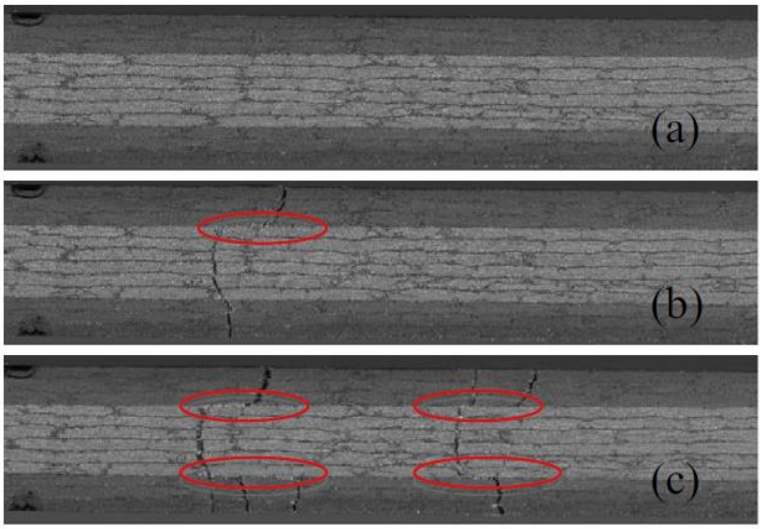


**Figure 10, MCID observed by microscopy, [12]**

### 2.2.3. Fatigue damage impact on a laminate

A damage mode that causes major reduction in the shear buckling load of a laminate is the delamination, [14, 15]. It can potentially decrease the buckling load with up to 70% in the worst-case scenario. The worst-case scenario is the delamination to propagate along the whole width of the laminate. On the other hand, there is a possibility the delamination to be confined within a small area inside the laminate without propagating to the edges. If this central delamination has width of less than 20% of the laminate total width, the reduction in the buckling load is negligible (less than 10%), Figure 11.

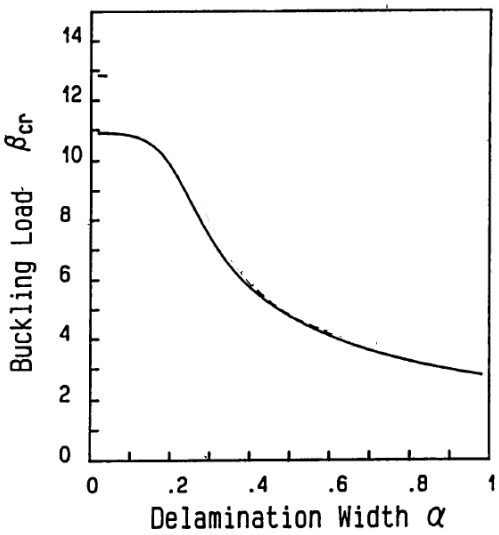


**Figure 11, Buckling load of plate with a center delamination dependency on the normalized delamination width, [14]**

Another way of impacting the laminate mechanical properties is by reducing its stiffness, [16]. The laminate stiffness could be reduced by accumulating damage. The accumulated damage consists mainly of cracks.

### 2.2.4. Thermal fatigue vs. mechanical fatigue of composites

There are some fundamental differences between the thermal and mechanical cyclic loads, [17]. The thermal fatigue load is biaxial compared to the mechanical fatigue load, which is uniaxial. The typical mechanical fatigue load is uniaxial tension-tension. On the other hand, the thermal cyclic load has effects on the material, which are not present in its mechanical counterpart, such as thermal embrittlement of the matrix at low temperatures.

One parameter used for the comparison of mechanical and thermal fatigue is the crack density. A typical crack density dependency on the number of tested cycles for thermal and mechanical fatigue is presented in Figure 12. The crack densities after the test are similar. Moreover, they both reach almost the same saturation levels, [18]. However, the crack kinetics (i.e. crack development rate) is different.

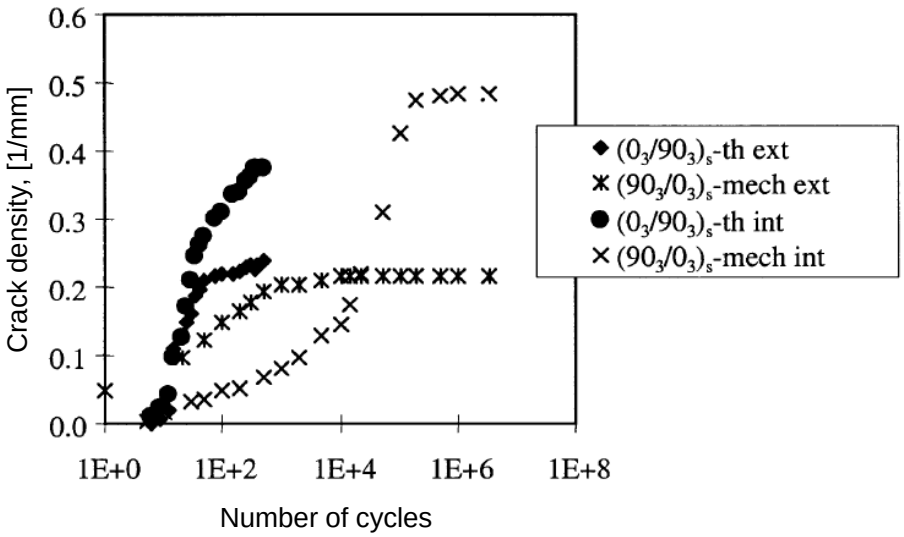


**Figure 12, Crack density-number of cycles data points for mechanically and thermally fatigued cross-ply laminate at comparable stress levels, [18]**

The crack kinetics is much faster under thermal cycling (the cycle is from (-50)°C to 20°C) compared to mechanical cycling (Figure 13), [18, 19]. Under thermal fatigue the cracks reach saturation level after approximately 500 cycles. In contrast, under mechanical fatigue the cracks require more than 50000 cycles to reach similar saturation level for comparable stress cycle.

Besides the matrix biaxial stress state and the matrix embrittlement at low temperatures during thermal cycling, there is one more difference – the load frequency (Figure 13). The thermal cycling frequency is 0.00015 Hz on average compared to 5 Hz or 10 Hz of mechanical cycling frequency. It is observed that lowering the mechanical cycling frequency to the thermal cycling

frequency yields substantially increased crack density after low number of cycles (e.g. 500 cycles, when the thermal cycling crack saturation level is reached).

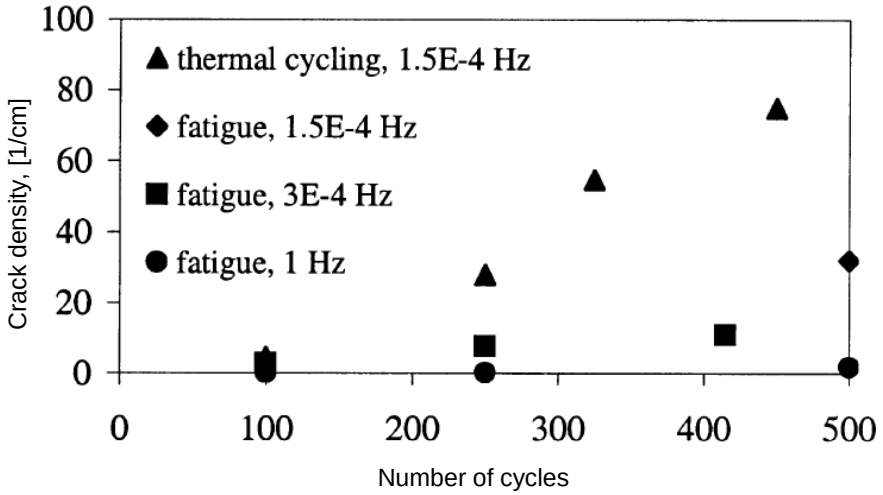


**Figure 13, Crack density-number of cycles data points for mechanically and thermally fatigued cross-ply laminate at different frequencies, [18]**

One explanation of the observed crack retardation (i.e. crack density increase delay) in the mechanical fatigue case is the Le Chatelier's principle, [19]. According to this principle, by mechanically loading the epoxy matrix stress activated post-curing is induced. It potentially toughens the material and "heals" its flaws, resulting in crack development retardation. It is proven by testing that post-cured laminates exhibit slower crack development compared to laminates cured at a standard production cycle without post-curing. Post-curing also reduces the matrix residual tensile stress from manufacturing, [20].

Another criterion for comparing the thermal and mechanical cycling is the total test duration. Thermal cycling up to 500 cycles with 0.00015 Hz frequency takes about 39 days. In contrast, mechanical testing up to 500 cycles with 5 Hz frequency takes about 1 minute and 40 seconds. The mechanical fatigue test is about 33 333 times faster.

To summarize, four phenomena differentiate thermal fatigue from mechanical fatigue – biaxial vs. uniaxial load, thermal degradation, low temperature matrix embrittlement and the Le Chatelier's principle. One way to mechanically replicate the low temperature matrix embrittlement is by performing the mechanical fatigue test at negative temperature in a climate chamber. However, peculiarly the crack density development rate at different temperatures after the same number of cycles is the same (Figure 14).

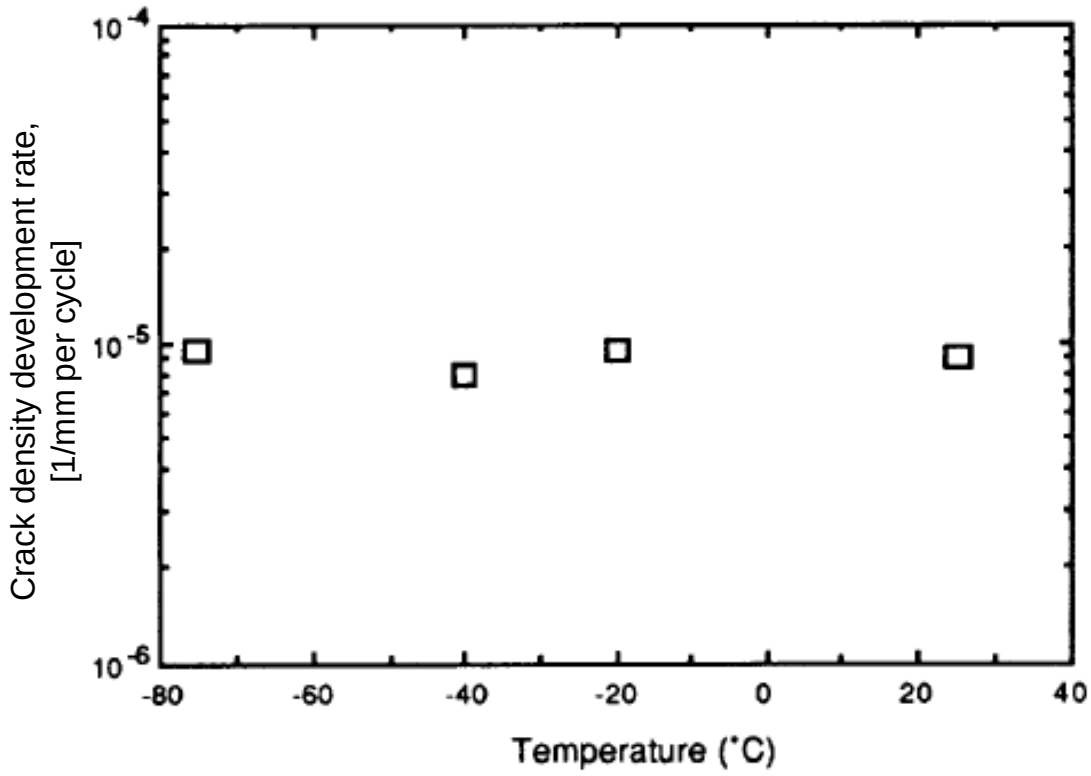


**Figure 14, Crack density development rate-temperature data points for mechanically fatigued laminate at the same stress level and same number of cycles, but at different temperatures, [19]**

## 2.3. Testing of composites

The most common standards for testing of laminated composites are defined by the American Society for Testing and Materials (ASTM). Two types of ASTM standards are of particular interest – for static composite testing and for fatigue composite testing. The geometry of the specimens for both types is almost always the same – a rectangular shape. The main difference is the cyclic load in the fatigue testing instead of static loads in the static testing, [9, 21].

The most commonly used way of statically testing the in-plane shear properties of a laminate is by the use of the ASTM standard for testing of ±45° stacked laminates, [22]. On the other hand, the most commonly used way of fatigue testing in general is by a simple tension-tension cyclic test, as in the ASTM standard for testing the fatigue properties of laminates loading them in cyclic tension-tension, [9]. This means that a combination of both would be convenient to test in a simple way the in-plane shear fatigue properties of a laminate.

## 2.4. RTM 6 epoxy

The matrix material used in this research is the RTM 6 epoxy system. Therefore, this section reviews the relevant literature related to RTM 6.

### 2.4.1. Temperature dependent properties of pure RTM 6 epoxy

**Experimental data**

RTM 6 is a degassed, 180°C premixed mono-component epoxy resin. It has low viscosity at processing temperature, which makes it suitable for Resin Transfer Molding (RTM) and Vacuum Infusion (VI) manufacturing processes. The RTM 6 in-service temperature range is from (-60)°C up to 120°C, [23]. This wide manufacturing and in-service temperature range arouses interest in the RTM 6 temperature dependent properties. Four RTM 6 properties exhibit temperature dependency – the Young's modulus, the yield and failure stresses and the Coefficient of Thermal Expansion (CTE), [24, 25].

Typical temperature dependent stress-strain curves are shown in Figure 15. The RTM 6 becomes more brittle and stronger, when the temperature is decreased. Test stress-strain data of RTM 6 for negative temperatures is not available in the literature. However, the observed trend is expected to be able to be extrapolated for negative temperatures, because the trend for epoxy resins in general is observed not to change (Figure 16).

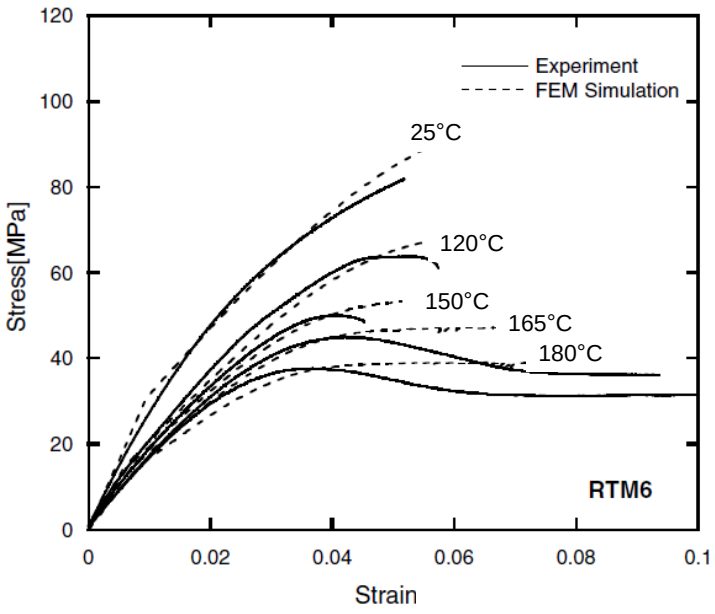


**Figure 15, RTM 6 stress-strain curve temperature dependency obtained by tensile test and Finite Element Analysis (FEA), [24]**

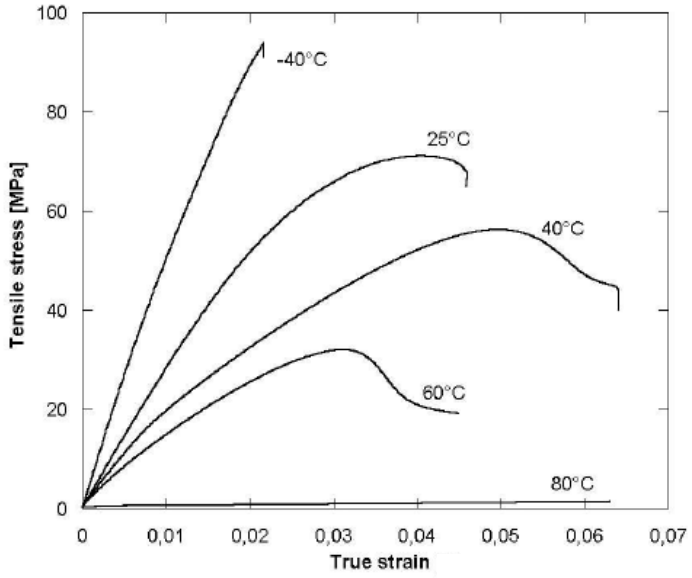


**Figure 16, L135i epoxy stress-strain curve temperature dependency obtained by tensile test, [26]**

The Young's modulus exhibits inverse temperature dependency (Figure 17). When the temperature is decreased, the modulus is increased (i.e. the resin becomes stiffer and more brittle). The modulus behavior is measured by Dynamic Mechanical Thermal Analysis (DMTA) calibrated at Room Temperature (RT) by a static tensile test of RTM 6 dog-bone specimens. The modulus behavior at different temperatures is validated by tensile tests (Figure 15).

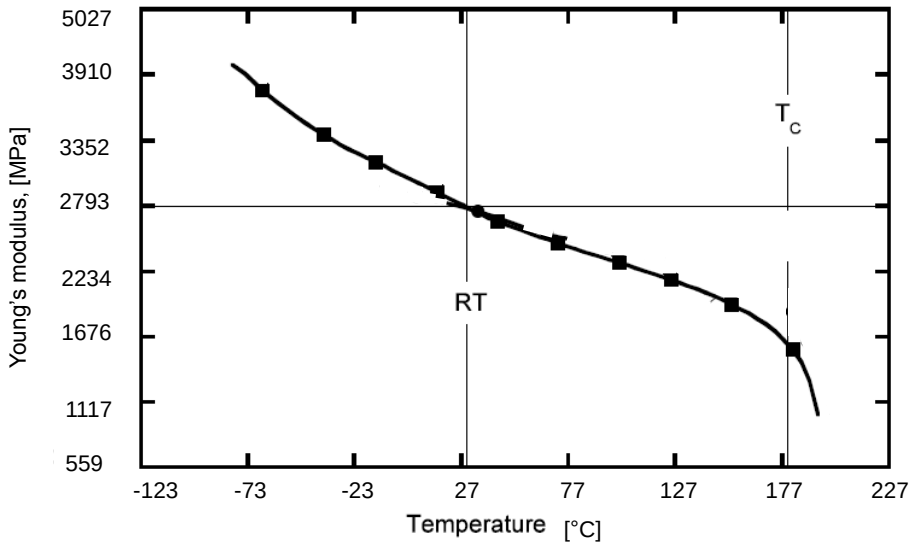


**Figure 17, RTM 6 Young's modulus temperature dependency obtained by DMTA, [24]**

The yield and failure stresses also exhibit inverse temperature relationship (Figure 18), while the CTE exhibits direct temperature relationship (Figure 19). The CTE temperature dependency however shows scatter, when approaching the RT. A summary of the RTM 6 mechanical properties at RT obtained from different sources is presented in Table 1. They are used in the FE analysis as described in chapter 3.

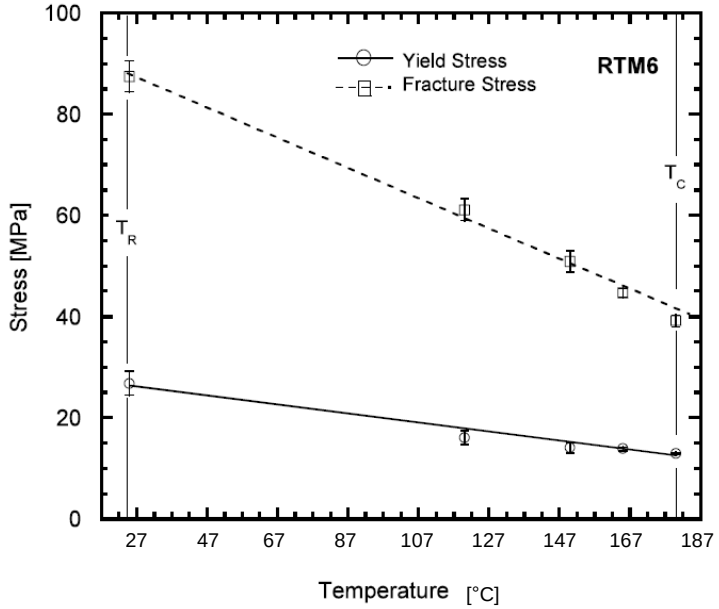


**Figure 18, RTM 6 yield and failure stress temperature dependency obtained by tensile test, [24]**

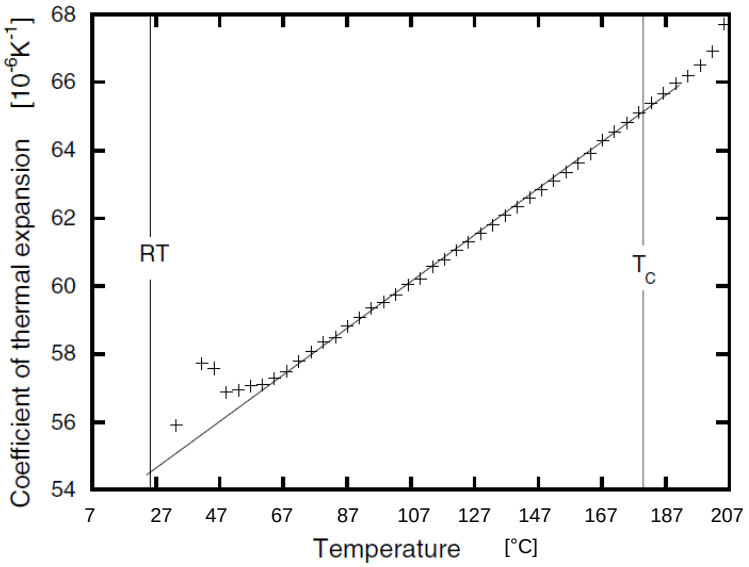


**Figure 19, RTM 6 CTE temperature dependency obtained by Thermal Mechanical Analysis (TMA), [24]**

**Table 1, Summary of the RTM 6 epoxy isotropic mechanical properties at RT**

| Property | Unit | Source | | |
|---|---|---|---|---|
| | | [24] | [25] | [23] |
| T | [°C] | RT | RT | RT |
| Poisson's ratio | [-] | 0.38 | 0.38 | N/A |
| Young's modulus | [MPa] | 2793 | 2760 | 2890 |
| Shear modulus | [MPa] | 1227 | 1000 | N/A |
| Yield stress | [MPa] | 27.0 | 27.0 | N/A |
| UTS | [MPa] | 87.5 | 87.5 | 75.0 |
| CTE | [1/°C] | 62[1] | 54.5 | 52.7 |

**Stress-strain behavior modeling**

The RTM 6 non-linear stress-strain behavior can be modeled approximately with an elastic-plastic material model, [25]. In order to do that, a three-parameter hyperbolic tangent function or a two-parameter work-hardening function is used. The model is valid for the 25-180°C temperature range. This model is not used in the FE modeling part of this project, but is useful information in case the research is expanded upon later.

### 2.4.2. Residual stresses in RTM 6-based composites

**Formation**

Residual stresses build-up due to constrained volumetric shrinkage of the RTM 6 resin during the manufacturing process. Two build-up stages of residual stresses are found in the literature (Figure 20), [24, 27]. The first stage is during the isothermal curing phase at elevated temperature. The second stage is during cooling down from curing to RT.

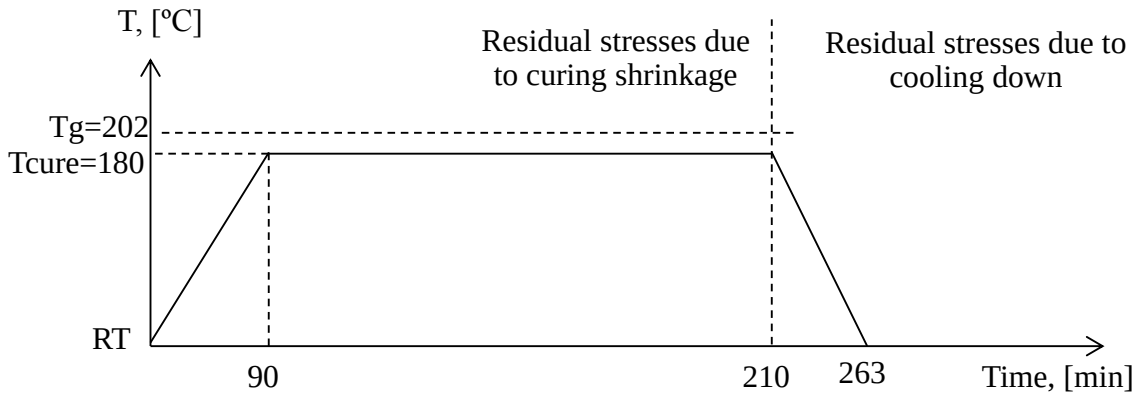


**Figure 20, RTM 6 residual stress build-up stages during the manufacturing cycle**

[1] For T<148°C

The volumetric shrinkage of an unconstrained resin is schematically represented in Figure 21. The two stages are clearly visible. The constrained volumetric shrinkage of the RTM 6 resin is responsible for the residual stress accumulation.

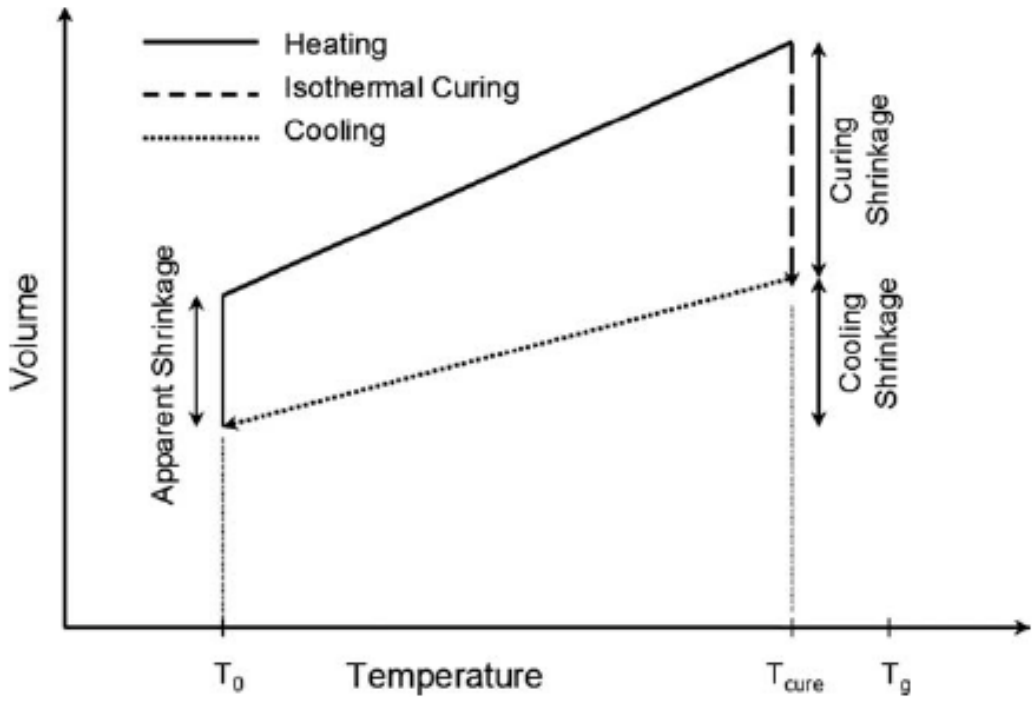


**Figure 21, Typical unconstrained epoxy volumetric shrinkage behavior during manufacturing, [28]**

The first stage of curing chemical shrinkage is attributed to the formation of chemical bonds between the atoms of the matrix, [27]. During curing a polymerization reaction takes place. The polymerization reaction forces the polymer molecular chains to cross-link. Moreover, this cross-linking process packs the atoms closer together, thus reducing the resin volume. On a macroscopic scale this is seen as resin solidification with an increase of its density (i.e. shrinkage).

The fibers have high stiffness and close to zero CTE, [29]. Therefore, the fibers constrain the matrix and prevent it from shrinking during curing. This leads to residual tensile stress accumulation. Moreover, the fiber CTE is even slightly negative, which further amplifies this effect and increases the residual stresses.

The second stage of cooling down is attributed solely to the thermal shrinkage due to the transition from curing to room temperature. It is characterized by the CTE and the glass transition temperature (Tg). The matrix residual stresses build-up onset point for this second stage usually starts at the curing temperature, because it is lower than the Tg (Figure 21). Similarly to the first stage the fibers apply a constraint to the matrix, thus preventing it from shrinking upon cooling and inducing tensile residual stresses.

**Influencing factors**

Two factors affect the residual stresses. The first factor is the 3D stress state of the resin inside the laminate on a microscopic level. It is shown by tests that the 3D stress state reduces the resin uniaxial strength with approximately 40%, [27]. The second factor is the stress relaxation in time. It is shown only by calculations that the residual stresses can be decreased with up to 30% due to their relaxation, [30].

## 2.5. Chapter outcomes

Information regarding fatigue damage modes in composites is found in the literature. The reviewed scientific papers use specimens made out of specific laminates most of which are UD and are subjected to specific load cases. Static and fatigue damage modes in these laminates are reviewed. Moreover, damage accumulation effects on these laminates are reviewed. Comparison of mechanical and thermal cycling of laminates is also performed. However, no papers review the fatigue damage in 5HS woven carbon fabric laminate infused with RTM 6 epoxy subjected to the relevant to this research set of conditions and loads. Moreover, there are no papers reviewing the replication of thermal stresses by applying mechanical load for the current laminate configuration and load case. Therefore, further research to fill in this knowledge gap is required.

Standard ASTM test methods for testing laminates and laminates with pure ±45° orientations statically and in fatigue are found. However, no standards describing how thermal stresses could be replicated by applying mechanical load to accelerate the testing are found. Therefore, a non-standardized test is required, which means further research to fill in this knowledge gap is also required.

Information regarding the RTM 6 temperature dependent properties is found in the literature. Moreover, a residual matrix stress formation mechanism is found. However, there are no papers reviewing the residual stress values resulting from the application of the current load case to 5HS woven fabric infused with RTM 6 resin. Therefore, further research to fill in this knowledge gap is required.

# 3. Finite element modeling

## 3.1. Chapter introduction

This chapter describes the finite element modeling part for this project. First, the FE models are described. Second, the FEA results are presented.

The goal of the FEA described in this chapter is to match the stresses in the bead to those in the specimen. However, this goal cannot be completely reached for one specimen. Therefore, a few specimen types subjected to a few load cases are used instead of only one configuration. Another goal is to calculate the fiber residual compressive stress difference of specimen type C between 26°C and (-20)°C.

To reach the defined goal, two models are created – one of the bead and one of the composite specimen. The thermal load of the bead is directly taken from the aircraft thermal cycle description. The mechanical loads of the composite specimens are the experimentally determined loads in chapter 5.

Both models use shell elements and a pure plane stress response. It turns out that pure plane stress response yields acceptable results, because the laminate layers are sufficiently thin (less than 1 mm). Two types of loads are applied to the FE models – thermal load and mechanical tensile load. The investigated parameters are the in-plane stresses layer-by-layer.

## 3.2. Models

### 3.2.1. Finite element modelling technique used in all models

The same FE modelling technique is used for all models. ABAQUS 6.12-3 commercial FEA package is used as software for performing the finite element analysis. The performed numerical analyses are geometrically linear, because of the small displacements (within 1 mm).

The models are meshed using fully integrated quadrilateral conventional shell elements (denoted in ABAQUS as type S4). This type of element has only a membrane (i.e. in-plane) stress response, which is sufficient as an output from the analysis. S4 elements are not subjected to bending or membrane hourglass modes, [31]. This implies that it is not overly sensitive to element distortion and does not suffer from parasitic locking. A composite layup, integrated during the analysis, is assigned to each element.

In order to perform the mesh convergence study, the element size is decreased. The mesh convergence study is presented in Table 2. The mesh convergence study is performed for the stresses at the resin rich layer interface with the first fabric ply of the bead FE model, which is described in details in section 3.2.3. The investigated stresses show no change when the element size is decreased.

**Table 2, Mesh convergence study of the stresses at the resin rich layer interface of the bead FE model**

| Element size | Number of elements | $S22_{matrix}$ | $S22_{fiber}$ | $S11_{matrix}$ | $S11_{fiber}$ | $S12_{matrix}$ | $S12_{fiber}$ |
|---|---|---|---|---|---|---|---|
| [mm] | [-] | [MPa] | [MPa] | [MPa] | [MPa] | [MPa] | [MPa] |
| 4 | 4242 | 36 | -101 | 27 | -101 | 0 | 17 |
| 3 | 7695 | 36 | -100 | 27 | -100 | 0 | 17 |
| 2 | 16632 | 36 | -99 | 27 | -100 | 0 | 17 |

Two different materials are used in the FE models – RTM 6 isotropic matrix and RTM 6 matrix/HexForce G0926 D fabric reinforced anisotropic lamina. The mechanical properties of both materials are presented in Table 3 and Table 4.

**Table 3, Cured RTM 6 matrix isotropic mechanical properties**

| Property | Unit | Value | Source |
|---|---|---|---|
| Young's modulus | [MPa] | 2890 | [23] |
| Poisson's ratio | [-] | 0.35 | [24, 25] |
| CTE | [1/°C] | 52.7E-6 | [23] |
| UTS | [MPa] | 75 | [23] |
| Shear strength | [MPa] | 52 | [32] |

**Table 4, Cured RTM 6/HexForce G0926 D lamina anisotropic homogenized mechanical properties**

| Property | Unit | Value | Source |
|---|---|---|---|
| Young's modulus (warp and weft) | [MPa] | 64500 | [33] |
| Shear modulus | [MPa] | 4200 | [33] |
| Poisson's ratio | [-] | 0.05 | [33] |
| CTE (warp and weft) | [1/K] | 3.4E-6 | [32] |
| UTS (warp and weft) | [MPa] | 860 | [23] |
| Compressive strength (warp and weft) | [MPa] | 680 | [23] |
| In-plane shear strength (warp and weft) | [MPa] | 95 | [23] |

The use of S4 type shell elements is validated with Classical Lamination Plate Theory (CLPT). A plate is modelled both in ABAQUS and analytically with CLPT code written in MATLAB, [32]. The validation is performed for five load cases. The plate has sufficiently large dimensions to achieve stress homogeneity in the middle (i.e. it is representative for an infinite laminate). The load cases consist of different combinations of tensile, shear and thermal loads. The thermal

load in all load cases is a constant predefined temperature field of (-154)°C. The stresses in the fibers and the matrix are compared (Table 5). The stresses in both composite constituents are equivalent in both the numerical and the analytical model for all load cases. Consequently, the use of S4 type shell elements is validated.

**Table 5, FE modeling validation with CLPT (all load cases have additional constant thermal load)**

| Load case | N11 | N22 | N12 | Calculation method | $S11_{fiber}$ | $S11_{matrix}$ | $S12_{fiber}$ | $S12_{matrix}$ | $S22_{fiber}$ | $S22_{matrix}$ |
|---|---|---|---|---|---|---|---|---|---|---|
| [-] | [N/mm] | [N/mm] | [N/mm] | [-] | [MPa] | [MPa] | [MPa] | [MPa] | [MPa] | [MPa] |
| Uniaxial tension | 100 | 0 | 0 | ABAQUS | 34.571 | 34.571 | -24.477 | 8.502 | -3.974 | 0.000 |
| | | | | CLPT | 34.571 | 34.571 | -24.477 | 8.502 | -3.974 | 0.000 |
| Biaxial tension | 100 | 200 | 0 | ABAQUS | 103.714 | 103.714 | 24.477 | 0.554 | 13.030 | 0.000 |
| | | | | CLPT | 103.714 | 103.714 | 24.477 | 0.554 | 13.030 | 0.000 |
| In-plane shear | 0 | 0 | 100 | ABAQUS | 74.086 | -74.086 | 0 | 0 | 0 | 2.582 |
| | | | | CLPT | 74.085 | -74.085 | 0 | 0 | 0 | 2.582 |
| Uniaxial tension + in-plane shear | 100 | 0 | 100 | ABAQUS | 108.658 | -39.915 | -24.477 | 8.502 | -3.974 | 2.582 |
| | | | | CLPT | 108.657 | -39.514 | -24.477 | 8.502 | -3.974 | 2.582 |
| Biaxial tension + in-plane shear | 100 | 200 | 50 | ABAQUS | 140.758 | 66.671 | 24.477 | 0.554 | 13.030 | 1.291 |
| | | | | CLPT | 140.757 | 66.672 | 24.477 | 0.554 | 13.030 | 1.291 |

### 3.2.2. Thermal load applied to all models

The same thermal load is used in all FE models. The thermal load is calculated by analyzing the thermal profiles defined by the fatigue test program of the VTP, [34]. Seven thermal profiles are provided. The most frequently occurring thermal profile is selected.

The thermal load is cyclic and is characterized by the minimum and maximum temperature for one cycle. In case of the selected thermal mission the upper temperature limit is 26°C and the lower limit is -20°C. If the residual stresses are assumed to build-up from a temperature generically denoted as $T_{zero\text{-}stress}$, then the thermal load temperature difference is expressed with Equation 1. For calculation of the thermal load $T_{zero\text{-}stress}$ is assumed to be equal to the resin curing temperature (Figure 20), because it is lower than $T_g$. A summary of the thermal loads is presented in Table 6.

$$dT_{min/max} = T_{min/max} - T_{zero-stress} \qquad \text{Equation 1}$$

**Table 6, Summary of the VTP thermal loads**

| $T_{cure}$=$T_{zero\text{-}stress}$ | $T_{min}$ | $T_{max}$ | $dT_{min}$ | $dT_{max}$ |
|---|---|---|---|---|
| [°C] | [°C] | [°C] | [°C] | [°C] |
| 180 | -20 | 26 | -200 | -154 |

### 3.2.3. Description of the model of the bead

An overview of the bead FE model is presented in Table 7. The geometry of the bead is presented in Figure 4. Two resin rich areas are modeled – one at the R10 corner and one at the R25 corner. The layup is presented in Figure 22. The bead laminate areas different from the resin rich areas use the same layup, but with a thin resin rich layer instead of thick layer. The thicknesses of the layers are presented in Table 15.

A pure thermal load case is used in the bead FE model. The load is a predefined temperature field. The boundary conditions of the bead FE model are all edges completely clamped (i.e. all DOF are constrained).

**Table 7, Overview of the bead FE model**

| Overview | Element size | Element type | Number of elements | Analysis type | Resin rich layer thickness | Interface resin layer thickness | Fabric ply thickness |
|---|---|---|---|---|---|---|---|
| [-] | [mm] | [-] | [-] | [-] | [mm] | [mm] | [mm] |
| 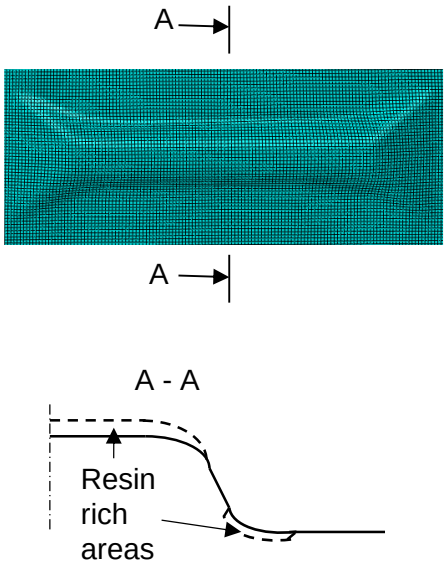 | 3 | S4 | 7695 | Linear | 1.500 | 0.050 | 0.360 |

| Resin rich layer |
|---|
| Fabric |
| Resin |
| Fabric |
| Resin |
| Fabric |
| Resin |
| Fabric |
| Resin |

| Resin |
|---|
| Fabric |
| Resin |
| Fabric |
| Resin |
| Fabric |
| Resin |
| Fabric |
| Resin |

| Resin |
|---|
| Fabric |
| Resin |
| Fabric |
| Resin |
| Fabric |
| Resin |
| Fabric |
| Resin rich layer |

**Figure 22, Bead FE model layups of: left – R25 corner radius, center – area without resin rich layer, right – R10 corner radius**

### 3.2.4. Description of the models of specimen types B, C and D

Three FE models corresponding to three specimen types B, C and D are created (see chapter 4). Specimen type B is produced in one step. Specimen type C is produced in two steps by co-bonding the resin rich layer in a second curing cycle. Specimen type D is the base laminate made in the first manufacturing step of specimen C and has no resin rich layer. The specimen geometry and manufacturing are presented in details in chapter 4 and their testing – in Table 16.

An overview of the specimen FE model is presented in Table 8. The in-plane geometry of the three models is the same (Figure 34). The layup stacking sequence is also the same (Figure 35). However, different layer thicknesses are used. The thicknesses are based on real measurements described in section 4.7. To switch from one specimen type to another only the layer thicknesses are changed.

One load case is applied to the specimen models – combined thermal-mechanical load case. The thermal load is applied as a predefined temperature field. The mechanical load is applied as a concentrated force at a point, which is kinematically coupled to the right tab area.

The same boundary conditions are applied to the specimen models. The left tab area is clamped (i.e. all DOF are constrained). The right tab area is allowed to move only in-plane (i.e. all out-of-plane DOF are constrained).

**Table 8, Overview of the FE models of specimen types B and C**

| Specimen | Overview | Element size | Element type | Number of elements | Analysis type | Resin rich layer thickness | Interface resin layer thickness | Fabric ply thickness |
|---|---|---|---|---|---|---|---|---|
| [-] | [-] | [mm] | [-] | [-] | [-] | [mm] | [mm] | [mm] |
| Type B | 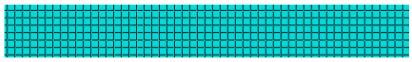 | 1 | S4 | 6500 | Linear | 0.970 | 0.112 | 0.431 |
| Type C | | | | | | 2.480 | 0.050 | 0.358 |
| Type D | | | | | | 0.000 | 0.050 | 0.358 |

## 3.3. Finite element analysis results

### 3.3.1. Calculation of the fabric compressive stress of specimen types B, C and D at (-20)°C and 26°C

The fabric compressive stress at (-20)°C and 26°C of specimen types B, C and D is calculated numerically. The calculation is based on FEA of specimen types B, C and D FE models. The calculation procedure is based on the difference in a cured fabric ply residual compressive stress at (-20)°C and 26°C (Equation 2 and Equation 3). This compressive stress is assumed

to be predominantly caused by the adjacent matrix layer shrinkage. The more the fabric is compressed by the adjacent matrix layers, the more it can be later stretched during the static test.

The results are presented in Table 9. The fabric has more residual compressive stress at (-20)°C due to the higher matrix shrinkage compared to 26°C. Test data at both temperatures is available for specimen type B. The difference in the UTS between the two temperatures is 55 MPa (Table 17) compared to 34 MPa calculated by the FEA and the corresponding assumptions described in the previous paragraph.

$$N11_{fiber} = S11_{fiber} \cdot t_{fiber} \qquad \text{Equation 2}$$

$$dN11_{fiber} = N11_{fiber}^{26°C} - N11_{fiber}^{(-20)°C} \qquad \text{Equation 3}$$

**Table 9, Fiber compressive stress at (-20)°C and 26°C**

| Specimen | $N11_{fiber}^{26°C}$ | $N11_{fiber}^{(-20)°C}$ | $dN11_{fiber}$ |
|---|---|---|---|
| [-] | [N/mm] | [N/mm] | [N/mm] |
| Type B | -121 | -155 | 34 |
| Type C | -132 | -172 | 40 |
| Type D | 3 | 3 | 0 |

### 3.3.2. Analysis of the resin rich area stress cycle

The maximum in-plane principal stress (SP) is oriented longitudinally in the resin rich area of the bead and specimen types B and C (Figure 23 and Figure 24). In other words, SP orientation coincides with the longitudinal stress S11. Moreover, the predominant part of the cracks are perpendicular to the longitudinal axis of the bead and the specimens. This shows that the cracks are perpendicular to SP. Based on this finding flat composite specimen geometry is defined, because the bead corner radius is observed to show little influence on the SP-crack orientation relation.

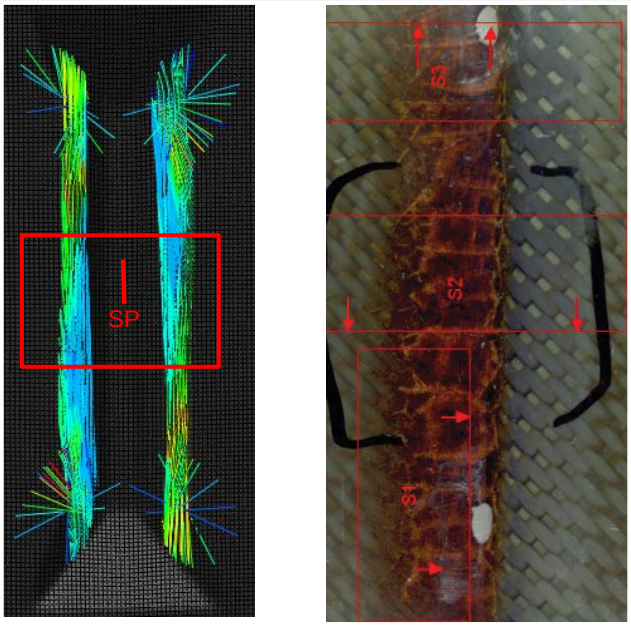


**Figure 23, Correlation of the SP orientation of the bead with the cracks in the resin rich area**

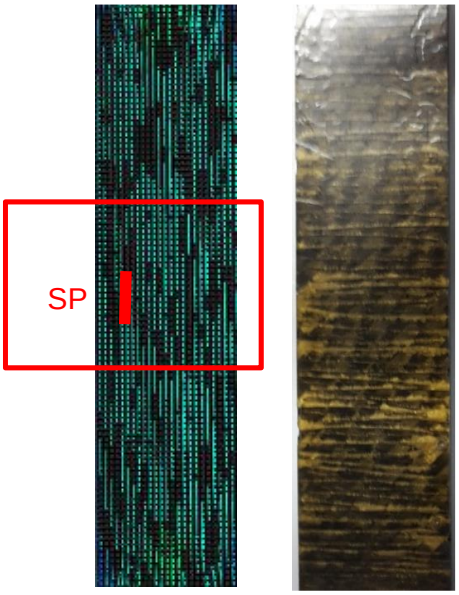


**Figure 24, Correlation of the SP orientation of specimen type B with the cracks in the resin rich area**

Two parameters are used to characterize the stresses that are presented in Figure 25 to Figure 30. The first parameter is the absolute through-the-thickness longitudinal stress S11. The second parameter is the S11 stress amplitude that is defined by Equation 4. Moreover, instead of stress of the whole specimen cross-sectional area, running load is used as a measure of the mechanical load (Equation 5).

$$2.S11_a = S11_{max} - S11_{min}$$ Equation 4

$$N = \frac{F}{w_{specimen}}$$ Equation 5

The bead stress cycle is created by the thermal cyclic load defined in section 3.2.2. The bead stresses in the resin rich area for the two limit temperatures of the thermal cycle are presented in Figure 25. The bead stress amplitude is presented in Figure 26. The bead thermal cycle loads the fibers and the matrix with opposite stresses. The matrix is loaded in tension and the fibers are loaded in compression. In other words, the stress cycle of the two composite constituents is opposite. The fiber stress at T=26°C is higher than the stress at T=(-20)°C, (Table 10).

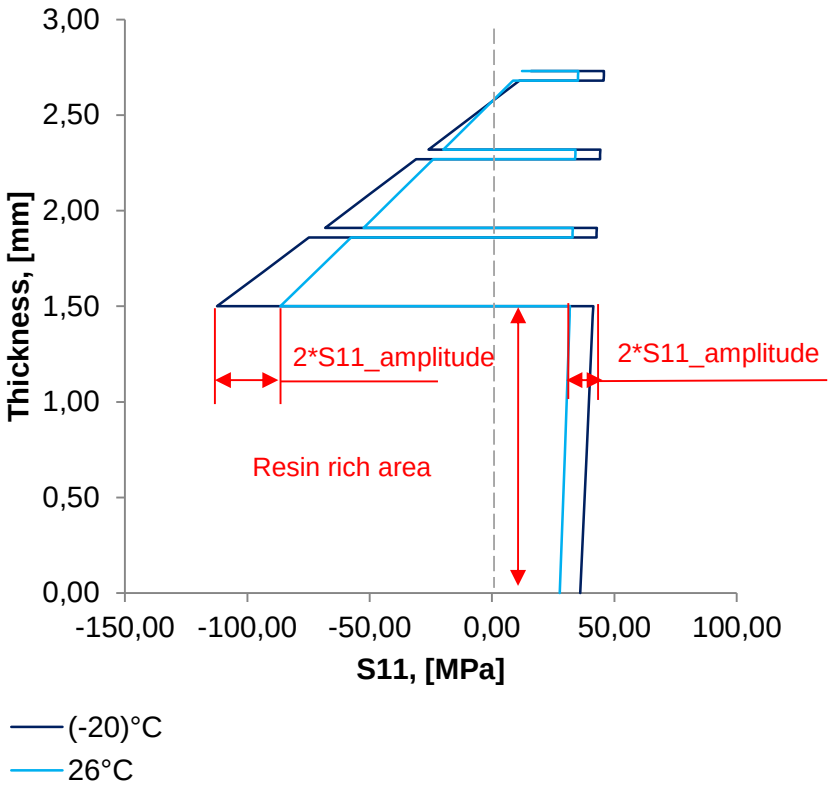


**Figure 25, Through-the-thickness stress of the bead**

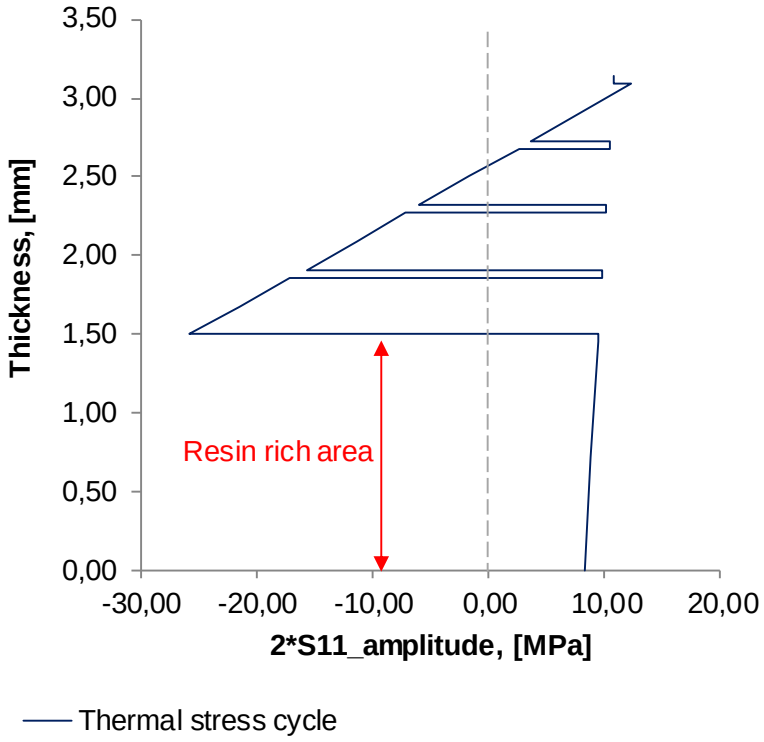


**Figure 26, Through-the-thickness stress amplitude of the bead**

Specimen type B stresses resulting from the mechanical load cycle at (-20)°C and 26°C are presented in Figure 27. The specimen stress amplitudes for both temperatures are presented in Figure 28. In the first place, the specimen mechanical load cycle makes the stress increase in both the fibers and the matrix. The mechanical stress cycle of both specimen types for both composite constituents is tensile. The fiber stress at minimum load is lower than the stress at maximum load (Table 10). In the second place, the matrix stress increases through-the thickness of the resin rich layer.

The stress trends of specimen type C are the same as those observed in specimen type B (Figure 27 and Figure 28). The stresses and the stress amplitudes of specimen type C are presented in Figure 29 and Figure 30. The fiber stress at minimum load is lower than the stress at maximum load (Table 10).

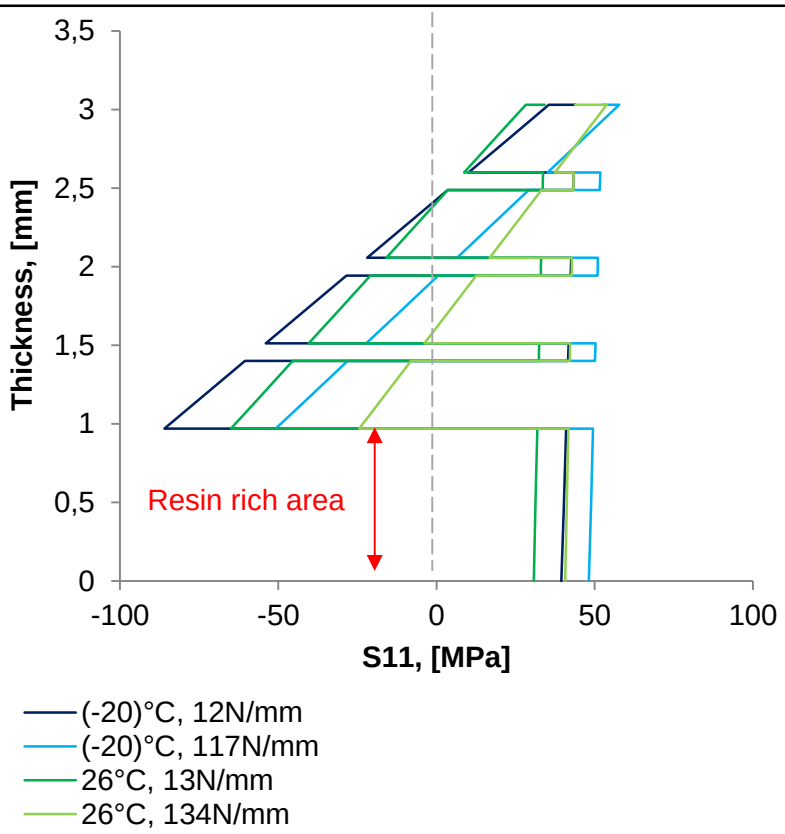


**Figure 27, Through-the-thickness stress of specimen type B**

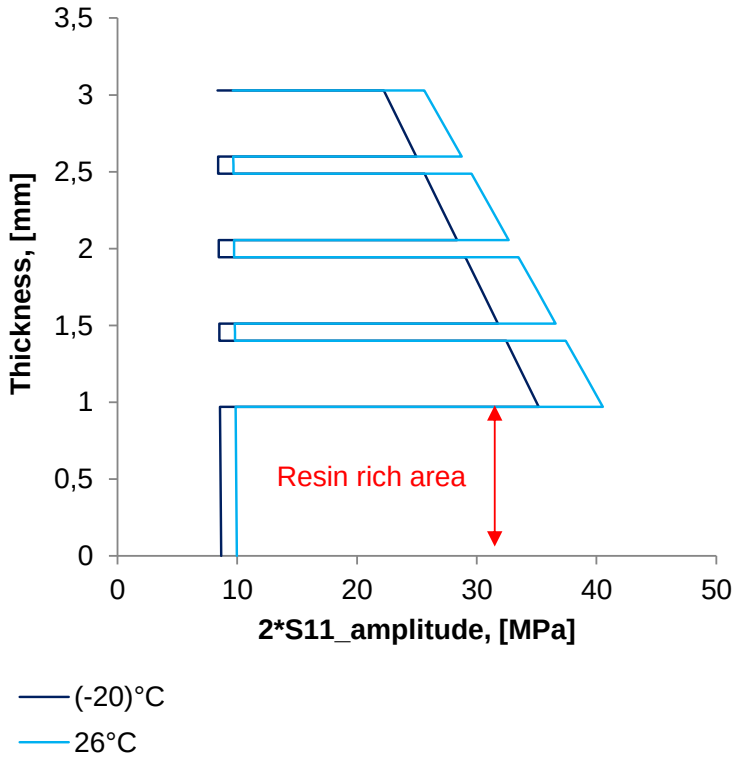


**Figure 28, Through-the-thickness stress amplitude of specimen type B**

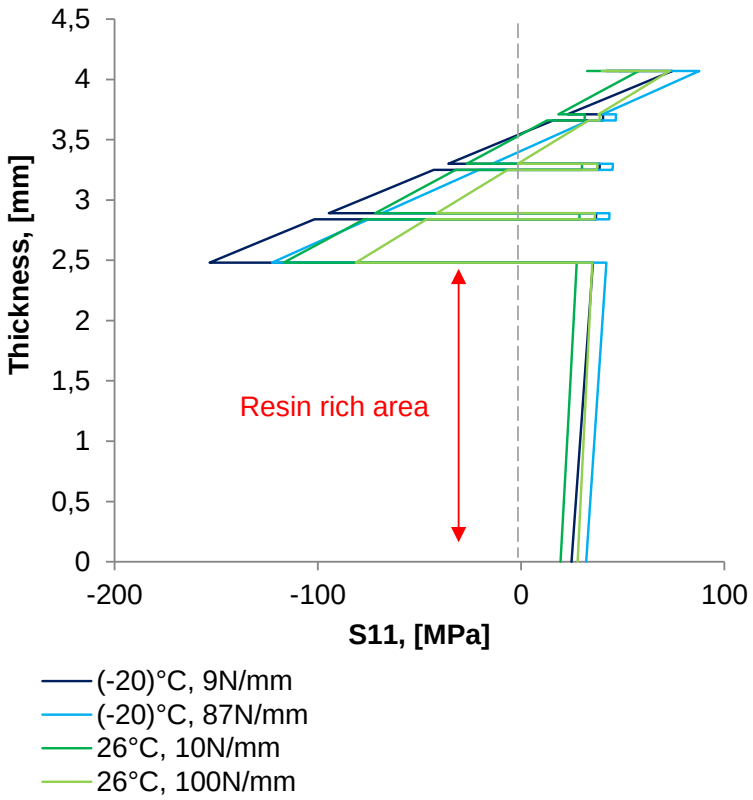


**Figure 29, Through-the-thickness stress of specimen type C**

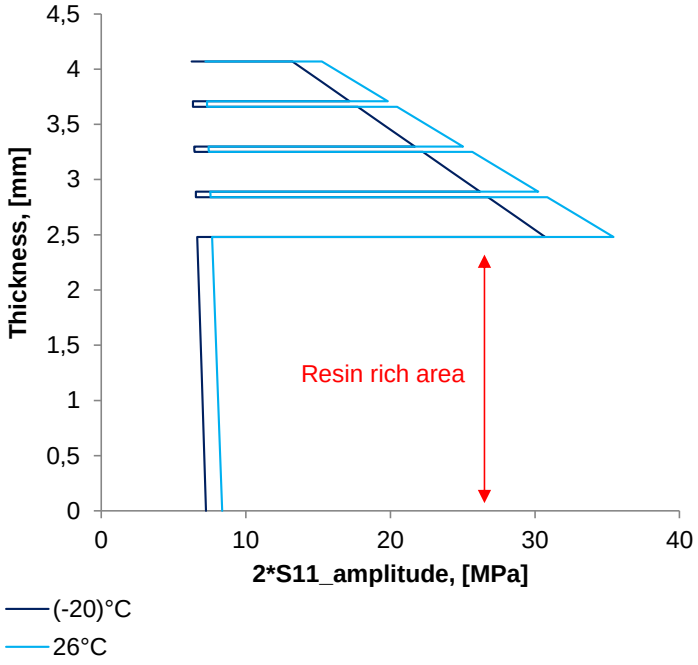


**Figure 30, Through-the-thickness stress amplitude of specimen type C**

**Table 10, Fiber stress cycle comparison at the resin rich layer interface**

| Specimen | T | Fiber $S11_{min\ load}$ | Fiber $S11_{max\ load}$ |
|---|---|---|---|
| [-] | [°C] | [MPa] | [MPa] |
| Bead | 26 and -20 | -86 | -112 |
| Type B | -20 | -86 | -51 |
| | 26 | -65 | -24 |
| Type C | -20 | -153 | -123 |
| | 26 | -117 | -83 |

In addition to the matrix stress amplitude, another investigated parameter is the interlaminar stress at the resin rich layer interface. The interlaminar stress is calculated by subtracting the fiber stress from the matrix stress (Equation 6). Similar to the matrix stress amplitude at the interface, the interlaminar stress amplitude is calculated by subtracting the minimum interlaminar stress from the maximum (Equation 7).

$$SIL = S11_{matrix} - S11_{fiber} \quad \text{Equation 6}$$

$$2.SIL_a = SIL_{max} - SIL_{min} \quad \text{Equation 7}$$

The resin rich layer stress analysis is mainly focused on the resin rich layer interface. Therefore, an overview of the stresses at the resin rich layer interface is presented in Table 11. Moreover, the presented stresses are used to calculate the fatigue parameters at the interface in Table 12 and Table 13.

**Table 11, Stresses at the resin rich layer interface**

| Specimen | T | F1 | N11 | $S11_{matrix}$ | $S11_{fiber}$ | SIL |
|---|---|---|---|---|---|---|
| [-] | [°C] | [N] | [N/mm] | [MPa] | [MPa] | [MPa] |
| Bead | -20 | N/A | N/A | 41 | -112 | 153 |
| | 26 | N/A | N/A | 31 | -86 | 117 |
| Type B | -20 | 300 | 12 | 41 | -86 | 127 |
| | -20 | 2925 | 117 | 50 | -51 | 101 |
| | 26 | 325 | 13 | 32 | -65 | 97 |
| | 26 | 3350 | 134 | 42 | -24 | 66 |
| Type C | -20 | 225 | 9 | 35 | -153 | 188 |
| | -20 | 2175 | 87 | 42 | -123 | 165 |
| | 26 | 250 | 10 | 27 | -117 | 144 |
| | 26 | 2500 | 100 | 35 | -81 | 116 |

The fatigue parameters of the matrix stress cycle in the bead and specimen types B and C at the resin rich area interface are presented in Table 12. The R-ratio in all cases is in a range of 0.76-0.73. Moreover, the stress amplitude ($S11_a$) is in the range of 4-5 MPa. The maximum stress has higher variation. It is in the range of 35-50 MPa.

**Table 12, Fatigue parameters of the matrix stress cycle at the resin rich layer interface**

| Specimen | T | R | $S11_a$ | $S11_{min}$ | $S11_{max}$ |
|---|---|---|---|---|---|
| [-] | [°C] | [-] | [MPa] | [MPa] | [MPa] |
| Bead | 26 and -20 | 0.78 | 5 | 32 | 41 |
| Type B | 26 | 0.76 | 5 | 32 | 42 |
| | -20 | 0.82 | 5 | 41 | 50 |
| Type C | 26 | 0.77 | 4 | 27 | 35 |
| | -20 | 0.83 | 4 | 34 | 41 |

The fatigue parameters of the interlaminar stress cycle in the bead and specimen types B and C at the resin rich area interface are presented in Table 13. The R-ratio in all cases remains is in a range of 0.68-0.88. Moreover, the interlaminar stress amplitude ($SIL_a$) is in the range of 12-18 MPa. The maximum stress is in the range of 97-188 MPa.

**Table 13, Fatigue parameters of the interlaminar stress cycle at the resin rich layer interface**

| Specimen | T | R | $SIL_a$ | $SIL_{min}$ | $SIL_{max}$ |
|---|---|---|---|---|---|
| [-] | [°C] | [-] | [MPa] | [MPa] | [MPa] |
| Bead | 26 and -20 | 0.76 | 18 | 117 | 153 |
| Type B | 26 | 0.68 | 16 | 66 | 97 |
| | -20 | 0.80 | 13 | 101 | 127 |
| Type C | 26 | 0.81 | 14 | 116 | 144 |
| | -20 | 0.88 | 12 | 165 | 188 |

**Validation of the matrix residual stress results**

The residual stresses in a UD laminate on micro-level are calculated by the use of a hexagonal unit-cell FE model, [24]. The FE model has fiber volume fraction of 60% and is loaded by a thermal load dT=(-155)°C. The FE model boundary conditions only fix it in space, i.e. it is representative for a free expandable laminate. The material is modeled by using RTM 6 temperature dependent properties (section 2.4.1). Both linear and non-linear matrix material models are used.

The maximum residual stress obtained by the linear FEA is 36 MPa. The non-linear FEA provides a lower residual stress of 29 MPa. The FEA results are verified by a photo-elastic measurement, [28]. The measured residual stresses using the photo-elastic method reach 28 MPa.

## 3.4. Chapter outcomes

The main outcome of this chapter is that the bead thermal stresses cannot be completely matched by applying mechanical load to a specimen. Therefore, the investigated parameters are further narrowed down to the longitudinal matrix stress and the interlaminar stress at the resin rich layer interface with the first fabric ply. Moreover, as the load is cyclic, the amplitude and the R-ratio of the investigated stresses are also calculated and analyzed.

Applying mechanical loads to the specimens that are experimentally determined in chapter 5 gives similar results to the bead matrix stress cycle at the interface. The interlaminar stress cycle at the interface differs to a higher extent than compared to the matrix stress cycle.

The experimental work is influenced by the FEA in a few ways. Specimen type C and D UTS at (-20)°C is calculated in chapter 5 from the difference of the residual compressive fiber stress calculated between 26°C and (-20)°C in this chapter to save time. Specimen type A stress cycle applied during testing is the same as the cycle of the matrix at the interface in the bead (calculated in this chapter). One of the fatigue load cases applied to specimen type B is matching the interlaminar stress cycle at the interface of the bead (calculated in this chapter).

# 4. Specimen description

## 4.1. Chapter introduction

This chapter describes the manufacturing of the specimens for this project, including geometry and assessment of the manufacturing quality. The goal of this chapter is to fabricate a pure polymer dog-bone specimen and flat rectangular composite specimens with a resin rich layer that are representative of the bead.

One type of pure polymer dog-bone specimen and three types of composite specimens are manufactured. The polymer dog-bone specimen type A goal is to match the matrix stress at the bead resin rich layer interface with the first fabric ply in a mechanical test.

The goal of the first composite specimen type B is to manufacture a specimen in a single step for testing similar to the real bead. The goal of the second composite specimen type C is to obtain a specimen with better compaction that is more representative of the bead, because specimen B is poorly compacted. To achieve that, specimen C is fabricated in two steps. Specimen types B and C are used to investigate the damage development and the loads and the stresses that produce them. Specimen type D is a reference specimen without any resin rich layer. It is used to monitor the damage development in the absence of a resin rich layer.

Pure polymer specimen A is made by injection molding of the epoxy resin in an aluminum mold. Composite specimen B is made by vacuum infusion and by the use of special spacers to make the resin rich layer in one manufacturing step. Composite specimen C is made by conventional vacuum infusion of a pure laminate and subsequent co-bonding of the resin rich layer onto an activated surface by UV/ozone treatment. Composite specimen D is made by conventional vacuum infusion of a pure laminate.

## 4.2. RTM 6 curing cycle

The RTM 6 curing cycle used for the manufacturing of the composite specimens is the same. The curing cycle is presented in Figure 31. Resin infusion is performed at 120°C and 50 mbar of absolute pressure for approximately 30 minutes. It is followed by a ramp-up stage, where the temperature is increased from infusion to curing temperature with 2°C/min heat-up rate. The laminate is cured for 2 hours at 180°C. Finally, the laminate is cooled with 3°C/min cool-down rate.

The thermal profile of the curing cycle of specimen type A (i.e. the pure polymer specimen) is the same as in Figure 31. However, there is no applied vacuum. In other words, it cures at ambient pressure.

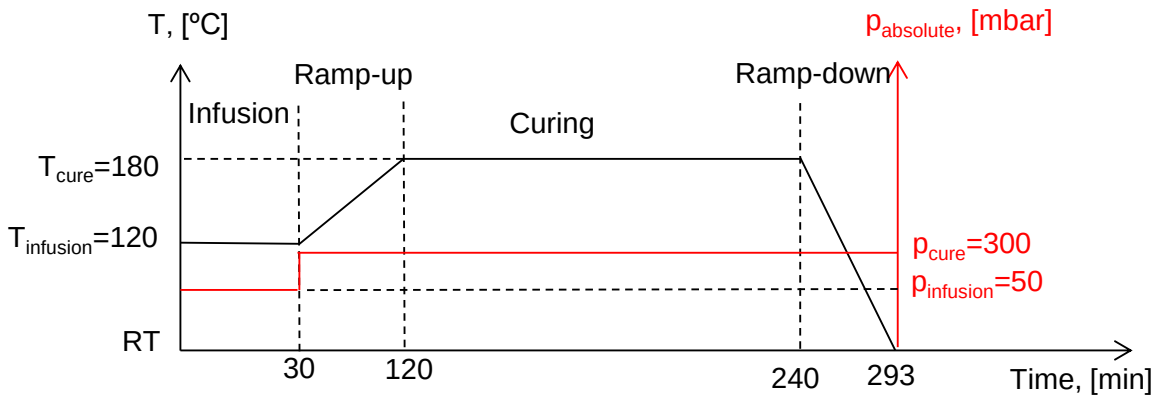


**Figure 31, RTM 6 curing cycle, [23]**

### 4.3. Type A

One type of pure polymer specimen made from RTM 6 epoxy is manufactured. It is manufactured in a dog-bone shape. The dog-bone shape is typical for testing the tensile properties of plastics, [35, 36]. The geometry of the specimen type A is presented in Figure 32. The presented geometry is completely in accordance with the ASTM standard for testing tensile properties of plastics, [36].

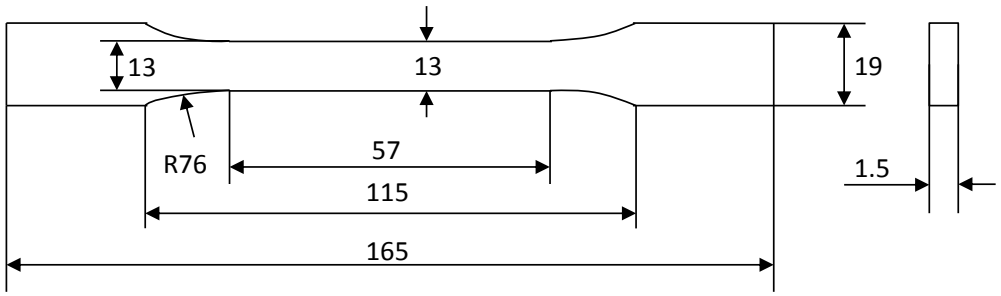


**Figure 32, Geometry of specimen type A**

Specimen type A is produced by injection molding in one step. The mold is machined from thick aluminum plate. A photo of the mold is presented in Figure 33. It consists of two parts – a mold and a cover. The dog-bone shaped cavity for the specimen is machined in the mold. The two flushing surfaces of the mold and the cover are polished to ensure perfect matching of both surfaces, which prevents resin from escaping. The two parts of the mold assembly are assembled and fastened with bolts.

The manufacturing process starts with applying Marbocote release agent on the mold and closing it. The resin and the mold are preheated at infusion temperature to decrease the resin viscosity and make it suitable for injection. Then the resin is injected through the inlet by a syringe in an inclined mold. The resin is injected from bottom to top to prevent air entrapment. Subsequently, the mold is put back in a horizontal position, inserted in an oven and the resin

is cured at curing temperature for 2 hours. The manufacturing process provides net-shaped dog-bone RTM 6 specimen.

Mold cover

Mold

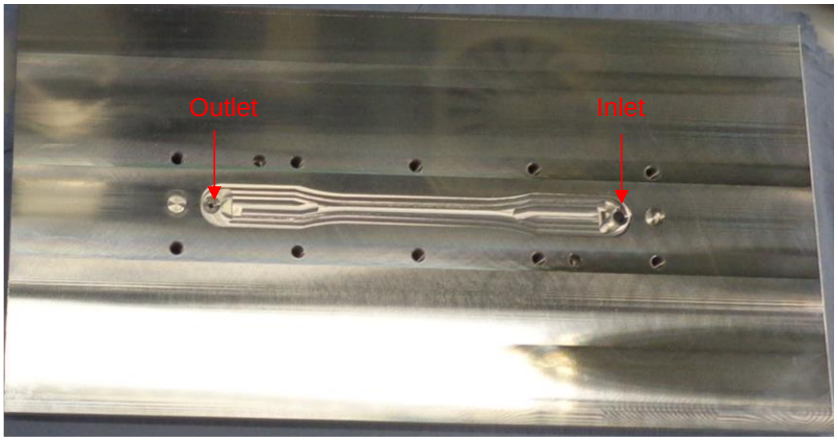


**Figure 33, Mold of specimen type A**

### 4.4. Type B

Specimen type B is a composite specimen with a resin rich layer produced in one step. The in-plane geometry of the specimen is presented in Figure 34. The geometry is typical for testing the tensile properties of composites, [9, 21, 22].

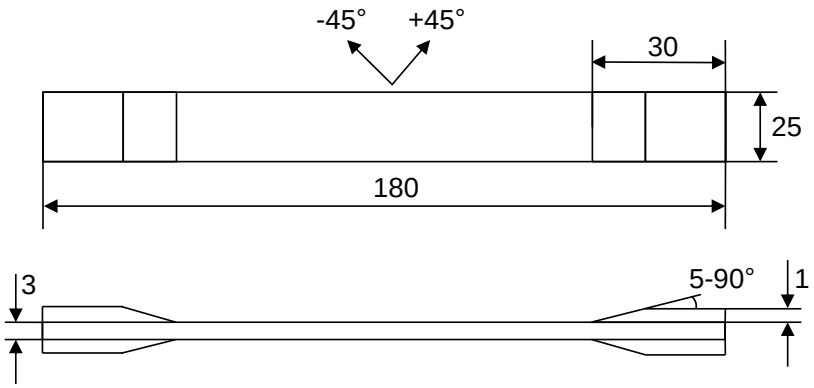


**Figure 34, Geometry of specimen type B**

In order to prevent grip slippage during testing, aluminum tabs are attached to the specimen. They are cut out of aluminum sheet metal at a guillotine by shearing. In addition, to avoid stress concentrations near the tab edges a bevel angle is created in the tabs by grinding. The tabs are attached to the specimen by adhesive bonding. The used adhesive is 3M Scotch-Weld EC-9323 B/A aerospace grade structural two-component epoxy adhesive. In order to control the bond line thickness, 6% of glass beads with diameter of 100-300 microns are added to the adhesive.

The layup of the specimen is illustrated in Figure 35. It consists of four fabric plies rotated at 45° with respect to the laminate longitudinal axis. In between every two fabric plies there are interface resin layers. Moreover, there is a thick one-sided resin rich layer, which makes the layup asymmetrical. This layup asymmetry creates residual deformation in the specimen after manufacturing. In other words, the specimen is bent around a sphere, because the residual matrix thermal stress is biaxial. In addition, the resin rich layer substantially reduces the fiber volume fraction for obvious reasons.

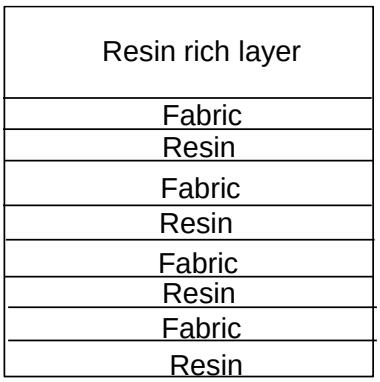


**Figure 35, Layup of specimen type B**

The specimens type B are produced by the use of a vacuum infusion process in one step. A schematic of the complete production set-up is illustrated in Figure 36. A photo of it is presented in Figure 37. An electrical hot plate is used to preheat the resin to infusion temperature. An electrically heated blanket is used to preheat the vacuum bag layup to infusion temperature. The temperature is controlled by a thermocouple. A flow control valve is used to control the resin flow speed during the infusion process. Finally, the infused laminate is cured in an electrical oven. The specimens are cut from the cured laminate with a diamond disk cutter.

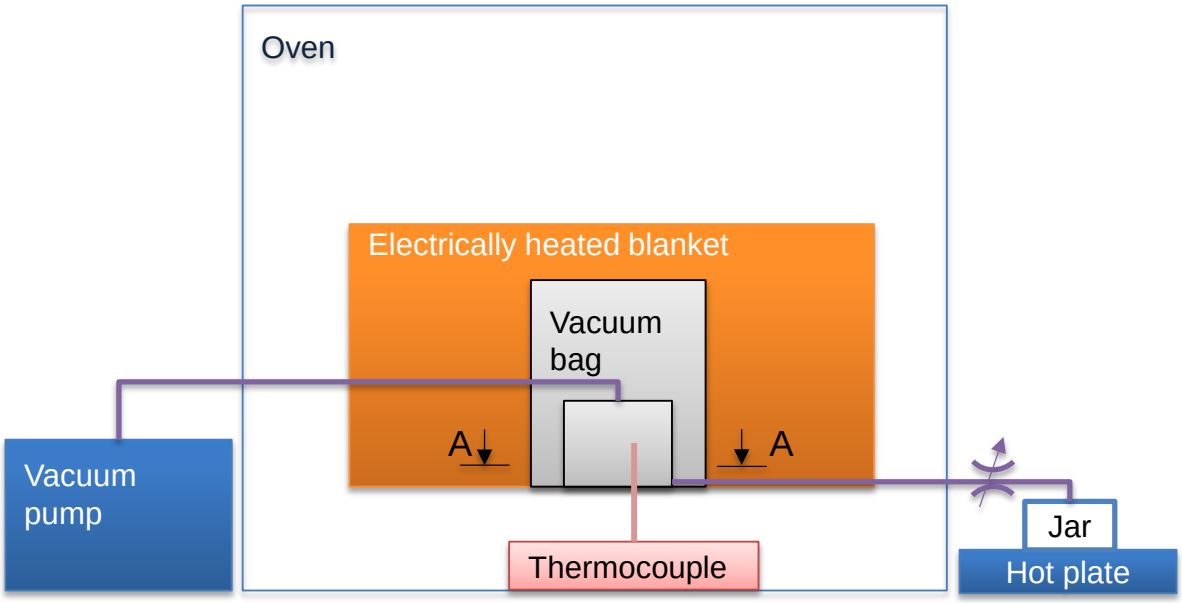


**Figure 36, Schematic of the vacuum infusion set-up of specimen type B**

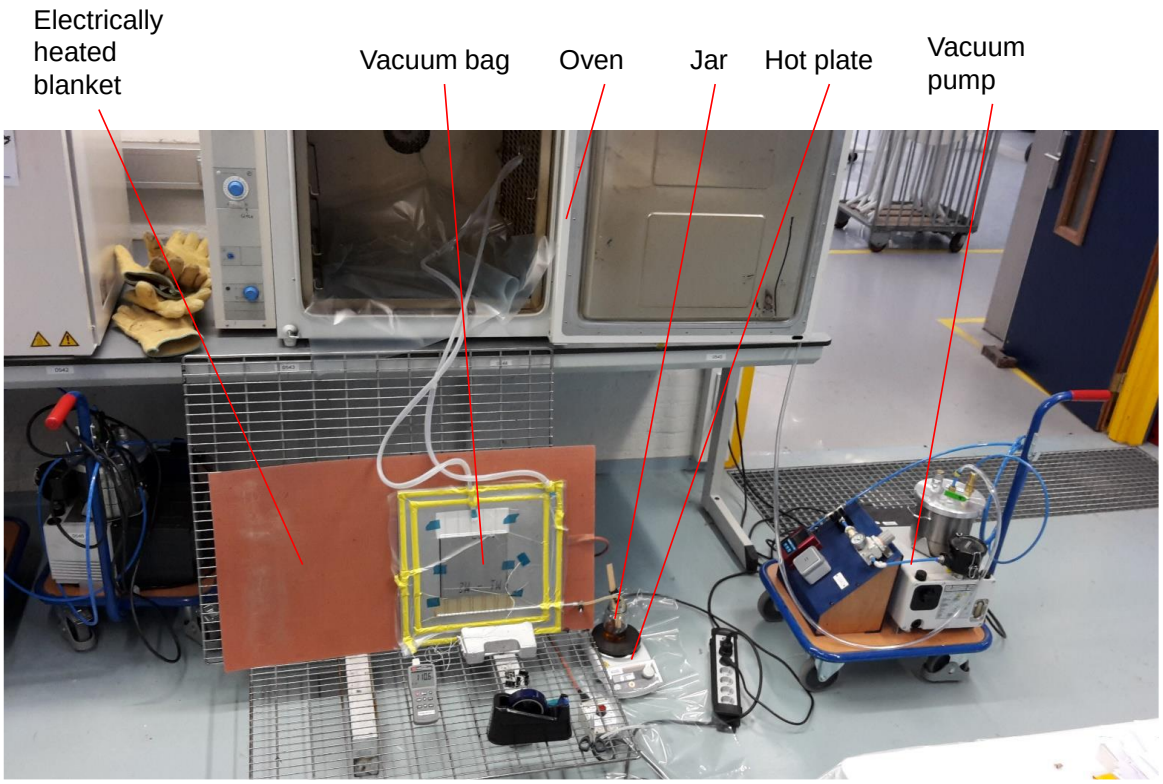


**Figure 37, Photo of the vacuum infusion set-up of specimen type B**

To manufacture the specimens type B, a special vacuum bag layup is used (Figure 38). On both sides of the laminate relatively thick (3 mm) aluminum plates are placed to hold the laminate in place during manufacturing and to ensure good surface quality. Both plates are

covered with Marbocote release agent. The fabric is laid down on the bottom plate. Between the top plate and the fabric 2 mm steel wire spacers are inserted. Their purpose is to control the cavity (i.e. the future resin rich layer) thickness. The smooth shape of the spacers ensures that no cracks are initiated in the resin rich layer due to initial flows at the edges of the resin rich layer during manufacturing. Finally, the vacuum bag is sealed with two high-temperature tacky tape perimeters to avoid leakages due the tacky tape softening at the high curing temperature.

The manufacturing process is relatively complex. First, the vacuum bag layup is laid down and checked for leakage under vacuum (i.e. absolute pressure is 10 mbar) at infusion temperature. Then the resin is preheated at infusion temperature and degassed for 30 minutes under the same vacuum. Subsequently, the preheated resin is infused in the vacuum bag layup, which is also preheated at infusion temperature. The resin flow is controlled to ensure simultaneous infusion of the cavity and the fabric. At last, the laminate is cured.

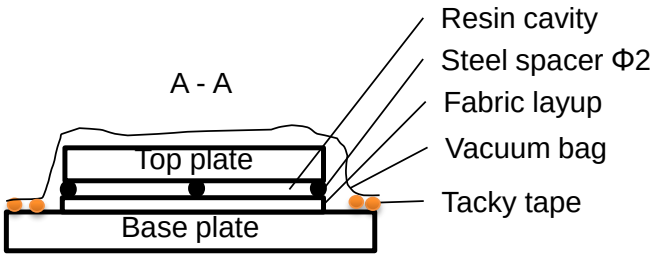


**Figure 38, Vacuum bag layup of specimen type B**

### 4.5. Type C

Specimen type C is a composite specimen with resin rich layer produced in two steps. It has the same geometry and layup as specimen type B (section 4.4). Moreover, the tabs are manufactured and bonded using the same procedure as in specimen type B.

In the first production step of the specimen type C, a pure laminate is vacuum infused and cured (i.e. the laminate is processed in one curing cycle). The pure base laminate manufacturing process is similar to the one used for the specimen type B (section 4.4). The only difference is that in the vacuum bag layup no spacers are used, because there is no resin rich layer during this first manufacturing step (Figure 38). In the second production step, the resin rich layer is co-bonded to the cured laminate (i.e. the cured laminate is processed in a second curing cycle). The resin is casted in a mold on the top of the cured laminate.

A photo of the co-bonding set-up is shown in Figure 39. The mold for the process is made from aluminum sheet metal by bending and attaching to the base together with the laminate via the clamps. The base of the set-up is cut from thick solid aluminum plate. The clamps are cut on a guillotine via shearing of aluminum sheet metal. They do not only fix the set-up, but also prevent the specimen from premature thermal bending during the manufacturing. High temperature tacky tape is used to seal the mold. Steel wire spacers with 1.5 mm diameter are used to control the resin rich layer visually.

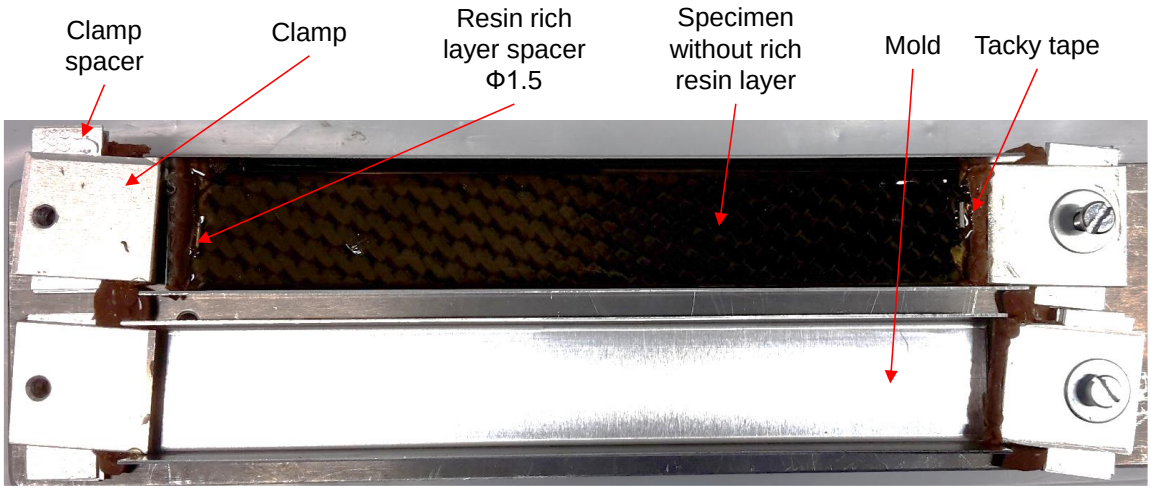


**Figure 39, Co-bonding set-up of specimen type C**

Two surface parameters play substantial roles in the co-bonding process. First, is the surface roughness, which facilitates the micro-mechanical interlocking at the bond line. Second, it is the surface activation, which improves the chemical bonding at the bond line.

The co-bonding process starts with preparing the surface (Figure 40). It is cleaned, roughened and treated with UV/ozone surface treatment for 5 minutes, which activates the surface for bonding. Then the specimen is fixed in the mold. Subsequently, the mold is sealed. Finally, the resin is cast on the top of the activated laminate surface and the product is cured in a second curing cycle.

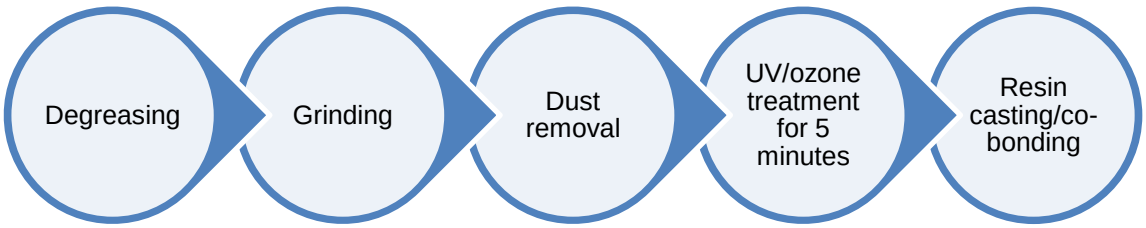


**Figure 40, Co-bonding process of specimen type C**

The surface activation is characterized by the surface wetting. A measure of the surface wetting is the surface contact angle. The effect of the UV/ozone treatment on the wetting is assessed by measuring the surface contact angle via a water drop shape analysis (Figure 41). A water droplet with precisely controlled volume is put on the surface. Using a camera and

image post-processing software the contact angle at the droplet intersection with the surface is calculated. KSV NIMA CAM200 contact angle measurement equipment is used.

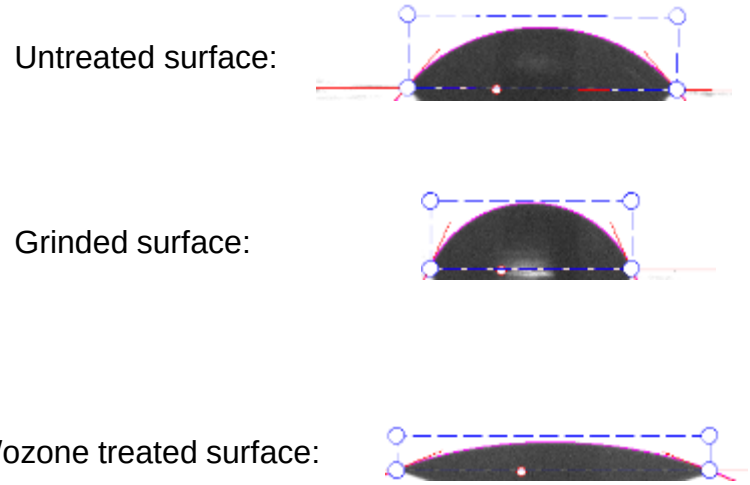


**Figure 41, Water droplet shape for the contact angle measurement during the stages of the co-bonding process**

The contact angle reduction after the UV/ozone treatment (Table 14). The resulted contact angle reduction is the highest angle that is able to be obtained. Moreover, it is observed that the contact angle remains low after the treatment for at least 20 minutes, which eliminates possible wetting reduction during the set-up handling (i.e. preparation) for casting.

**Table 14, Contact angle measurement during the stages of the co-bonding process**

| Surface treatment | Contact angle |
|---|---|
| [-] | [°] |
| Untreated surface | 50 |
| Grinded surface | 65 |
| UV/ozone treated surface for 5 minutes | 22 |

### 4.6. Type D

Specimen type D is a composite specimen without a resin rich layer produced in one step. In other words, it is the base laminate produced in the first manufacturing step of specimen type C (section 4.5) It has the same geometry and layup as specimen type B (section 4.4). Moreover, the tabs are manufactured and bonded using the same procedure as for specimen type B.

## 4.7. Evaluation of the manufacturing quality

A measure of the laminate manufacturing quality is its compaction. To investigate the laminate compaction, the laminate layer thicknesses are measured. The average thickness data is presented in Table 15. The average resin rich layer thickness of the specimen type B is smaller than the one of the specimen type C.

The base laminate of specimen types C and D is the same. The only difference between them is the presence of a resin rich layer in type C. Therefore, the fabric and the interface resin layer thicknesses for specimen types C and D is the same.

**Table 15, Average layer thicknesses**

| Specimen | Resin rich layer thickness | Interface resin layer thickness | Fabric ply thickness |
|---|---|---|---|
| [-] | [mm] | [mm] | [mm] |
| Bead | 1.500 | 0.050 | 0.360 |
| Type B | 0.970 | 0.112 | 0.431 |
| Type C | 2.480 | 0.050 | 0.358 |
| Type D | N/A | 0.050 | 0.358 |
| Datasheet, [23] | N/A | N/A | 0.360 |

An overview of the layer thicknesses of the specimen type B is presented in Figure 42. There are 0.112 mm thick interlaminar resin rich areas on average, which become distinguishable interface resin layers. Moreover, the fabric ply is poorly and non-uniformly compacted (0.431 mm compared to 0.360 mm in the datasheet). This leads to thinner and non-uniform resin rich layers and overall poor laminate compaction. The complete set of thickness measurements is presented in Appendix 1.

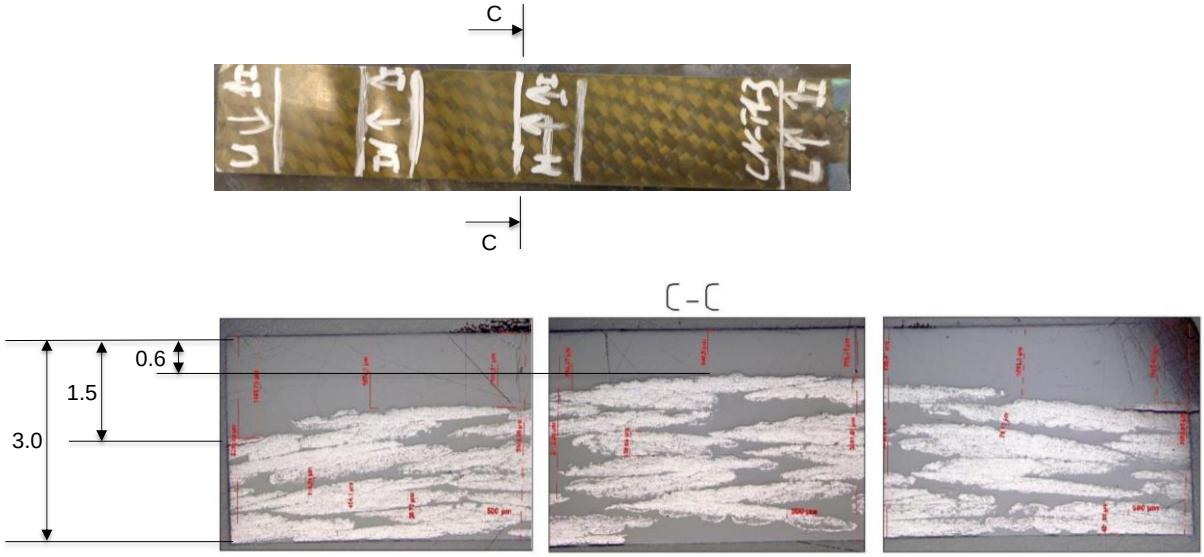


**Figure 42, Overview of the layer thicknesses of specimen type B**

An overview of the layer thicknesses of the base laminate of the specimen types C and D is presented in Figure 43. The fabric ply has approximately 0.360 mm uniform thickness, which is the same as seen in the datasheet, [23]. Moreover, no large interply resin rich areas are observed. Only tiny resin pockets due to the fabric weave are observed.

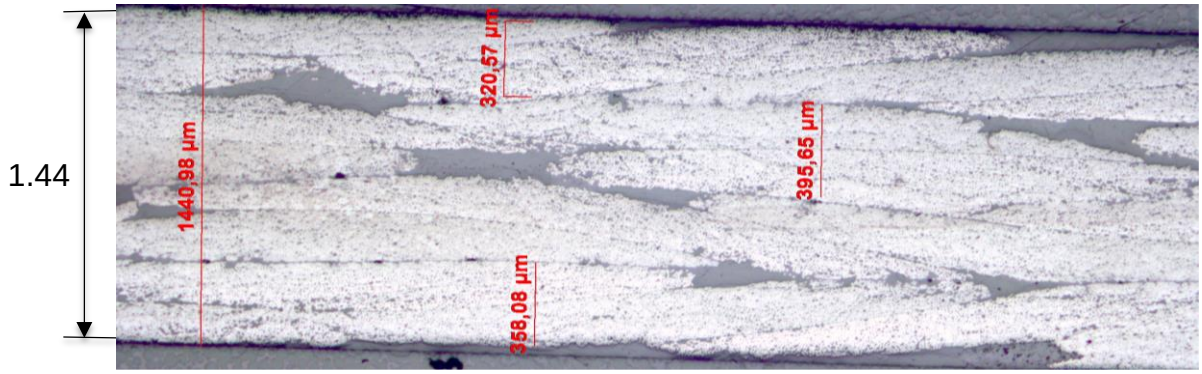


**Figure 43, Overview of the layer thicknesses of specimen type C and D base laminate**

## 4.8. Chapter outcomes

Specimen type B laminate is not completely representative for the bead laminate, because of its poor compaction. Moreover, specimen type C laminate is also not completely representative for the laminate, because of two reasons – the interface of the resin rich layer resulting from the co-bonding process and the second curing cycle the base laminate undergoes. At last, the composite coupons are flat and no radii as in the bead are fabricated.

There are a few implications for the test resulting from the aforementioned limitations. First, specimen type B might exhibit more matrix damage due to the bigger amount of resin in the laminate (poor compaction). Second, specimen type C laminate might be more damage resistant due to its second curing cycle and interface created in the second production step. Third, the simplification of the coupons by excluding the bead radius is proven not to influence the stresses much, because the maximum principal in-plane stress in the resin rich area is oriented longitudinally in the bead (chapter 3).

# 5. Tests

## 5.1. Chapter introduction

This chapter describes the tests performed for this project. First, the test matrix is described. Second, the test results are presented.

Mechanical fatigue tests were carried out in order to observe if representative bead matrix cracking damage could be reproduced in the rectangular specimens under mechanical loading that matched the matrix or interlaminar shear stresses at the interface in the bead. The matrix stress at the interface is matched by mechanically testing pure polymer specimen type A. The interlaminar stress is matched by mechanically testing composite specimen type B.

Both tests exhibit no damage and therefore, the test philosophy is shifted from being stress replication focused to damage focused. In other words, the load is changed until damage similar to the bead damage is observed in the composite specimens. Only then the stresses producing this damage are compared and analyzed.

Composite specimen types B, C and D are tested mechanically in fatigue according to the damage focused philosophy. Two main features are obtained from the tests. First, is the damage development. Second, is the load levels to obtain this damage development. The stresses resulting from the experimentally selected load levels are calculated and analyzed in chapter 3.

The results from specimen types C and D are to be interpreted together. The reason is that specimen type D is the base laminate of specimen type C without the co-bonded resin rich layer. Therefore, specimen type D serves as a reference configuration of specimen C.

## 5.2. Test matrix

The test matrix is presented in Table 16. In total 35 specimens are tested statically and in fatigue at two ambient temperatures. The tests denoted as performed at RT are performed in a lab environment. The test frequency in all fatigue tests is 5 Hz.

Each test has defined measurements that are performed during this test. The required test measurements are numbered in Table 16 and formulated as follows:

1. Obtain specimen UTS;
2. Match exactly the matrix stress cycle at the bead resin rich layer interface;
3. Match exactly the interlaminar stress amplitude at the bead resin rich layer interface;
4. Select cyclic load level suitable for studying the fatigue damage;
5. Fractography of specimens with a resin rich layer;
6. Calculate stiffness reduction of specimens with a resin rich layer due to damage accumulation;
7. Fractography of well compacted specimen without a resin rich layer to be used as a reference damage state.

All specimen types are tested statically (measurement 1). The result from the static test is the specimen temperature-dependent UTS. The only composite specimen type that is tested statically at (-20)°C and 26°C is type B. Specimen types C and D are tested statically only at RT. The UTS of specimen types C and D at (-20)°C is calculated from the RT data as it is described in section 3.3.1 and section 5.3.1.

All specimen types are tested in fatigue. Specimen type A is tested under a load that provides the same matrix stress cycle as at the bead resin rich layer interface (Table 11), (measurement 2). Specimen type B is tested under a load that provides the same interlaminar stress amplitude as at the bead resin rich layer interface (Table 13), (measurement 3). The absolute interlaminar stress values are not matched (Table 11). However, no damage is observed in these tests.

Therefore, the fatigue test philosophy is shifted from being stress focused to damage focused. First, the cyclic load levels to obtain desired damage levels are selected for specimen types B and C (measurement 4). This is the reason for the high variation in the applied loads shown in the first fatigue tests of each specimen-temperature combination in the test matrix in Table 16. Second, specimens B and C are tested at the selected load levels at different number of cycles to investigate the fatigue damage behavior through fractography (measurement 5). Third, the stiffness reduction due to damage accumulation during the fatigue test is calculated from the fatigue test load-displacement data (measurement 6).

The purpose of specimen type D is to have a reference fatigue damage state of a specimen with good quality without any resin rich areas (measurement 7). It is tested at the two temperatures by gradually increasing the load levels to ensure that fatigue damage does occur and the load level is not too low.

**Table 16, Test matrix (forces applied to a specimen with perfect dimensions are presented)**

| Specimen | T | Number of specimens | R | $F_{max}$ | Cycles | Test type | Measurement |
|---|---|---|---|---|---|---|---|
| [-] | [°C] | [-] | [-] | [N] | [-] | [-] | [-] |
| Type A | RT | 5 | N/A | | | Static | 1 |
| Type A | -20 | 1 | 0.78 | 800 | 0-170k | Fatigue | 2 |
| Type B | -20 | 5 | N/A | | | Static | 1 |
| Type B | RT | 5 | N/A | | | Static | 1 |
| Type B | -20 | 1 | 0.1 | 1 450 | 0-130k | Fatigue | 3 |
| Type B | -20 | 1 | 0.1 | 4 875 | 0-500 | Fatigue | 4 |
| Type B | -20 | 1 | 0.1 | 1 950 | 0-600k | Fatigue | 4 |
| | | | | 2 925 | 600k-780k | | 4, 5, 6 |
| Type B | RT | 1 | 0.1 | 5 850 | 0-8k | Fatigue | 4 |
| Type B | RT | 1 | 0.1 | 3 350 | 0-150k | Fatigue | 4, 6 |
| Type B | RT | 1 | 0.1 | 3 350 | 0-15k | Fatigue | 5 |
| Type B | RT | 1 | 0.1 | 3 350 | 0-60k | Fatigue | 5 |
| Type B | RT | 1 | 0.1 | 3 350 | 0-140k | Fatigue | 5 |
| Type C | RT | 2 | N/A | | | Static | 1 |
| Type C | -20 | 1 | 0.1 | 2 175 | 0-100k | Fatigue | 4, 5, 6 |
| Type C | RT | 1 | 0.1 | 1 875 | 0-20k | Fatigue | 4 |
| | | | | 2 500 | 20k-120k | | 4, 5, 6 |
| Type D | RT | 5 | N/A | | | Static | 1 |
| Type D | -20 | 1 | 0.1 | 2 125 | 0-20k | Fatigue | 4 |
| | | | | 2 850 | 20k-40k | | 4 |
| | | | | 3 550 | 40k-59k | | 4, 7 |
| Type D | RT | 1 | 0.1 | 2 125 | 0-20k | Fatigue | 4 |
| | | | | 2 850 | 20k-40k | | 4 |
| | | | | 3 550 | 40k-42k | | 4, 7 |

The cyclic load level selection procedure flow chart is illustrated in Figure 44. Cyclic load level means the maximum running load of the fatigue cycle. It is expressed as percentage of the specimen UTS (i.e. %UTS). The selection criterion for choosing the desired load level is obtaining the desired damage level. The load level is adjusted (i.e. increased or decreased) until the desired damage mode is achieved.

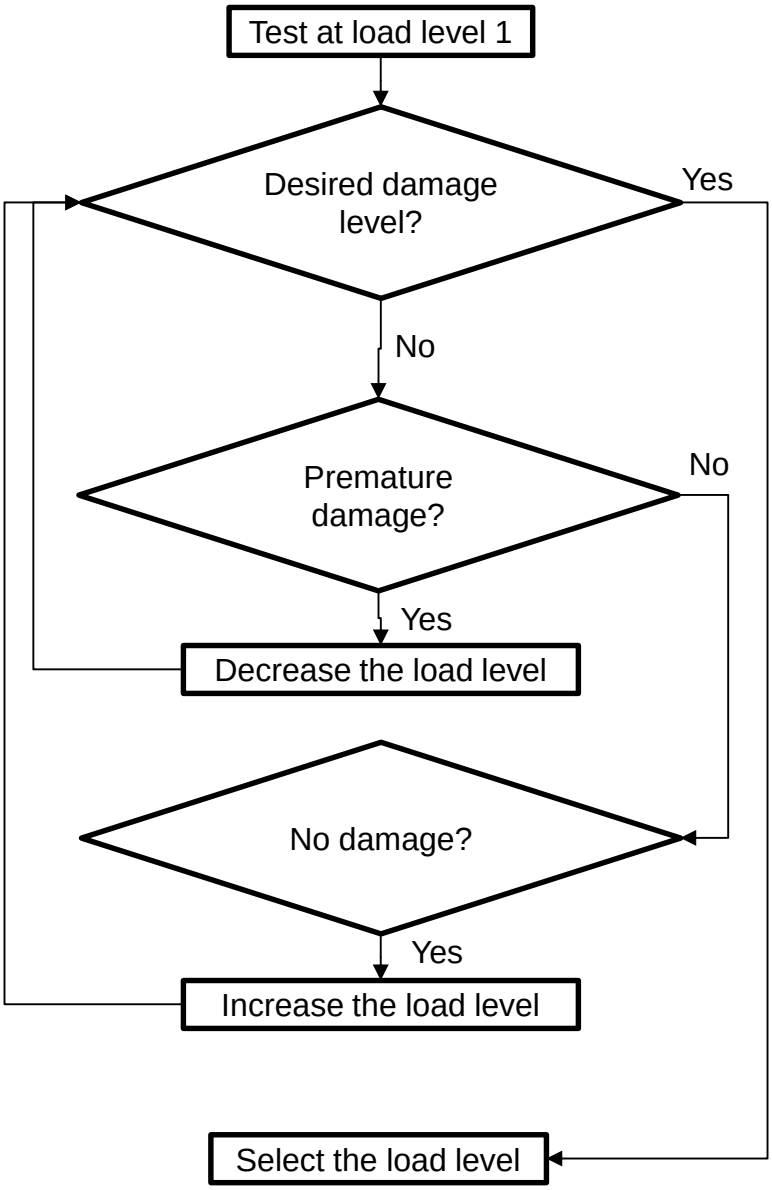


**Figure 44, Load level selection procedure**

The specimen stiffness is evaluated from the fatigue test load-displacement data by dividing the force by the displacement at the point of maximum load (Equation 8). This is not the real stiffness, but only a measure of it. It is interesting to calculate the stiffness reduction as a percentage. The stiffness reduction is calculated with respect to the stiffness of an intact specimen.

$$Measure\ of\ stiffness = \frac{Force}{Displacement}$$ Equation 8

Two static material testing machines are used in the static tests. Zwick 1455 20 kN machine with mechanical self-aligning grips is used for the RT tests. Zwick Z250 250 kN machine with standard mechanical grips and installed climate chamber cooled with liquid nitrogen is used for the tests at (-20)°C.

Two fatigue testing machines are used in the fatigue tests. The first machine is MTS 831 10 kN hydraulic fatigue testing machine with mechanical grips and installed additionally Thermotron climate chamber cooled by liquid nitrogen. The second machine is DynaMess 20 kN pneumatic fatigue testing machine with mechanical grips. The displacement is measured by the grip displacement gage embedded in the test machines. Moreover, in some tests a camera synchronized with the test machine is used to shoot a time-lapse video of the resin rich layer cracking.

The fractography is performed through microscopy. Leica DM LM optical microscope is used. The fractographic images are captured by Zeiss AxioCam ICc 3 camera.

## 5.3. Test results

### 5.3.1. Static tests

The results from the static tests of specimen types A, B, C and D are presented in Table 17. A grip separation of 115 mm and displacement rate of 3 mm/min are used for the pure polymer specimens. A grip separation of 122 mm and displacement rate of 3 mm/min are used for the composite specimens. The UTS is taken as the maximum achieved load during the test, [22, 36]. The UTS of the specimens is dependent on the specimen type and the test temperature. Moreover, an UTS increase at (-20)°C compared to RT is observed. The complete set of static test data is provided in Appendix 2.

**Table 17, Average results from the static tests**

| Specimen | T | $F1_{max}$ | $w_{specimen}$ | $t_{specimen}$ | UTS | UTS |
|---|---|---|---|---|---|---|
| [-] | [°C] | [N] | [mm] | [mm] | [N/mm] | [MPa] |
| Type A | RT | 2 100 | 13.04 | 1.94 | N/A | 83 |
| Type B | RT | 8 348 | 24.92 | N/A | 335 | N/A |
| | -20 | 9 727 | 24.94 | | 390 | |
| Type C | RT | 6 114 | 24.36 | | 251 | |
| | -20 | N/A | N/A | | 291 | |
| Type D | RT | 6 820 | 23.93 | | 285 | |
| | -20 | N/A | N/A | | 285 | |

The UTS of specimen C and D at (-20)°C is calculated (Equation 9) for time-saving reasons. The difference in fabric compressive stress between 26°C and (-20)°C is presented in Table 9.

$$UTS^{(-20)°C} = UTS^{RT} + dN11_{fiber}$$ Equation 9

### 5.3.2. Fatigue tests

The input for the fatigue test of the pure polymer are presented in Table 18. In total one specimen is tested at (-20)°C ambient temperature. The stress cycle is the same as the cycle of the matrix at the interface of the resin rich layer of the bead (Table 12, first data row). The specimen is tested up to 170 000 fatigue cycles, after which the test is stopped without any observed specimen failure or damage.

**Table 18, Input for the fatigue test of specimen type A matching the bead resin rich layer interface matrix stress cycle**

| Specimen | T | $F1_{min}$ | $F1_{max}$ | $w_{specimen}$ | $t_{specimen}$ | $S11_{min}$ | $S11_{max}$ | R | Cycles |
|---|---|---|---|---|---|---|---|---|---|
| [-] | [°C] | [N] | [N] | [mm] | [mm] | [MPa] | [MPa] | [-] | [-] |
| Type A | -20 | 673 | 862 | 13.14 | 1.60 | 32 | 41 | 0.78 | 170 000 |

The input for the fatigue test of the specimen type B that matches the bead resin rich layer interlaminar stress cycle are presented in Table 19. The bead interlaminar stress amplitude at the resin rich layer interface is matched (Table 13, first row). The exact interlaminar stress values are not matched. The specimen is tested up to 130 000 cycles after which the test is stopped without any observed specimen failure or damage.

**Table 19, Input for the fatigue of test specimen type B matching the bead interlaminar stress amplitude – R=0.1**

| Specimen | T | $F1_{min}$ | $F1_{max}$ | $w_{specimen}$ | $N11_{min}$ | $N11_{max}$ | Cycles |
|---|---|---|---|---|---|---|---|
| [-] | [°C] | [N] | [N] | [mm] | [N/mm] | [N/mm] | [-] |
| Type B | -20 | 154 | 1485 | 25.60 | 6 | 58 | 130 000 |

In order to investigate the fatigue damage progression adequately, an appropriate cyclic load level has to be chosen. This choice faces some difficulties. The problem lies in the fact that some loads are too low to create any damage in the tested specimens, while some loads are too high and the specimen fails prematurely in low-cycle fatigue.

One way of selecting a suitable load level for studying the damage is by relating the cyclic load level to the Ultimate Tensile Strength (UTS) of the sample, [37]. In this case the maximum cyclic load level is selected as a percentage of the UTS. The cyclic load level, when testing RTM 6 UD samples up to complete failure at RT, varies between 50%UTS and 70%UTS. The

specimens fail after approximately 200 000 cycles at 50%UTS load level and 15 000 cycles at 70%UTS load level.

The load levels selection for specimen types B and C is presented in Table 20 and Table 21. The tests are performed in the same sequence as they are presented. The selected load levels provide gradual progressive matrix cracking of the resin rich layer in both specimen types (Figure 45 and Figure 46), which is the desired damage level in this case. The load level is directly dependent on the UTS of the specimen. It is adjusted with a step multiple of 10%UTS. The load level at RT is 30%UTS and at (-20)°C – 40%UTS for both specimens.

**Table 20, Load level selection of specimen type B – R=0.1 (selected load levels are highlighted in green)**

| Specimen | T | $F1_{max}$ | $w_{specimen}$ | Damage level | $N11_{max}$ | $N11_{max}$ |
|---|---|---|---|---|---|---|
| [-] | [°C] | [N] | [mm] | [-] | [%UTS] | [N/mm] |
| Type B | -20 | 4729 | 24.25 | Immediate static cracking | 50 | 195 |
| Type B | -20 | 2034 | 26.08 | Nothing | 20 | 78 |
| Type B | -20 | 3051 | 26.08 | Progressive cracking of the resin rich layer | 30 | 117 |
| Type B | RT | 5841 | 24.96 | Premature rupture | 70 | 234 |
| Type B | RT | 3519 | 26.26 | Progressive cracking of the resin rich layer | 40 | 134 |

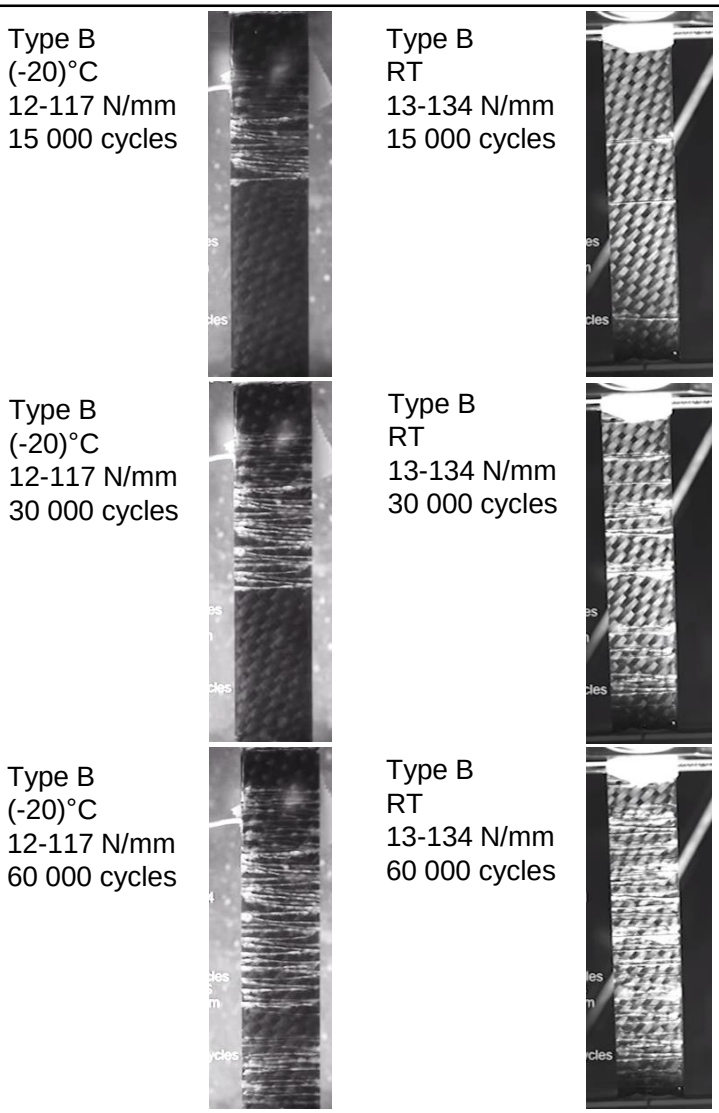


**Figure 45, Resin rich layer damage progression as function of the number of cycles of specimen type B**

**Table 21, Load level selection summary of specimen type C – R=0.1 (selected load levels are highlighted in green)**

| Specimen | T | $F1_{max}$ | $w_{specimen}$ | Damage level | $N11_{max}$ | $N11_{max}$ |
|---|---|---|---|---|---|---|
| [-] | [°C] | [N] | [mm] | [-] | [%UTS] | [N/mm] |
| Type C | -20 | 2092 | 24.05 | Progressive cracking of the resin rich layer | 30 | 87 |
| Type C | RT | 1810 | 24.13 | Nothing | 30 | 75 |
| Type C | RT | 2413 | 24.13 | Progressive cracking of the resin rich layer | 40 | 100 |

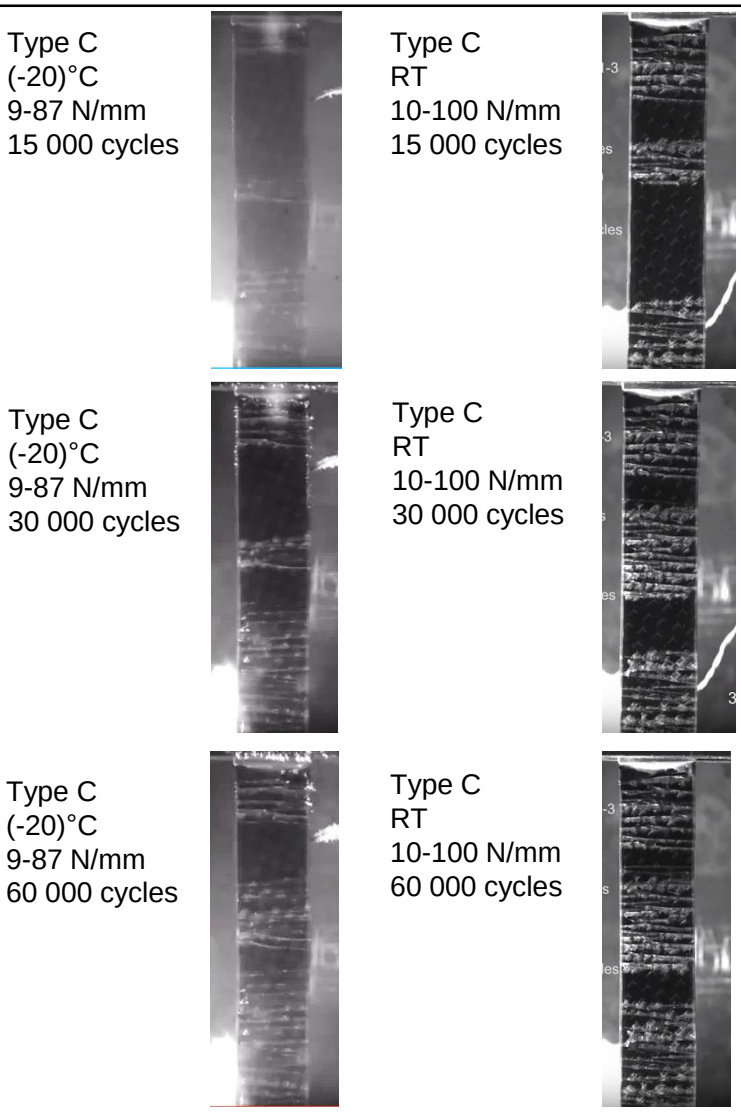


**Figure 46, Resin rich layer damage progression as function of the number of cycles of specimen type C**

The stiffness reduction results are presented in Table 22 and Table 23. The maximum observed reduction in stiffness for 60 000 cycles is in the range of 18%-34% compared to the intact specimen stiffness (i.e. 2500 cycles). The stiffness reduction at RT for 60 000 cycles is higher compared to (-20)°C in both specimen types. Moreover, the stiffness does not degrade rapidly, but gradually. The reduction in stiffness is also visible from the increasing displacement in time, because the test is load-controlled.

**Table 22, Stiffness reduction due to damage accumulation in time of specimen type B**

| Specimen | T | Cycles | $F1_{max}$ | Max. displ. | Measure of stiffness | Stiffness reduction |
|---|---|---|---|---|---|---|
| [-] | [°C] | [-] | [N] | [mm] | [N/mm] | [%] |
| Type B | -20 | 2 500 | 2853 | 0.92 | 3101 | N/A |
| | | 15 000 | 2861 | 1.01 | 2833 | 9 |
| | | 60 000 | 2855 | 1.23 | 2321 | 25 |
| Type B | RT | 2 500 | 3291 | 1.43 | 2301 | N/A |
| | | 15 000 | 3289 | 1.48 | 2222 | 3 |
| | | 60 000 | 3290 | 2.18 | 1509 | 34 |

**Table 23, Stiffness reduction due to damage accumulation in time of specimen type C**

| Specimen | T | Cycles | $F1_{max}$ | Max. displ. | Measure of stiffness | Stiffness reduction |
|---|---|---|---|---|---|---|
| [-] | [°C] | [-] | [N] | [mm] | [N/mm] | [%] |
| Type C | -20 | 2 500 | 2092 | 0.72 | 2906 | N/A |
| | | 15 000 | 2091 | 0.79 | 2647 | 9 |
| | | 60 000 | 2092 | 0.88 | 2377 | 18 |
| Type C | RT | 2 500 | 2419 | 1.23 | 1967 | N/A |
| | | 15 000 | 2419 | 1.3 | 1861 | 5 |
| | | 60 000 | 2418 | 1.82 | 1329 | 32 |

### 5.3.3. Fractography

The damage of specimen type B is presented in Figure 47, Figure 48, Figure 49 and Figure 50. In general, two main pure damage modes are observed in specimen type B – cracks and delamination. Looking in more details, the pure cracks are observed predominantly in resin rich areas. Cracked resin rich areas are located both at the surface (i.e. the resin rich layer) and inside the laminate. The cracks are also observed to penetrate through the fibers. However, cracks penetrating through the fibers are rarely seen.

In addition to the pure damage modes, an observed interactive damage mode in specimen type B is MCID. In other words, cracks coalescing with delamination is seen. Moreover, delamination coalesces with cracks. No pure or stand-alone delamination is observed. Delamination is observed to penetrate only up to the second fabric ply.

A phenomenon observed in the surface resin rich layer is that not all cracks reach the surface. There are cracks that continue all the way from the fibers to the surface of the resin rich layer. However, there are also cracks at the resin rich layer interface, the tips of which are located inside the resin rich layer. In other words, they do not propagate to the surface.

The crack density increase inside the laminate is presented in Figure 47 to Figure 49. The crack density increase in the resin rich layer is presented from a different perspective in Figure 45 and Figure 46. The damage and more specifically the crack density is observed to increase gradually with the increase in the number of cycles in specimen type B. At a high number of cycles there are still only a few areas of delamination. However, the number of matrix cracks, which are the predominant damage mode, is increased substantially.

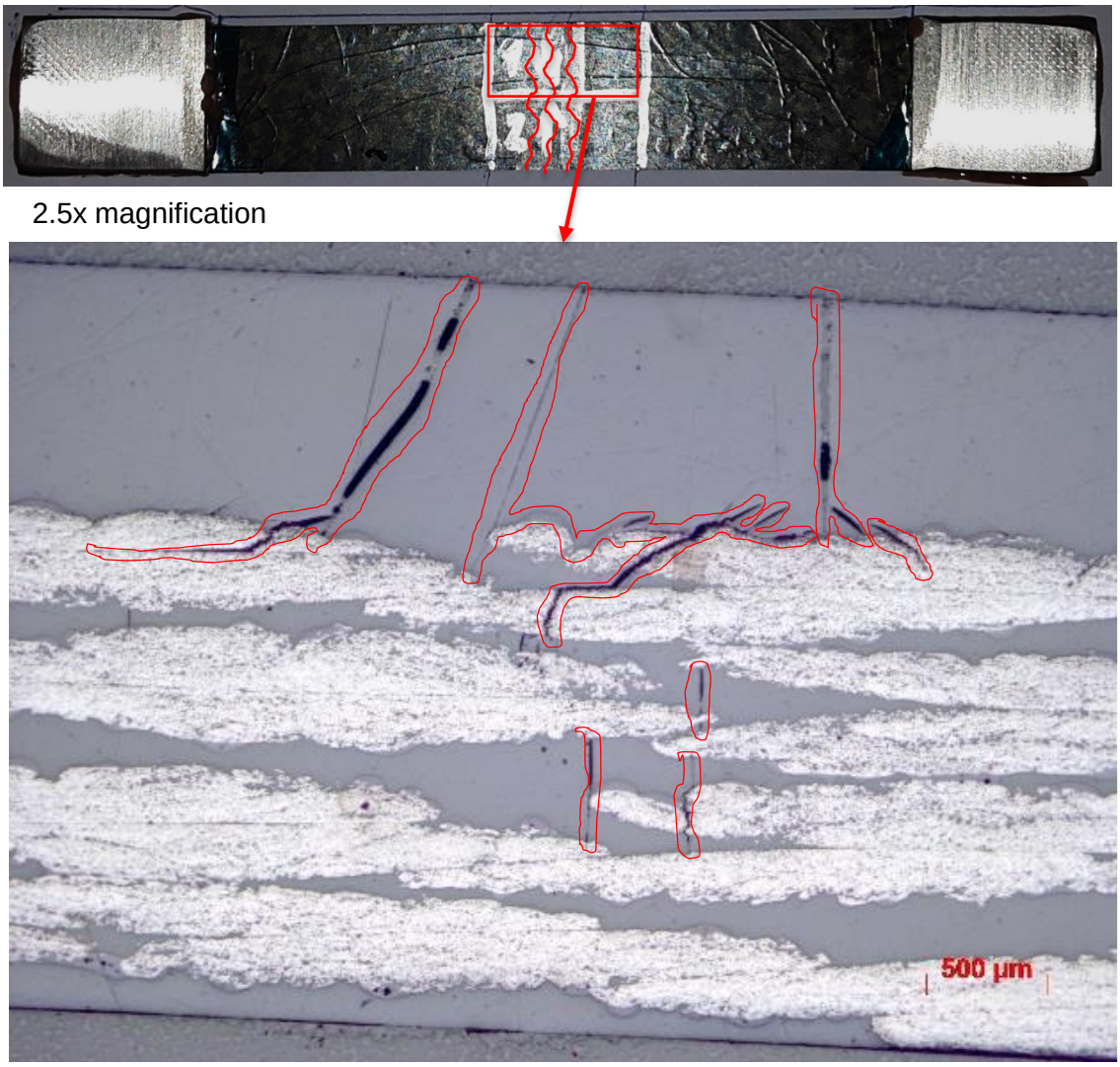


**Figure 47, Specimen type B damage – RT, max. load=134 N/mm, R=0.1, 15 000 cycles**

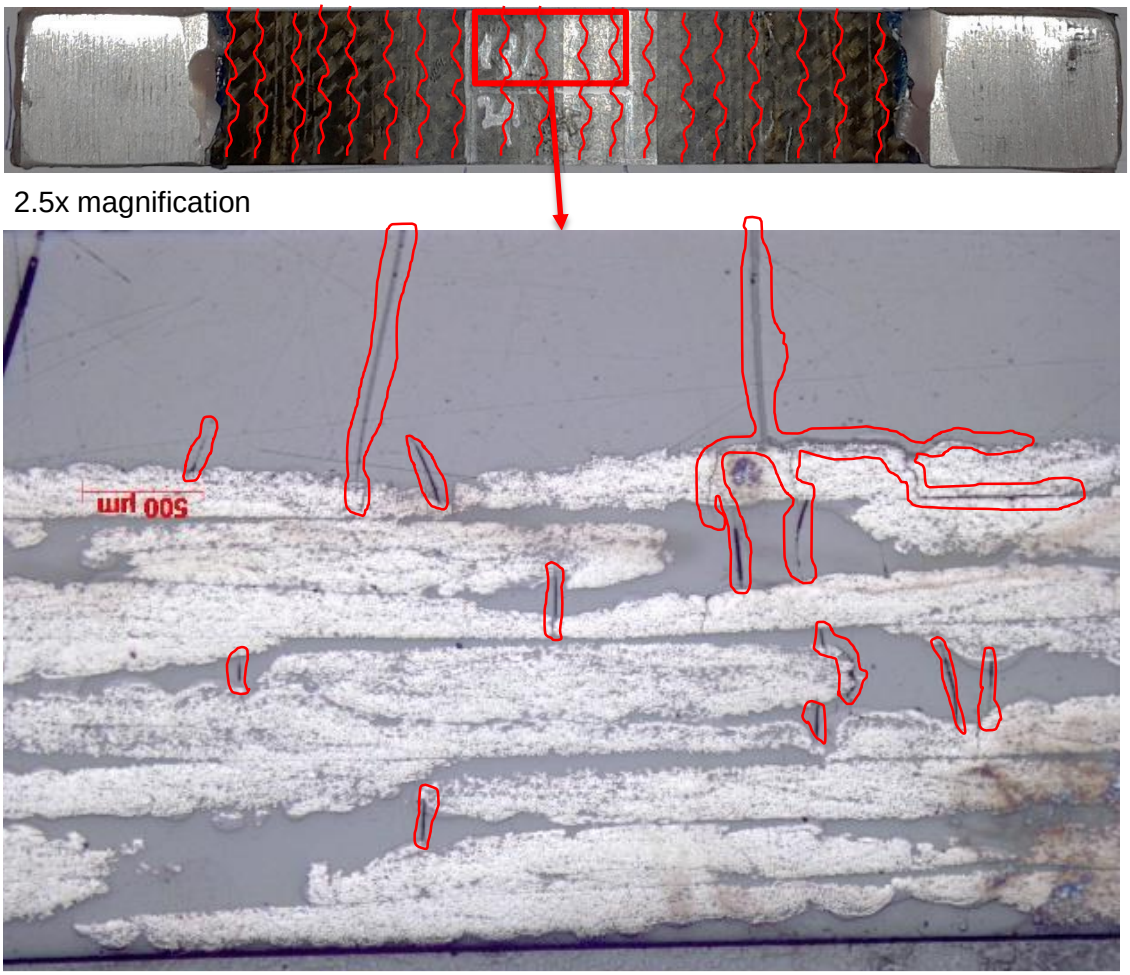


**Figure 48, Specimen type B damage – RT, max. load=134 N/mm, R=0.1, 60 000 cycles**

Specimen type B damage for high number of cycles at RT is presented in Figure 49 and at (-20)°C – in Figure 50. The specimen exhibits similar damage modes and similar crack densities at both temperatures. The crack density at RT is even higher compared to (-20)°C.

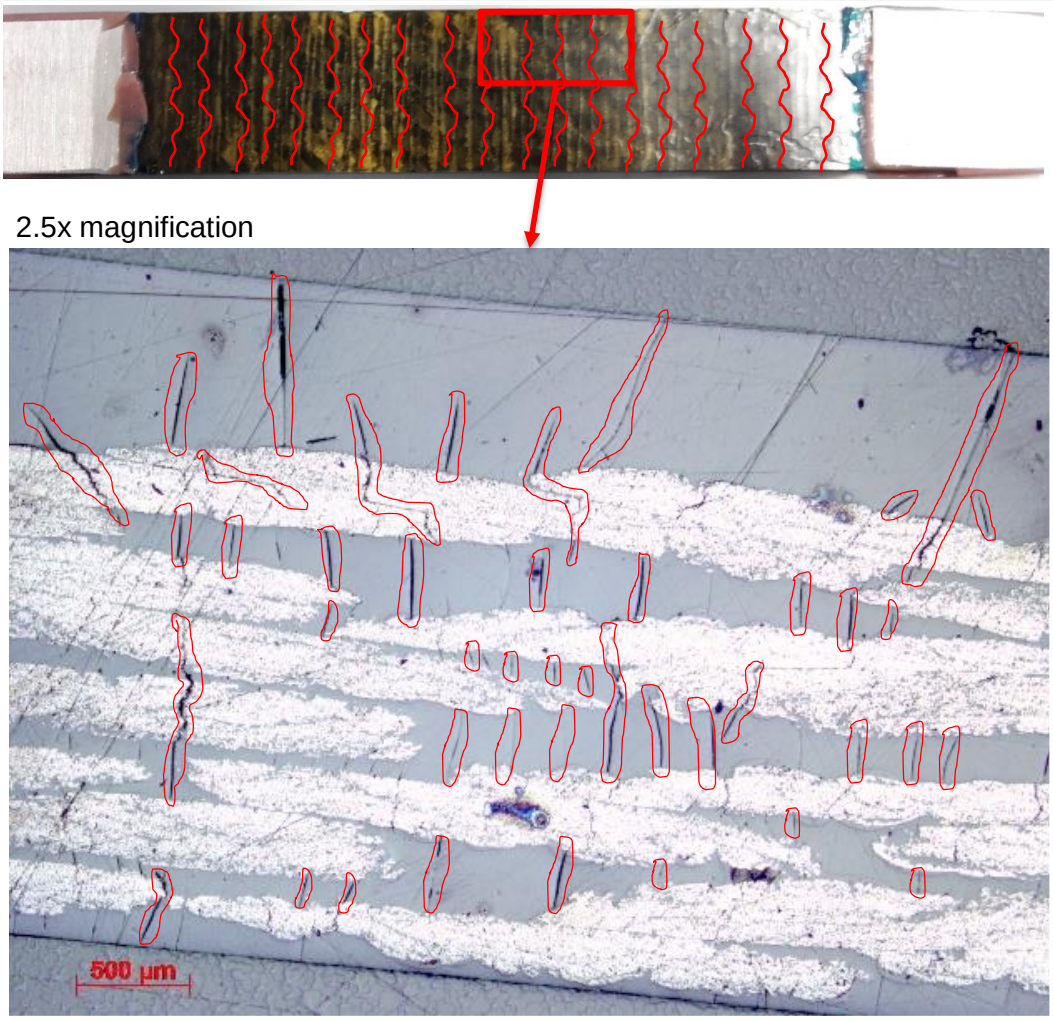


**Figure 49, Specimen type B damage – RT, max. load=134 N/mm, R=0.1, 140 000 cycles**

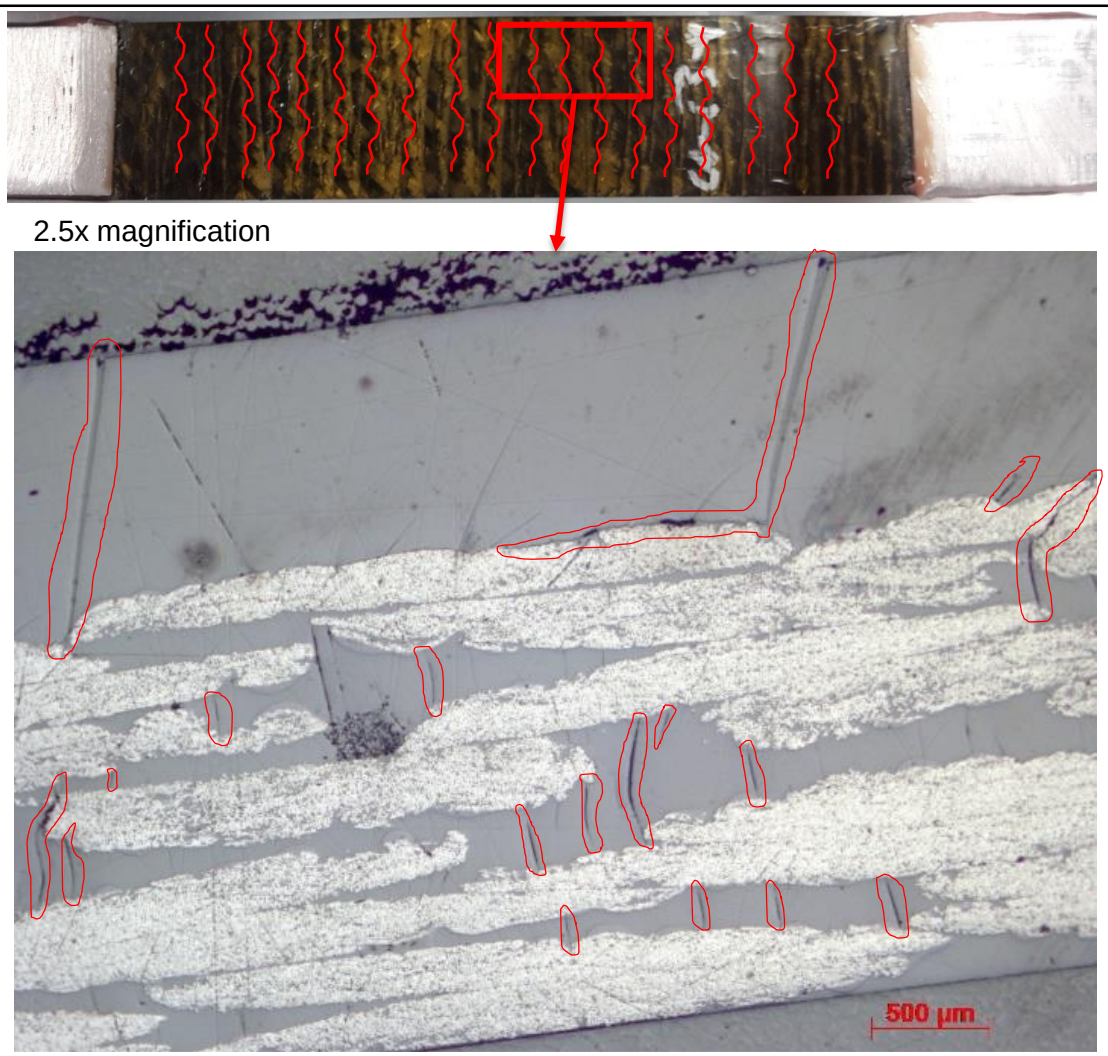


**Figure 50, Specimen type B damage – (-20)°C, max. load=117 N/mm, R=0.1, 180 000 cycles**

Damage behavior similar to specimen type B is observed in specimen type C for a high number of cycles at RT and (-20)°C (Figure 51 and Figure 52). However, there are a few differences in the damage behavior. In the first place, the crack density after a high number of cycles is lower compared to specimen type B. In the second place, all damage (both cracks and delamination) is observed to penetrate only up to the second fabric ply.

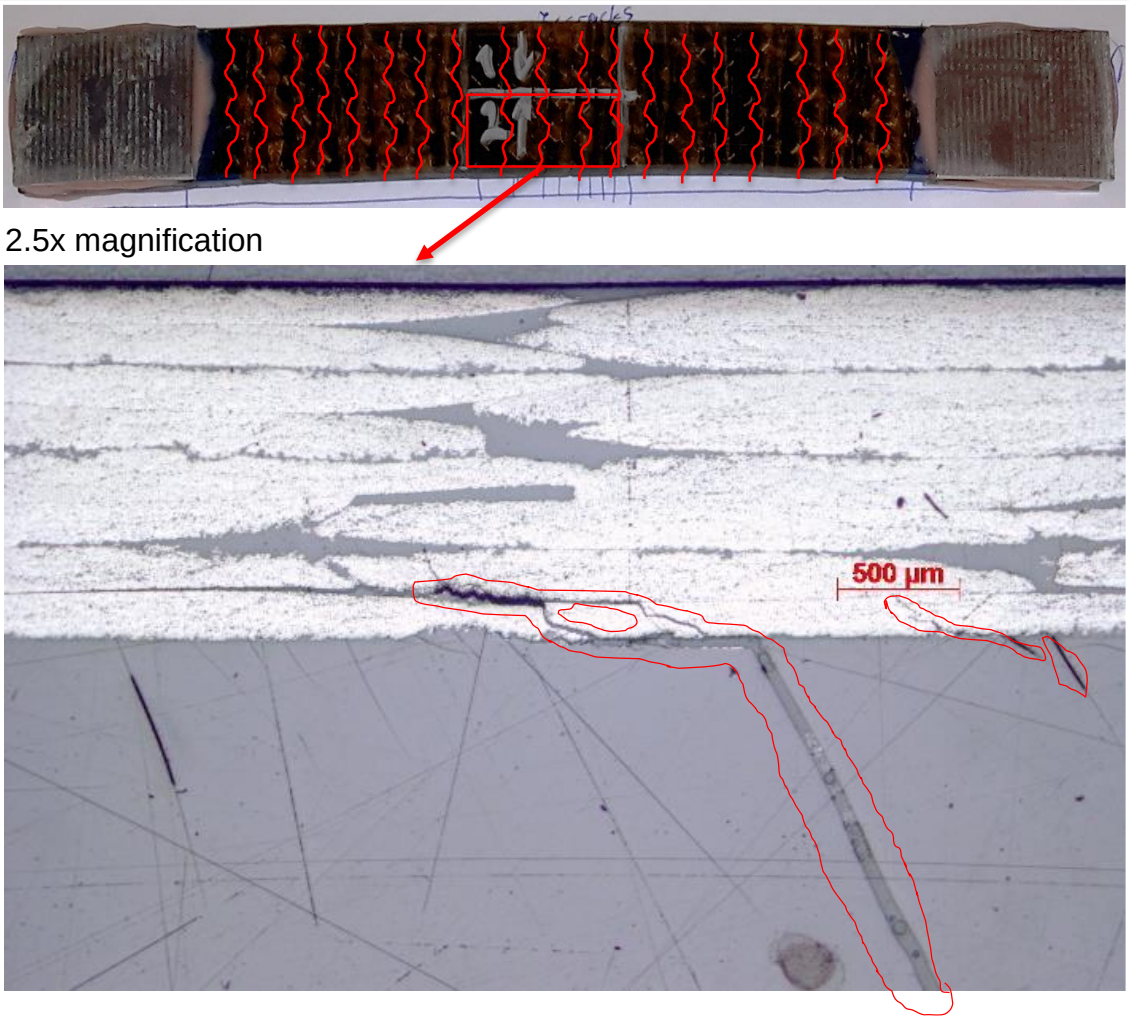


**Figure 51, Specimen type C damage – RT, max. load=100 N/mm, R=0.1, 100 000 cycles**

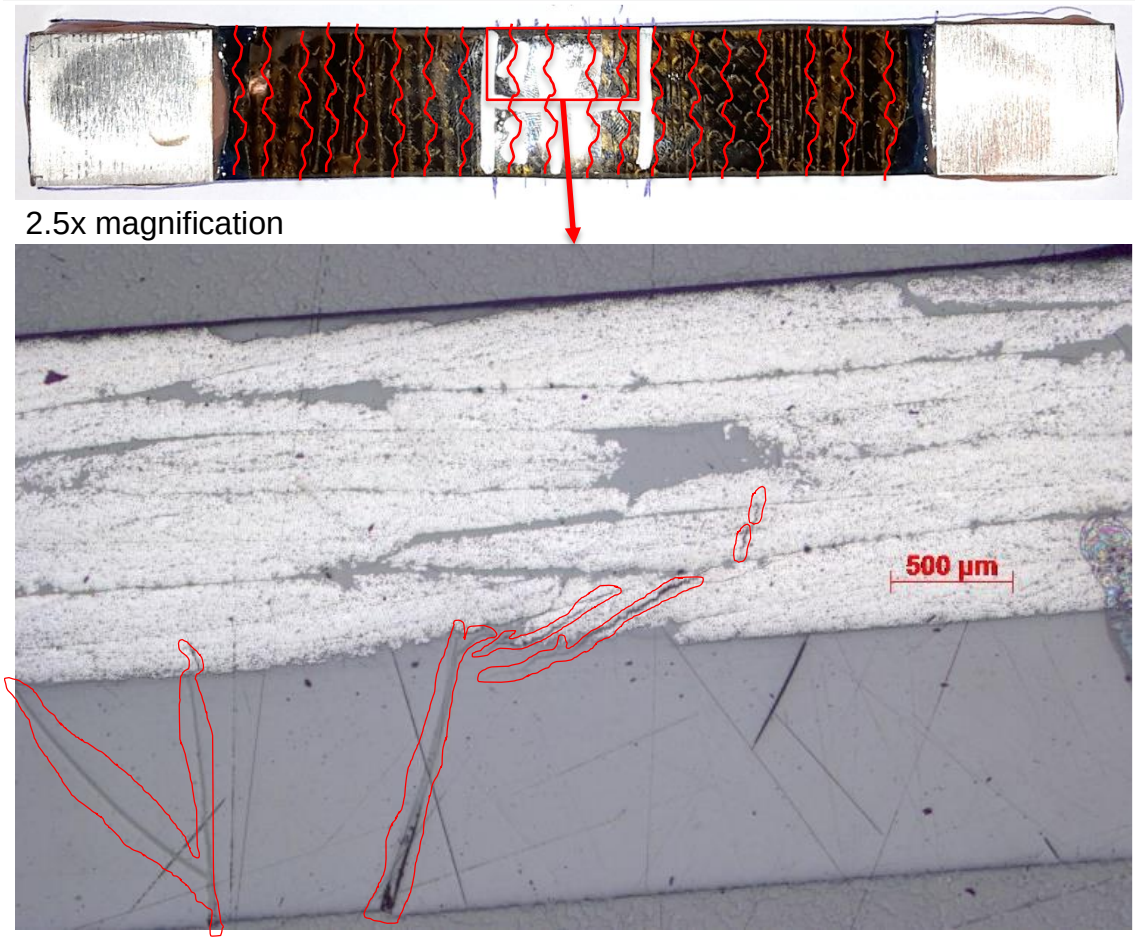


**Figure 52, Specimen type C damage – (-20)°C, max. load=87 N/mm, R=0.1, 100 000 cycles**

The fatigue damage of specimen D is presented in Figure 53 and Figure 54. Specimen type D is tested up to complete fatigue failure. The predominant damage mode is intralaminar cracking in-between the fibers. In contrast with specimen type B and C, specimen type D exhibits only a few matrix cracks in the small resin rich pockets.


**Figure 53, Specimen type D damage – RT , R=0.1; max. load=85 N/mm, 20 000 cycles; max. load=114 N/mm, 20 000 cycles; max. load=142 N/mm, 2 000 cycles**

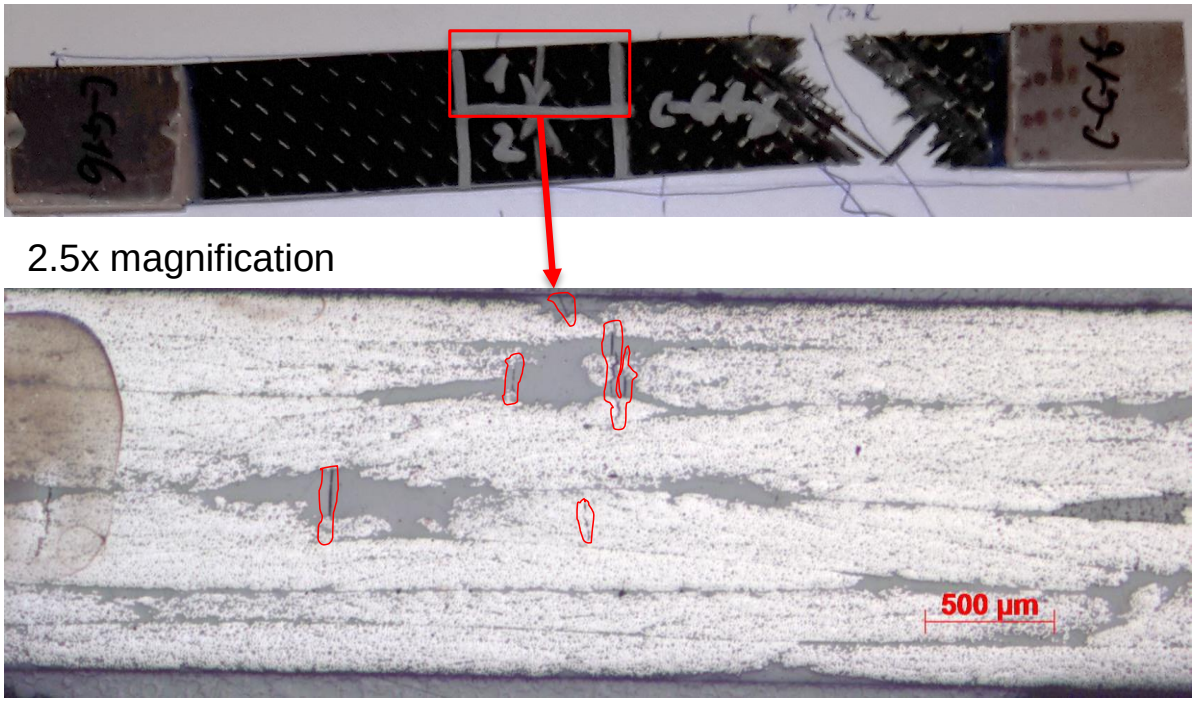


**Figure 54, Specimen type D damage – (-20)°C , R=0.1; max. loa d=85 N/mm, 20 000 cycles; max. load=114 N/mm, 20 000 cycles; max. load=142 N/mm, 19 000 cycles**

## 5.4. Chapter outcomes

Replicating the bead matrix stress cycle at the interface in a pure polymer specimen A yields no damage. Moreover, replicating the bead interlaminar stress cycle at the interface in a composite specimen B also yields no damage. However, by increasing the load as percentage of the composite specimen UTS damage similar to the bead is obtained. By analyzing the stresses in chapter 3 resulting from the experimentally selected mechanical loads it is discovered that the matrix stress cycle at the interface is similar in the bead and in the composite specimens B and C.

There are two implications of the results. First, matching the matrix stress at the interface could potentially be sufficient to replicate the bead damage. Second, the interface plays a role in the matrix cracking initiation.

# 6. Discussion of results

## 6.1. Similitude of the coupon and the bead stress state

### 6.1.1. Summary of results

The fiber stress cycle at the resin rich layer interface of the bead and the composite specimen induces stresses with opposite signs in the fibers of the two parts (Figure 55). The fiber stress in the bead at minimum load (T=26°C) is higher than the stress at maximum load (T=(-20)°C), (Table 10). In other words, the fibers are loaded in compression. In comparison, the fiber stress in specimen types B and C at minimum load is lower than the stress at maximum load (Table 10). In other words, the fibers are loaded in tension.

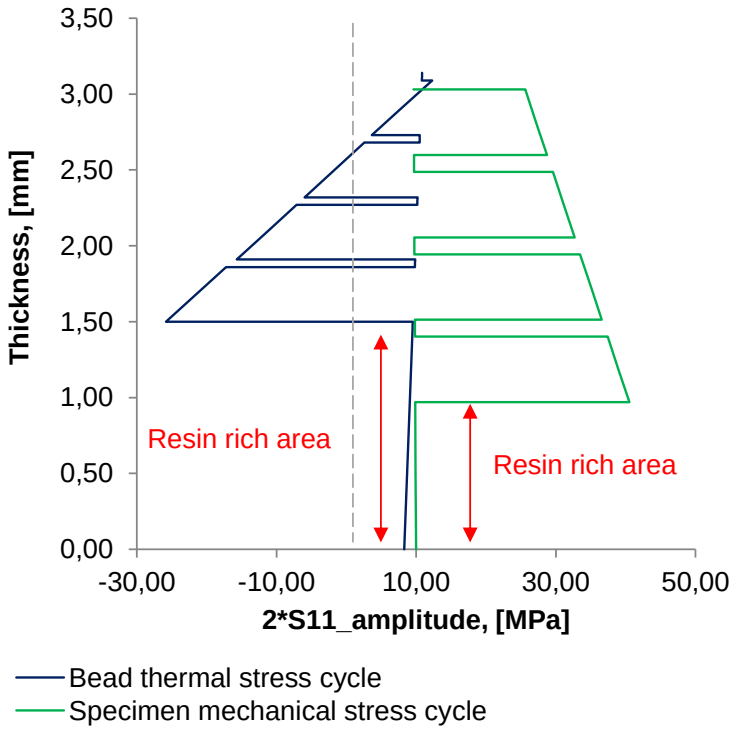


**Figure 55, Comparison of bead and composite specimen stress amplitudes (based on Figure 26 and Figure 28)**

In addition to the different fiber stress cycle, the fatigue parameters of the interlaminar stress cycle at the resin rich layer interface of the bead are different compared to the parameters of specimen types B and C (Table 24 and Table 25). The R-ratio of the bead is 0.76. The R-ratio of the specimens is 0.68-0.88. The interlaminar stress amplitude of the bead is 18 MPa compared to 12-16 MPa for the specimens. The maximum interlaminar stress in the bead is 153 MPa compared to 97-188 MPa for the specimens.

Matching the interlaminar stress cycle at the interface of the bead in the composite specimen type B yields no fatigue damage (section 5.3.2, Table 18). Matching the matrix stress cycle at the interface in specimen type A also yields no fatigue damage.

In contrast with the different fiber stress cycle, the matrix stress cycle at the resin rich layer interface in both the bead and the specimen is similar. The R-ratio in the bead is 0.78. The R-ratios of the composite specimens are in the range of 0.76-0.83, depending on the specimen type and ambient test temperature. The matrix stress amplitude in the bead is 5 MPa. The stress amplitudes of the specimens are in the range of 4-5 MPa, depending on the specimen type and ambient test temperature. The maximum matrix stress in the bead is 41 MPa. The maximum matrix stress in the composite specimen is in the range of 35-42 MPa. Moreover, applying mechanical fatigue loads creating matrix stress cycles similar to those in the bead at the interface yields fatigue damage similar to the bead (Table 24).

**Table 24, Fatigue parameters comparison of the matrix stress cycle and the interlaminar stress cycle at the resin rich layer interface (based on Table 12)**

| Specimen | T | Stress | R | Amplitude | Minimum | Maximum |
|---|---|---|---|---|---|---|
| [-] | [°C] | [-] | [-] | [MPa] | [MPa] | [MPa] |
| Bead | 26 and -20 | $S11_{matrix}$ | 0.78 | 5 | 32 | 41 |
| Type B | 26 | $S11_{matrix}$ | 0.76 | 5 | 32 | 42 |
| | -20 | $S11_{matrix}$ | 0.82 | 5 | 41 | 50 |
| Type C | 26 | $S11_{matrix}$ | 0.77 | 4 | 27 | 35 |
| | -20 | $S11_{matrix}$ | 0.83 | 4 | 34 | 41 |

**Table 25, Fatigue parameters comparison of the matrix stress cycle and the interlaminar stress cycle at the resin rich layer interface (based on Table 13)**

| Specimen | T | Stress | R | Amplitude | Minimum | Maximum |
|---|---|---|---|---|---|---|
| [-] | [°C] | [-] | [-] | [MPa] | [MPa] | [MPa] |
| Bead | 26 and -20 | SIL | 0.76 | 18 | 117 | 153 |
| Type B | 26 | SIL | 0.68 | 16 | 66 | 97 |
| | -20 | SIL | 0.80 | 13 | 101 | 127 |
| Type C | 26 | SIL | 0.81 | 14 | 116 | 144 |
| | -20 | SIL | 0.88 | 12 | 165 | 188 |

Despite the similarity of the R-ratio and the stress amplitude of the matrix stress cycle at the resin rich layer interface, the damage shows a peculiar trend. The composite specimen has higher crack density at RT compared to (-20)°C (Figure 56). Therefore, in general higher stress levels at RT are expected. However, the maximum matrix stress of the mechanical fatigue cycle at RT is smaller than the stress at (-20)°C.

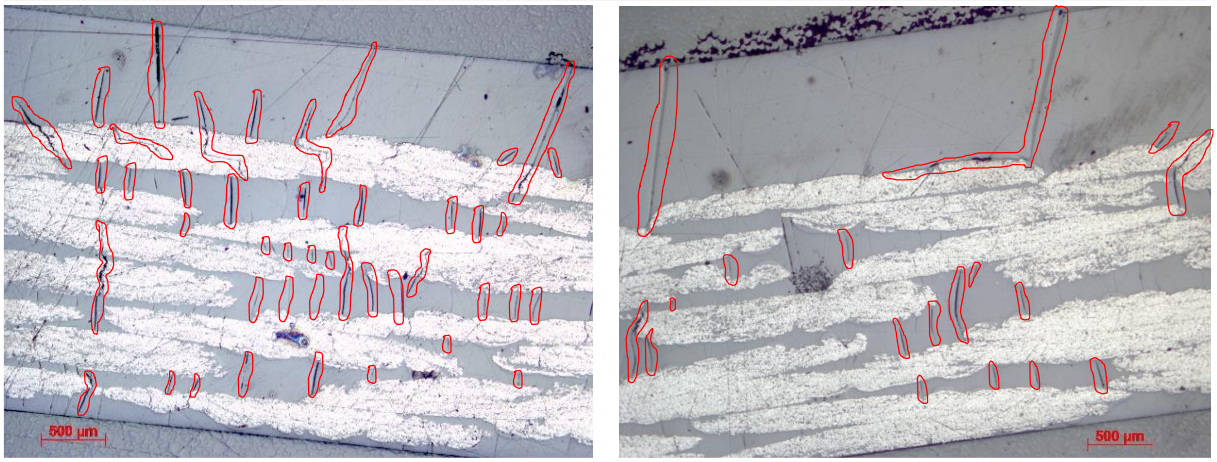


**Figure 56, Comparison of specimen type B damage state at different temperatures – left: RT, right: (-20)°C (based on Figure 49 and Figure 50)**

### 6.1.2. Discussion of results

No way of completely matching the bead stress cycle by mechanically loading coupons is found. Therefore, the matrix stress cycle and the interlaminar stress cycle at the bead interface are matched in separate tests. This decision impacts the subsequent test results. The stress cycle is not the same anymore. This means that if there is a combined effect of the two stress cycles on the damage, it cannot be entirely captured. Both stress cycles still exist in the laminate, but only one of them is matched at a time. The assumption is that one of these two stress cycles is the predominant contributor to the damage.

Based on the results the stresses have different importance on the damage. Solely matching the bead interlaminar stress amplitude at the interface yields no damage in specimen B. This implies the interlaminar stress is not the initiation driver for the damage. On the other hand, solely matching the matrix stress cycle at the interface in a pure polymer specimen yields no damage in specimen A within the test cycles and the applied loads. However, if the damage is matched in composite specimens B and C at both temperatures, the matrix stress cycle seems to be similar to the bead. This implies there is an additional contributing factor to the matrix stress cycle.

As mentioned in the previous paragraph solely matching the matrix stress in a pure polymer specimen A yields no damage in it. In addition, the mechanical load levels required to obtain damage similar to the bead damage are selected experimentally by gradually increasing the load. Then, by applying these load levels, matrix stress cycles similar to the bead at the interface are calculated. This implies the driver of the damage initiation is not solely the calculated stress. The interface plays a role.

One parameter that is not matched in any test is the fiber compressive stress. The reason for that is because it is not suspected to influence the matrix cracking. However, such influence might exist. One way it could contribute to the matrix damage is by affecting the stresses in directions different from the longitudinal direction. In the current ±45° stacked laminate there is a coupling between compression and shear. This means the fibers could shear thereby affecting the matrix stresses. Another contribution of the fiber compressive stress is influencing the bending stresses due to the asymmetry caused by the resin rich layer specimen.

Depending on the fiber compressive stress, equilibrium at different through-the-thickness stresses is reached and thereby the matrix stress is also affected.

The first hypothesis could be tested by stacking a 0/90° laminate. This stacking sequence would avoid the compression/shear coupling thereby leaving only the Poisson's coupling. Moreover, the Poisson's ratio of a cured lamina made from RTM 6 and woven 5HS carbon fabric is low (0.05). The second hypothesis could be tested by producing composite specimens with double-sided resin rich layers. It would avoid the secondary bending due to the laminate layer stiffnesses' asymmetry. Moreover, the through-the-thickness stress gradient would be reduced to a minimum. The only phenomenon creating a stress gradient would be the difference in matrix shrinkage at the free surface of the resin rich layer and at the interface.

## 6.2. Behavior of matrix damage replicated by mechanical cycling

### 6.2.1. Summary of results

**Resin rich layer fatigue damage initiation location**

The damage in the resin rich layer is observed to initiate bellow the resin rich layer surface. The damage mode observed in the resin rich layer in the bead and specimen types B and C is matrix cracking. Matrix cracks starting within the interface, but not reaching the surface of the resin rich layer, are observed in the bead and in the specimens (Figure 57). Their tips remain inside the resin rich layer.

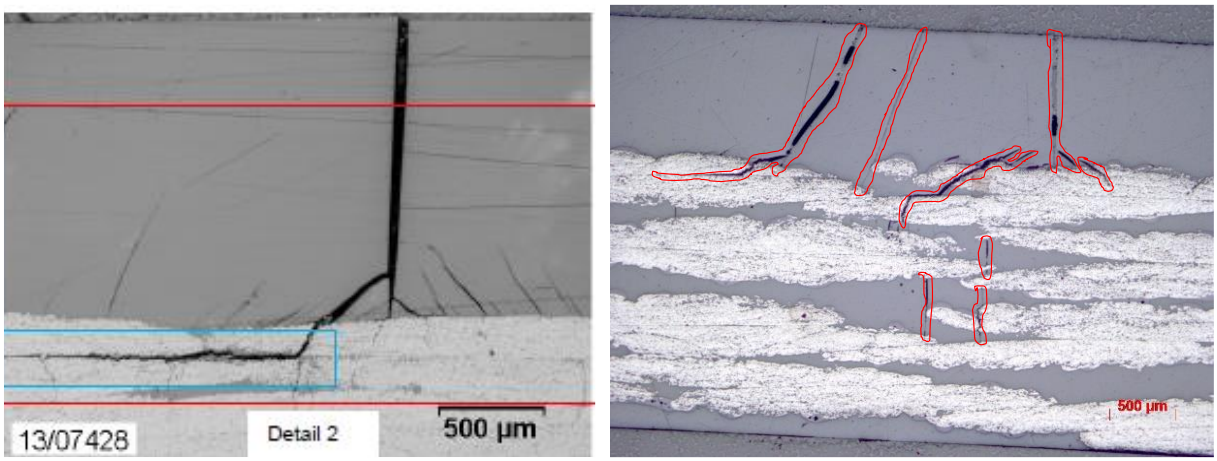


**Figure 57, Comparison of bead and composite specimen damage – left: bead, right: specimen type B (based on Figure 7 and Figure 47)**

**Resin rich layer fatigue damage growth**

The damage modes observed in the bead and the specimens are similar (Figure 57). Both parts exhibit pure damage modes (i.e. not interactive) – cracks and delamination. In both parts cracks in the resin rich layer that reach and do not reach the surface are observed. In both parts intralaminar cracks in-between the fibers are observed. In both parts small delaminated areas are observed. Moreover, both in the bead and in the specimen one interactive damage

mode is observed. Cracks coalesce with the delamination, thereby creating MCID. No pure or stand-alone delamination is found.

**Influence of the laminate quality on the damage**

The laminate quality shows influence on the damage penetration depth. A comparison of the damage states at a high number of cycles of a poorly compacted specimen and well compacted specimen is provided in Figure 58. The poorly compacted specimen damage penetrates through its full depth. In comparison, the damage in the well compacted specimen penetrates only up to the second fabric ply.

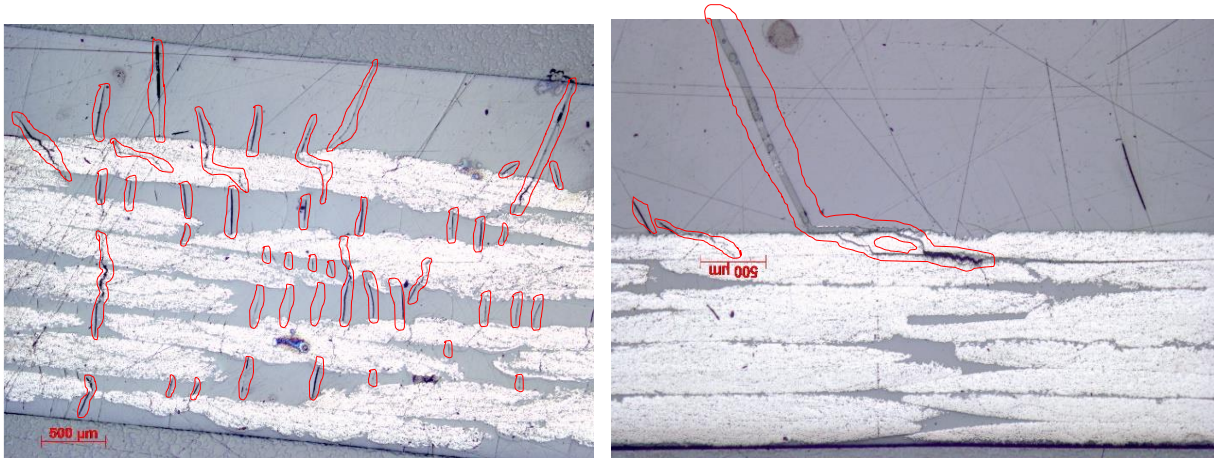


**Figure 58, Comparison of damage penetration depth for differently compacted specimens – left: poorly compacted specimen type B, right: well compacted specimen type C (based on Figure 49 and Figure 51)**

The poorly compacted specimen has resin rich areas not only at the surface, but also inside the laminate. These inner resin rich areas facilitate the development of matrix cracks inside the laminate. In comparison, the well compacted laminate has small inner resin rich areas, which rarely act as damage initiation sites. A supporting evidence is that a fatigued well compacted specimen D without a surface resin rich layer exhibits cracks predominantly in-between the fibers (Figure 53 and Figure 54).

### 6.2.2. Discussion of results

All damage observations discussed here are strictly valid under the assumptions discussed in section 6.1. Moreover, it should be kept in mind that the stresses of the bead are not completely matched in the specimens.

The damage in the resin rich layer is observed to initiate bellow the free surface. Tips of cracks not reaching the free surface are observed. A fact supporting the observed damage initiation location is the calculated high matrix residual thermal stress. There is a positive through-the-thickness stress gradient in the resin rich layer of the bead and the specimens (Figure 25, Figure 27 and Figure 29). This implies that the matrix stress at the resin rich layer interface is higher compared to the surface.

Another argument supporting the observation is that the fibers are much stiffer than the resin. They constrain the matrix thermal shrinkage at the interface more than at the free surface. Moreover, specimen type A shows no damage, when replicating the matrix stress cycle at the bead resin rich layer interface (section 5.3.2.). This implies that the damage is related to the interface.

The damage in the coupons is similar to a certain extent to the damage found in the literature (chapter 2). In between the fibers there are transverse cracks. Moreover, some of these transverse cracks coalesce by forming a delamination. However, there is one major difference with the reviewed literature – the presence of the resin rich area. The predominant amount of damage is in the resin rich area. Moreover, in case of the poorly compacted specimen B, where the interface resin layers are relatively thick, the predominant amount of damage is also in these interlaminar resin rich areas.

The laminate compaction shows influence on the damage penetration depth. Specimen type C, which has improved compaction, exhibits lower damage penetration depth than specimen B. However, the well compacted specimen type C base laminate is subjected to a second curing cycle, which could potentially act as a post-curing stage. Normally RTM 6 post-curing stages reduce the matrix high residual tensile stress in a composite, which could potentially make it require higher stresses to crack, [20]. This is a probable explanation of the cracking of the resin rich layer (one curing cycle) and almost no cracking of the base laminate (two curing cycles).

Looking at the damage behavior in the specimen one new hypothesis emerges. The delamination seems to be always preceded by transverse cracks and to stem from their tips. A supporting evidence of this hypothesis is that no stand-alone delamination is found, but many single cracks are observed. The hypothesis could be tested by performing similar tests as for specimen type B at RT, but using a smaller step (number of cycles). In other words, reduce the time interval at which the specimens are examined microscopically, because using the current interval some damage events might be missed.

## 6.3. Suitability of mechanical testing approach for studying the bead damage

### 6.3.1. Summary of results

In addition to the already presented results in section 6.1 and section 6.2, one more summary set of results is relevant to this section. The composite specimens are tested 33 333 times faster, if only the test speed is compared. The test frequency of the bead thermal cycle is higher than the frequency of the specimen mechanical cycle. The frequency of the bead thermal cycle is 0.00015 Hz, [7]. In contrast the frequency of the specimen mechanical cycle is 5 Hz (section 5.2.). It takes 39 days to test the bead for 500 thermal cycles compared to only 1 minute and 40 seconds for 500 mechanical cycles of the specimens.

The specimen mechanical fatigue test is also about 156 times faster, if the total test durations are compared. The bead resin rich area damage saturates in about 500 thermal cycles, [7]. In contrast, about 100 000 cycles (the number is exaggerated on purpose to be conservative) are required for the damage in the specimen resin rich area to saturate (Figure 45 and Figure 46). These numbers of cycles lead to 39 days of total test duration for the bead and about 6 hours for the specimen.

### 6.3.2. Discussion of results

Several things tested during this research are found to be working. Through-the-thickness stress gradient behavior of the bead is reproduced. However, only one bead stress of interest (interlaminar stress or matrix stress) at a certain through-the-thickness location is able to be reproduced at a time. Moreover, the damage found in the bead and in the composite specimens are visually similar. The matrix stress cycles at the interface in the bead and the composite specimens, which are responsible for the damage initiation, are also similar

On the other hand, a few things tested during this research are found not to be working. No way of reproducing the bead thermal stress state completely by the use of mechanical load is discovered. This means that no way of investigating the bead damage mechanically in a coupon under absolutely the same conditions is found. It is also discovered that matching the matrix stress cycle in a pure polymer specimen A does not lead to any damage in it. Moreover, matching solely the interlaminar stress cycle in a composite specimen also results in no damage.

The things that are found not to be working require one topic to be studied further. New possibilities of mechanically matching both the interlaminar and the matrix stress cycles at the interface need to be investigated further. However, even then these new possibilities would not be able to reproduce the fiber compressive stress cycle. The reason is that the mechanical load can only create stresses with the same sign whereas the thermal cycle creates stresses with opposite signs.

The chosen approach in this project has several assumptions. However, it is found to head in the right direction. It is discovered with high probability that the damage initiation driving parameter is the matrix stress cycle at the interface (similar, but not the same stress cycles). Moreover, this is a result of independent correlation of fractographic observations from physical tests and FE stress analysis. However, there are still uncertainties regarding the exact role of the interlaminar stress and the fiber compressive stress.

Despite the assumptions in the test approach it has certain advantages. The mechanical fatigue testing is faster than thermal cycling, because of the higher test frequency. Moreover, it is observed that mechanical testing at RT using a widely available fatigue testing machine could be performed. The reason is that it is observed that the damage and the matrix stress cycle at the interface are similar at RT and (-20)°C. Thereby, using a complicated thermal cycling chamber is avoided. Also there is better accessibility to the specimen during testing for filming it in real time with a camera for better surface crack monitoring.

A few benefits for manufacturing the specimens exist. First, the specimens have simpler flat geometry than the bead curved shape. Second, the mold for manufacturing the flat composite specimens is easier for production and also cheaper. It consists only of flat sheet metal and straight steel wires.

Looking retrospectively, after obtaining the knowledge learned from this project a few things could be done differently. First, it would make more sense initially to try to match the matrix stress cycle at the interface directly in a composite specimen rather than the interlaminar stress cycle or the matrix cycle in a polymer specimen. The reason is that the discovered cracks are developed in the matrix and more specifically in the resin rich layer. Moreover, it is already known that solely matching the interlaminar stress does not produce any damage in composite specimen type B and solely matching the matrix stress yields no damage in a pure polymer specimen type A. Second, it would also make sense to investigate the influence of the second curing cycle in specimen type B, it is cured completely in one cycle. This means both manufacturing methods could be compared and the influence of the second curing cycle investigated after testing the specimens.

## 6.4. Criticality of matrix cracking

### 6.4.1. Summary of results

The damage accumulation influences the laminate mechanical properties. The accumulated damage causes laminate stiffness degradation in time. The stiffness reduction for 60 000 cycles, which is approximately the number of cycles at which the resin rich layer cracks saturate (Figure 45 and Figure 46) is in the range of 18-34%. Moreover, the stiffness reduction at RT is higher compared to the reduction at (-20)°C.

**Table 26, Stiffness reduction due to damage accumulation in time of specimen type B (based on Table 22 and Table 23)**

| Specimen | T | Cycles | Stiffness reduction |
|---|---|---|---|
| [-] | [°C] | [-] | [%] |
| Type B | -20 | 60 000 | 25 |
| | RT | 60 000 | 34 |
| Type C | -20 | 60 000 | 18 |
| | RT | 60 000 | 32 |

### 6.4.2. Discussion of results

The predominant damage mode in the composite specimens is transverse matrix cracking. The transverse matrix cracking leads to stiffness reduction of the laminate with up to 34%. This stiffness reduction is not reached rapidly. The cracks density is gradually increased until they reach a saturation level. The gradual crack density increase implies that the laminate stiffness also degrades gradually in time, which is preferred compared to a rapid decrease.

The composite specimen stiffness decrease in time is not measured accurately. The embedded grip displacement gage of the fatigue testing machine is used. However, an extensometer would provide more accurate displacement measurements, which are used for calculating the stiffness. Another possible option is using strain gages.

Another suspected influenced mechanical property is the shear buckling load of the laminate, [14]. The shear buckling load is influenced by delamination. Cracks coalescing with delamination are observed in the composite specimens. In order for a delamination to influence the shear buckling load, it should grow to a sufficient extent thereby splitting the laminate in two sub-laminates. The size of a centrally located delamination should be at least 20% of the laminate width (Figure 11). However, a delamination of this size is not observed in any of the fatigued specimens (section 5.3.3.).

The delamination is also not measured accurately. Only a longitudinal cross-section of delamination is observed. Normally, a delamination is developed in a laminate in two directions in-plane. This implies that in-order to observe and characterize a delamination several cuts along the two directions should be made. Another option is using non-destructive testing techniques such as ultrasonic testing and X-ray.

# 7. Conclusions and recommendations

## 7.1. Conclusions

During the course of this research project, the project evolved from goals and research questions through all performed research activities to the results obtained from these activities. The main goal of this project is to investigate cracks found in resin rich areas of composite rib beads. In order to reach the goal, several research questions are formulated. First, it should be determined if the cracks could be studied by mechanically cycling simplified coupons rather than thermally cycling the bead. Second, it should be investigated where the damage initiate and which are its driving parameters. Third, the way the damage accumulates in the laminate and its impact on the laminate should be determined.

The research activities for this project include FE analysis, specimen manufacturing and physical tests. The FE analysis is exclusively a stress analysis of undamaged specimens to investigate the drivers of the damage initiation. Two types of specimens are produced – pure epoxy specimens made by injection molding and composite specimens made by vacuum infusion. The specimens are tested statically and in fatigue by mechanically applying stress cycles which are similar, but not the same as in the bead.

The results from the research activities are discussed in the previous chapter. They cover four major topics – similitude of the coupon and the bead stress state, behavior of the matrix damage replicated by mechanical cycling, suitability of a mechanical testing approach for studying the bead damage and criticality of matrix cracking. The conclusions from the discussion chapter and respectively the whole research project are directly related to the research questions and formulated as follows:

1. Is it possible to replicate the bead resin rich area thermal fatigue stress cycle faster in a simple coupon specimen loaded in mechanical tension-tension?
    - It is discovered by calculations that it is not possible to exactly reproduce the bead thermal stress cycle by mechanically cycling a coupon specimen;
    - Based on testing and visual fatigue damage state comparison it is possible to create damage similar to the bead thermal fatigue damage by mechanically cycling a coupon specimen;
    - The mechanical fatigue coupon test is faster than a thermal fatigue test of a bead. However, the physical differences between the two loads should be taken into account.
2. Which parameters drive the fatigue damage initiation?
    - It is discovered by testing and calculations that approximately matching the matrix R-ratio and stress amplitude at the resin rich layer interface with the first fabric ply in the coupon specimen leads to visually similar types of damage, as seen in the bead;
    - It is visually observed in tests that the specimen laminate compaction affects the fatigue damage penetration depth. Better compaction reduces the damage penetration depth and vice versa.
3. Where does the fatigue damage initiate?
    - It is visually observed in tests and supported by calculations that the fatigue damage is not initiated at the surface of the resin rich layer. It is not directly observed, but with high likelihood the damage initiates below the surface within the interface of the resin rich layer with the first fabric ply.

4. How does the fatigue damage accumulate in the laminate?
    - It is visually observed in tests that the fatigue damage accumulates in the laminate in the form of cracks and delamination;
    - It is visually observed in tests that during damage accumulation the damage penetrates through the laminate thickness.
5. How does the fatigue damage affect the laminate mechanical properties?
    - It is discovered by testing that the laminate stiffness is reduced, because of the fatigue damage accumulation during mechanical cycling.

## 7.2. Recommendations

The first set of recommendations is regarding the design of laminated composite parts. Design recommendations:

1. Formation of resin rich areas should be avoided both at the surface and inside the laminate;
2. However, if resin rich area formation cannot be avoided, at least its effect should be minimized by ensuring the laminate is well compacted (i.e. only surface resin rich areas should be allowed to form).

The second set of recommendations is regarding the aspects of this project that need further research. Future research recommendations:

1. The laminate stiffness reduction is calculated only approximately based on the forces and displacements measured by the test machines embedded gages (load cell and grip displacement gage). Therefore, the stiffness reduction of the laminate due to damage accumulation should be investigated more accurately in a step of smaller number of cycles for specimen types B and C;
2. The damage level of specimen type B is different at RT and (-20)°C and this is clearly visible at the microscopic images. However, the difference in the damage level of specimen type C at both temperatures is not that clearly visible from the microscopic images. Therefore, performing more tests of specimen type C would clarify this scatter;
3. Specimen type C, which exhibits reduced damage penetration depth, undergoes second curing cycle. Therefore, the potential influence of the second curing cycle of the well compacted base laminate of specimen type C on the damage penetration depth should be investigated.

# Appendix 1: Complete sets of specimen layer-by-layer thickness measurements

### Specimen type B

The layer thicknesses of the specimen type B are measured in two directions – longitudinal and lateral. The measured longitudinal and lateral positions distribution is presented in Figure 59.


**Figure 59, Positions for measuring layer thicknesses of specimen type B**

Thicknesses of three layer types are measured – resin rich layer, interface resin layer and fabric ply. The measurement results are presented in Table 27, Table 28 and Table 29.

**Table 27, Thicknesses in [mm] of specimen type B resin rich layer**

| Section | | Lateral position | | | | | | | | Average |
|---|---|---|---|---|---|---|---|---|---|---|
| | 1 | 2 | 3 | 4 | 5 | 6 | 7 | 8 | 9 | |
| A-A | 1.113 | 0.955 | 0.940 | 0.767 | 0.635 | 0.763 | 0.924 | 1.201 | 1.411 | 0.968 |
| B-B | 1.165 | 0.881 | 0.859 | 0.650 | 0.575 | 0.747 | 0.948 | 1.207 | 1.521 | 0.950 |
| C-C | 1.150 | 1.053 | 0.835 | 0.709 | 0.650 | 0.866 | 1.105 | 1.074 | 1.492 | 0.993 |
| Total average: 0.970 mm | | | | | | | | | | |

**Table 28, Thicknesses in [mm] of specimen type B interface resin layer**

| Section | Lateral position | | | Average |
|---|---|---|---|---|
| | 1 | 2 | 3 | |
| A-A | 0.126 | 0.075 | 0.104 | 0.102 |
| B-B | 0.075 | 0.201 | 0.119 | 0.132 |
| C-C | 0.074 | N/A | 0.119 | 0.097 |
| Total average: 0.112 mm | | | | |

**Table 29, Thicknesses in [mm] of the specimen type B fabric ply**

| Section | Lateral position | | | Average |
|---|---|---|---|---|
| | 1 | 2 | 3 | |
| A-A | 0.484 | 0.486 | 0.375 | 0.448 |
| B-B | 0.399 | 0.493 | 0.380 | 0.424 |
| C-C | 0.462 | 0.336 | 0.464 | 0.421 |
| Total average: 0.431 mm | | | | |

**Specimen type C**

The layer thicknesses of the specimen manufactured in two-steps are measured only in the middle lateral positions of three longitudinal sections (Figure 60). Two longitudinal sections are located near the two tab areas and one is in the middle of the specimen gage area.

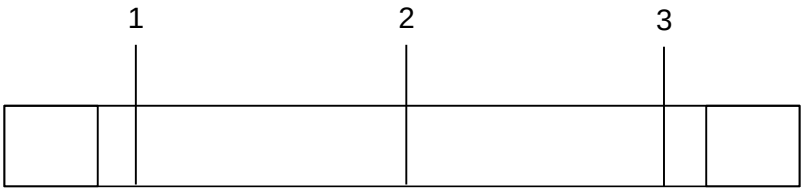


**Figure 60, Locations of sections for measuring thicknesses of the specimen type C**

The thicknesses of the resin rich layer and of the fabric ply are measured and averaged. The results are presented in Table 30 and Table 31.

**Table 30, Thicknesses in [mm] of specimen type C resin rich layer**

| Section 1 | Section 2 | Section 3 | Total average |
|---|---|---|---|
| 2.24 | 2.29 | 2.90 | 2.48 |

**Table 31, Thicknesses in [mm] of specimen type C fabric ply**

| Location 1 | Location 2 | Location 3 | Total average |
|---|---|---|---|
| 0.321 | 0.396 | 0.358 | 0.358 |

# Appendix 2: Complete sets of static test data

### Specimen type A

The static raw data of the specimen type A is presented in Table 32. The statistics of the processed raw data is presented in Table 33.

**Table 32, Raw data from the static test of specimen type A at RT**

| ID | $F1_{max}$ | Displ. at $F1_{max}$ | $w_{specimen}$ | $t_{specimen}$ | UTS |
|---|---|---|---|---|---|
| [-] | [N] | [mm] | [mm] | [mm] | [MPa] |
| 4 | 1511 | 6.45 | 12.94 | 1.47 | 79 |
| 10t-4 | 2961 | 8.69 | 13.07 | 2.62 | 86 |
| 13t-2 | 1800 | 5.38 | 13.06 | 1.50 | 92 |
| 11t-2 | 2856 | 8.38 | 13.08 | 2.52 | 87 |
| 12t-4 | 1486 | 6.09 | 13.03 | 1.60 | 71 |

**Table 33, Test parameters and statistics from the static test of specimen type A at RT**

Standard: ASTM D638
Type of test: Static tension
Grip separation: 115 mm
Displacement rate: 3 mm/min
Time to failure: from 1 min to 5 min

| | $F1_{max}$ | Displ. at $F1_{max}$ | $w_{specimen}$ | $t_{specimen}$ | UTS |
|---|---|---|---|---|---|
| | [N] | [mm] | [mm] | [mm] | [MPa] |
| Average value | 2123 | 7,00 | 13.04 | 1.94 | 83 |
| Standard deviation | 729 | 1.46 | 0.06 | 0.58 | 8 |
| Coefficient of variation, [%] | 34.34 | 20.84 | 0.44 | 29.68 | 9.59 |

### Specimen type B

The failure modes of the specimen type B are presented in Figure 61. The raw test data from each specimen is presented in Table 34 and Table 36. The statistics of the raw data after processing is presented in Table 35 and Table 37.

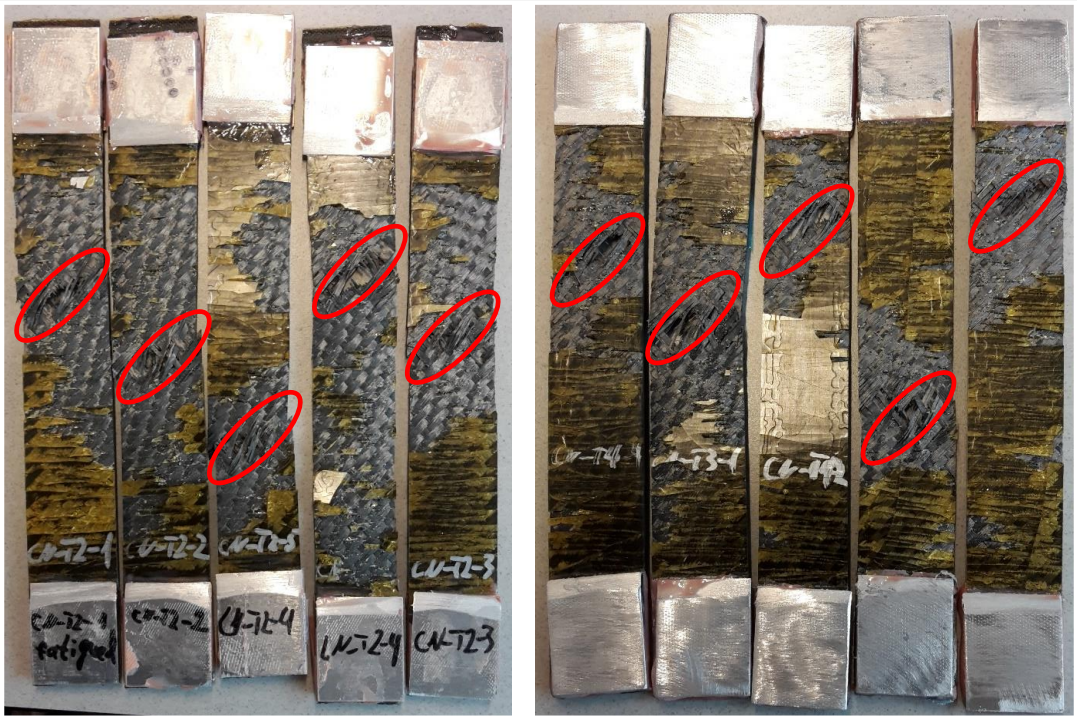

**Figure 61, Static failure modes of specimen type B – left: RT and right: (-20)°C**

**Table 34, Raw data from the static test of specimen type B at RT**

| ID | $F1_{max}$ | Displ. at $F1_{max}$ | $w_{specimen}$ | UTS |
|---|---|---|---|---|
| [-] | [N] | [mm] | [mm] | [N/mm] |
| CN-T2-1 | 7919 | 12.01 | 25.50 | 311 |
| CN-T2-2 | 8537 | 14.82 | 25.64 | 333 |
| CN-T2-3 | 8377 | 13.72 | 24.94 | 336 |
| CN-T2-4 | 9153 | 16.75 | 24.43 | 375 |
| CN-T2-5 | 7697 | 12.02 | 24.07 | 320 |

**Table 35, Test parameters and statistics from the static test of specimen type B at RT**

| | | | | |
|---|---|---|---|---|
| Standard: ASTM D3518<br>Type of test: Static in-plane shear<br>Grip separation: 122 mm<br>Displacement rate: 3 mm/min<br>Time to failure: from 1 min to 5 min | | | | |
| | $F1_{max}$ | Displ. at $F1_{max}$ | $w_{specimen}$ | UTS |
| | [N] | [mm] | [mm] | [N/mm] |
| Average value | 8336 | 13.86 | 24.92 | 335 |
| Standard deviation | 568 | 2.00 | 2.12 | 25 |

| Standard: ASTM D3518<br>Type of test: Static in-plane shear<br>Grip separation: 122 mm<br>Displacement rate: 3 mm/min<br>Time to failure: from 1 min to 5 min | | | | |
|---|---|---|---|---|
| | $F1_{max}$ | Displ. at $F1_{max}$ | $w_{specimen}$ | UTS |
| | [N] | [mm] | [mm] | [N/mm] |
| Coefficient of variation, [%] | 6.81 | 14.46 | 2.85 | 7.33 |

**Table 36, Raw data from the static test from specimen type B at (-20)°C**

| ID | $F1_{max}$ | Displ. at $F1_{max}$ | $w_{specimen}$ | UTS |
|---|---|---|---|---|
| [-] | [N] | [mm] | [mm] | [N/mm] |
| CN-T2-1 | 11095 | 9.62 | 25.83 | 430 |
| CN-T2-2 | 9958 | 10.03 | 24.43 | 408 |
| CN-T2-3 | 9010 | 8.24 | 23.65 | 381 |
| CN-T2-4 | 9219 | 7.72 | 25.47 | 362 |
| CN-T2-5 | 9390 | 8.85 | 25.30 | 371 |

**Table 37, Test parameters and statistics from the static test of specimen type B at (-20)°C**

| Standard: ASTM D3518<br>Type of test: Static in-plane shear<br>Grip separation: 122 mm<br>Displacement rate: 3 mm/min<br>Time to failure: from 1 min to 5 min | | | | |
|---|---|---|---|---|
| | $F1_{max}$ | Displ. at $F1_{max}$ | $w_{specimen}$ | UTS |
| | [N] | [mm] | [mm] | [N/mm] |
| Average value | 9735 | 8.89 | 24.94 | 390 |
| Standard deviation | 838 | 0.95 | 0.88 | 28 |
| Coefficient of variation, [%] | 8.61 | 10.72 | 3.55 | 7.13 |

**Specimen type C**

The failure modes of the specimen type C are presented in Figure 62. The static raw data of the specimen type C is presented in Table 38. The statistics of the processed raw data is presented in Table 39.

**Figure 62, Static failure modes of specimen type C at RT**

**Table 38, Raw data from the static test of specimen type C at RT**

| ID | $F1_{max}$ | Displ. at $F1_{max}$ | $w_{specimen}$ | UTS |
|---|---|---|---|---|
| [-] | [N] | [mm] | [mm] | [N/mm] |
| C-GR1-1 | 6197 | 8.33 | 24.27 | 255 |
| C-GR1-2 | 6011 | 7.49 | 24.44 | 246 |

**Table 39, Test parameters and statistics from the static test of specimen type C at RT**

| Standard: ASTM D3518<br>Type of test: Static in-plane shear<br>Grip separation: 122 mm<br>Displacement rate: 3 mm/min<br>Time to failure: from 1 min to 5 min | | | | |
|---|---|---|---|---|
| | $F1_{max}$ | Displ. at $F1_{max}$ | $w_{specimen}$ | UTS |
| | [N] | [mm] | [mm] | [N/mm] |
| Average value | 6104 | 7.91 | 24.36 | 251 |
| Standard deviation | 132 | 0.59 | 0.12 | 7 |
| Coefficient of variation, [%] | 2.15 | 7.51 | 0.49 | 2.65 |

## References

[1] Ploeger, "A330 VTP box Rib 9 drawing," vol. Issue G, ed. DA: Airbus Operations GmbH, N/A.

[2] T. Anft, "CFRP fin box composite summary report," vol. Issue 4.0, ed. TTEC: Airbus Operations GmbH, 2010.

[3] S. P. Renze and D. H. Laananen, "BUCKLING BEHAVIOR OF BEAD-STIFFENED COMPOSITE PANELS," *Composites Science and Technology,* vol. 50, pp. 157-166, 1994.

[4] H. Hosseini-Toudeshky, J. Loughlan, and M. Kharazi, "The buckling characteristics of some integrally formed bead stiffened composite panels," *Thin-Walled Structures,* vol. 43, pp. 629-645, Apr 2005.

[5] S. K. Mazumdar, *Composites manufacturing; materials, product, and process engineering*. Boca Raton: CRC Press, 2002.

[6] LightweightStructuresBV, "Vacuum infusion-Lecture slides," in *Part of the lecture series of the "AE4ASM004 Manufacturing of Aerospace Structures & Materials" course.*, ed: TU Delft, 2014.

[7] T. Rankenburg, "Crack initiation due to temperature difference," ed. EVMVU3: Airbus Operations GmbH, 2008.

[8] S. Schwaneberg, "Failure analysis of VTP ribs from LR (A330&A340), MSN 736, operated by VIR," vol. Issue 1.0, ed. ESMUG: Airbus Operations GmbH, 2013.

[9] ASTM, "D3479 - Standard Test Method for Tension-Tension Fatigue of Polymer Matrix Composite Materials," ed. USA: ASTM, 2012.

[10] B. Fiedler, C. De Jong, T. Hobbiebrunken, M. Hojo, and K. Schulte, "Micro/macro-mechanical approach of first ply failure in CFRP," *Journal of Materials Science,* vol. 41, pp. 6760-6767, 2006.

[11] P. Johnson and F. K. Chang, "Characterization of matrix crack-induced laminate failure - Part I: Experiments," *Journal of Composite Materials,* vol. 35, pp. 2009-2035, 2001.

[12] L. Zubillaga, A. Turon, J. Renart, J. Costa, and P. Linde, "An experimental study on matrix crack induced delamination in composite laminates," *Composite Structures,* vol. 127, pp. 10-17, 2015.

[13] J. Nairn and S. Hu, "The initiation and growth of delaminations induced by matrix microcracks in laminated composites," *International Journal of Fracture,* vol. 57, pp. 1-24, 1992.

[14] H. Suemasu, "Analytical study of shear buckling and postbuckling behaviors of composite plates with a delamination," *JSME International Journal, Series 1: Solid Mechanics, Strength of Materials,* vol. 34, pp. 135-142, 1991.

[15] M. Damghani, D. Kennedy, and C. Featherston, "Critical buckling of delaminated composite plates using exact stiffness analysis," *Computers and Structures,* vol. 89, pp. 1286-1294, 2011.

[16] A. P. Vassilopoulos, *Fatigue life prediction of composites and composite structures*. Cambridge: Woodhead, 2010.

[17] J. A. Nairn, "Matrix microcracking in composites," *Polymer matrix composites,* vol. 2, pp. 403-432, 2000.

[18] C. Henaff-Gardin and M. C. Lafarie-Frenot, "Specificity of matrix cracking development in CFRP laminates under mechanical or thermal loadings," *International Journal of Fatigue,* vol. 24, pp. 171-177, 2// 2002.

[19] J. A. Nairn, "Microcracking, Microcrack-Induced Delamination, and Longitudinal Splitting of Advanced Composite Structures," NASA, USA1992.

[20] T. S. Gross, H. Jafari, I. Tsukrov, H. Bayraktar, and J. Goering, "Curing cycle modification for RTM6 to reduce hydrostatic residual tensile stress in 3D woven composites," *Journal of Applied Polymer Science,* vol. 133, 2016.

[21] ASTM, "D3039 - Standard Test Method for Tensile Properties of Polymer Matrix Composite Materials," ed. USA: ASTM, 2014.

[22] ASTM, "D3518 - Standard Test Method for In-Plane Shear Response of Polymer Matrix Composite Materials by Tensile Test of a 645° Laminate," ed. USA: ASTM, 2013.

[23] Hexcel, "Datasheet-HexFlow® RTM 6 resin," ed: Hexcel, N/A.

[24] T. Hobbiebrunken, M. Hojo, B. Fiedler, M. Tanaka, S. Ochiai, and K. Schulte, "Thermomechanical analysis of micromechanical formation of residual stresses and initial matrix failure in CFRP," *JSME International Journal, Series A: Solid Mechanics and Material Engineering,* vol. 47, pp. 349-356, 2004.

[25] T. Hobbiebrunken, B. Fiedler, M. Hojo, S. Ochiai, and K. Schulte, "Microscopic yielding of CF/epoxy composites and the effect on the formation of thermal residual stresses," *Composites Science and Technology,* vol. 65, pp. 1626-1635, 2005.

[26] B. Fiedler, T. Hobbiebrunken, M. Hojo, and K. Schulte, "Influence of stress state and temperature on the strength of epoxy resins," in *11th International Conference on Fracture 2005, ICF11*, 2005, pp. 2271-2275.

[27] M. Kiasat, "Curing shrinkage and residual stresses in viscoelastic thermosetting resins and composites," PhD, TU Delft, 2000.

[28] K. Magniez, A. Vijayan, and N. Finn, "Apparent volumetric shrinkage study of RTM6 resin during the curing process and its effect on the residual stresses in a composite," *Polymer Engineering and Science,* vol. 52, pp. 346-351, 2012.

[29] TohoTenax, "Datasheet-Tenax® HTA filament yarn," ed, 2014.

[30] D. Karls, "Assessment of surface cracks in the VTP beaded ribs produced by resin infusion with analytical models," Master, PFH-Private University of Applied Sciences, Hamburg, 2009.

[31] SIMULIA, "ABAQUS analysis manual," ed, 2012.

[32] I. M. Daniel and O. Ishai, *Engineering mechanics of composite materials*. New York: Oxford University Press, 1994.

[33] Airbus, "Standard Modulus Carbon Fibre Fabric (with or without Binder); 5H Satin, 370 g/m2; Liquid epoxy resin 180°C curing," vol. Issue 5.0, ed: Airbus Operations GmbH, 2014.

[34] Ohrloff, "Fatigue test program for A330/A340 vertical tail," vol. Issue 1.0, ed. TK 536: Airbus Operations GmbH, 1991.

[35] ASTM, "D7791 - Standard Test Method for Uniaxial Fatigue Properties of Plastics," ed. USA: ASTM, 2012.

[36] ASTM, "D638 - Standard Test Method for Tensile Properties of Plastics," ed. USA: ASTM, 2014.

[37] M. Y. Shiino, L. M. De Camargo, M. O. H. Cioffi, H. C. J. Voorwald, E. C. Ortiz, and M. C. Rezende, "Correlation of microcrack fracture size with fatigue cycling on non-crimp fabric/RTM6 composite in the uniaxial fatigue test," *Composites Part B: Engineering,* vol. 43, pp. 2244-2248, 2012.